Magmatic and hydrothermal evolution of the Mesoproterozoic Current PGE-Cu-Ni deposit within the Thunder Bay North Intrusive Complex: Insights from trace element geochemistry and Nd, Sr, O, and H isotopes

Andrea Paola Corredor Bravo

A thesis presented to Lakehead University in partial fulfillment

of the requirements for the degree of

Master of Science in Geology

Department of Geology

Thunder Bay, Ontario, Canada, 2024

ABSTRACT

The Mesoproterozoic Current Intrusion, part of the Thunder Bay North Intrusive Complex, hosts PGE-Cu-Ni mineralization (indicated minerals resource of 8.2 million tonnes grading 0.33% Cu, 0.22% Ni, and 2.7g/t Pt+Pd and an inferred mineral resource of 1.6 million tonnes grading 0.32% Cu, 0.20% Ni, and 1.7g/t Pt+Pd). The intrusion consists of a northwest-trending conduit-type body, consisting of wehrlite, lherzolite, olivine gabbronorite ± troctolite, associated with the earliest stages of the Midcontinent Rift System (MRS) and the Keweenaw plume that intruded Archean rocks. The intrusion is associated with multiple splays related to the Quetico fault that cross the boundaries between the Quetico basin and the Wabigoon terrane of the Superior Province. The intrusion hosts four mineralized zones: the Current and Bridge Zone in the northwest, the Beaver-Cloud Zone in the middle, and the 437-Southeast Anomaly Zone in the southeast.

Geochemical analysis reveals that the intrusion displays a well-defined primitive mantle-normalized pattern resembling Oceanic Island Basalt and a lack of continental crust contamination given the slightly positive Nb, La, and Ce anomalies relative to Th. The La/Sm_n values for the intrusion (from 1.8 to 2.6) indicate a mafic magma was derived from an enriched mantle plume; this is consistent with other intrusions associated with the MRS, including the Nipigon Sills and the Lone Island, the Escape, and the Seagull intrusions. The Sr_i (from 0.7021 to 0.7043) and ε_{Nd} (from -1.18 to -4.02) values of the Current Intrusion are slightly lower than those typical values of the mantle source at 1100 Ma. Given the absence of geochemical anomalies that indicate assimilation of the Archean crust, an enriched Subcontitnetal Lithospheric Mantle (SCLM) is suggested to have interacted with the parental magma to generate the slightly negative radiogenic isotope values.

Stable isotope analysis suggests that the rocks of the intrusion underwent interactions with mantle-derived fluids (δ^2H from −40 to −80‰, $\delta^{18}O$ from 5.5 to 7.0‰), meteoric fluids (δ^2H <-80‰, $\delta^{18}O$ <5.5‰), and crustal-derived fluids ($\delta^{18}O$ >7‰). Analysis of the hydrothermal phases reveals three distinct mineral assemblages (domains) that altered the intrusive rocks. i) Domain A, influenced by the interaction of mantle-derived and meteoric fluids, formed antigorite, magnetite ± actinolite-tremolite after olivine, actinolite-tremolite and clinochlore after pyroxene, epidote-sericite and clinochlore after plagioclase, pyrite and magnetite after pyrrhotite, magnetite after pentlandite, secondary pyrrhotite after pyrite, chamosite and pyrite after magnetite. ii) Domain B consists of lizardite-chrysotile and an increase in mineral modal abundances of clinochlore, chamosite, epidote, sericite, pyrite, and secondary magnetite relative to Domain A. Stable isotopes in this domain indicate interaction with mixed mantle-derived and meteoric fluids. iii) Domain C, characterized by talc and carbonate minerals that replace domains A and B, with stable isotopes, indicating crustal-derived fluids.

In summary, this study indicates the Current Intrusion was derived from magmas that originated from an enriched mantle plume that interacted with an enriched SCLM as it ascended towards the crust. The documented alteration types resulted from fluid:rock interaction between the host intrusion and fluids derived from mantle-derived, crustal, and meteoric sources. These fluids also generated the mineral volume reduction of primary sulfides

ACKNOWLEDGEMENTS

This thesis was made possible thanks to the unconditional support of my supervisor Dr. Pete Hollings. I also want to thank Dr. Matthew Brzozowski for his guidance and patience, as well as NSERC, Clean Air Metals Inc., and Lakehead University for the funding and opportunity to develop this project. I also thank my family for their understanding and keeping me motivated.

TABLE OF CONTENTS

LIST OF FIGURES

LIST OF TABLES

1. INTRODUCTION

Magmatic sulfide deposits contribute 99% of the Platinum Group Elements (PGE) production and 60% of the global nickel production (Naldrett, 2004; Li & Ripley, 2011). Naldrett et al. (1990) classified the magmatic Ni-Cu-PGE deposits into two groups: i) sulfide-rich, with high Ni and Cu concentrations. ii) sulfide-poor, with high Platinum Group Elements (PGE) content (this group is the most economically significant).

Sulfide-rich Ni-Cu-(PGE) deposits are predominantly associated with komatiitic flows, high-Mg basalt, and picrite-mafic-ultramafic intrusions (Li & Ripley, 2011). Conversely, sulfide-poor PGE deposits are primarily situated within extensive layered intrusions (Li & Ripley, 2011). Naldrett (1981) proposed the classification of magmatic sulfides rich in Ni and Cu into three groups according to their tectonic setting: i) noritic rocks intruding an astrobleme, as in the case of Sudbury. ii) flows of basalts (mantle plumes) associated with intracontinental rift zones, as seen in the deposits of Noril'sk, Duluth, Tamarack, and the Thunder Bay North Intrusive Complex. iii) tholeiitic and komatiitic flows and intrusions in Precambrian greenstone belts as in the case of the Kambalda and Pechenga deposits.

Barnes and Lightfoot (2005) suggested that most of the host rocks for magmatic sulfide deposits originate from the mantle and are typically transported to the crust through normal faults in continental rifts. In contrast, Begg et al. (2010) argue that most Ni-Cu-PGE deposits are associated with mantle plumes that, on their ascent to the crust, move laterally along the base of the subcontinental lithospheric mantle (SCLM) to cratonic margins (thinner zones than the interior of the craton) where melting is induced by decompression during regional tectonism, creating

expansion zones along active structures that serve as pathways for the plume. The Subcontinental Lithospheric Mantle (SCLM; beneath the continental crust) is a few tens of kilometers thick beneath rift zones (Griffin & O'Reilly, 2007). The Archean SCLM consists of ultramafic rocks (generally harzburgites with low Ca and high Cr in garnets and magnesian olivine and orthopyroxene) that are dominantly depleted in Al_2O_3, FeO, and CaO and elevated in MgO compared to younger SCLM (Griffin & O'Reilly, 2007).

Nickel-Cu-PGE deposits are primarily formed in post-collision tectonic environments within intracontinental areas along reactivated paleocratons or on the edges of cratonic basins (Begg et al., 2010). The addition of S from crustal rock leads to saturation of base-metal-rich sulfide melt in the mantle magma (Barnes & Lightfoot, 2005), which is induced by two primary processes (Robertson et al., 2015); i) thermal aureoles, involving the transfer of mass from the country rock to the magma through thermal decomposition of minerals present in the country rock (induced by the diffusion of heat emanating from the magma); ii) mass transfer through the assimilation, melting, and/or dissolution of xenoliths from the country rock. Once sulfide saturation is achieved, segregation of droplets of sulfide liquid within the silicate magma will occur with subsequent accumulation at the base of the magmatic conduit by gravitational settling (Naldrett, 1999). Therefore, the highest concentrations of sulfides are concentrated where the geometry changes, specifically at the contacts between the country rock and the intrusion or flows (Barnes & Lightfoot, 2005). According to Holwell and McDonald (2010), after this separation, two crystallization phases occur in the sulfide droplets with decreasing temperature. The first phase consists of the crystallization of monosulfide solid solution (MSS) at 1000°C and the partitioning of Ni due to its compatibility, as well as Os, Ir, Ru, and Rh. The residual liquid is rich in Cu, Pt,

Pd, and Au, which partition into the intermediate solid solution (ISS) at around 900°C (the second crystallization phase). As the temperature decreases below 650°C, the MSS recrystallizes into pentlandite and pyrrhotite, and the ISS recrystallizes into chalcopyrite. Magmatic magnetite is also thought to crystallize at around 1000°C from an immiscible sulfide liquid (Naldrett, 1969; Ewers et al., 1976; Naldrett et al., 2000; and Fonseca et al., 2008)

Rock-fluid interactions in mafic-ultramafic rocks frequently generates serpentinization, amphibolitisation, and talc-carbonate after the primary magmatic phase (Chalokwu, 1985; Sassani & Pasteris, 1988; Barnes & Liu, 2012). These fluids typically originate from a variety of sources, including: i) magmatic fluids (Ripley et al., 1993; Moine et al., 2020), ii) crustal-derived fluids formed by partial melting of xenoliths and/or wall rock (Ripley & Alawi, 1988), iii) crustal-derived fluids formed by devolatilization/dehydration of wall rock in the contact between the basaltic magma and the crustal country rock (Ripley, 1981; Ripley & Al-Jassar, 1987), iv) meteoric fluids (Ripley et al., 1993). The interaction of these fluids commonly results in the mobilization of Cu, Au, Ni, S, and Fe, leading to the replacement of primary sulfides by silicates and secondary sulfides, as well as a reduction in mineral volume (Barnes & Liu, 2012; Holwell et al., 2017).

The principal objectives of this thesis were to 1) establish potential alteration episodes, determine secondary mineral assemblages, and identify the possible source of hydrothermal fluids, 2) determine the magmatic evolution and possible contamination sources that may have interacted with the parental magma of the Current Intrusion. These objectives were achieved by field work, sampling, and mineralogical and microtextural descriptions that were conducted and supported by scanning electron microscope (SEM) data. In addition, radiogenic Sr-Nd, stable O, and trace

elements were analyzed to determine possible sources of contamination, and stable isotopes of O-H were examined to identify the potential sources of the fluids.

2. REGIONAL GEOLOGY

2.1 Superior Province

The Superior Province is the largest Archean craton in the world and is found in the provinces of Quebec, Ontario, and Manitoba in Canada and in Minnesota in the USA (Hocq, 1994). According to Stott (1997), the Superior Province was consolidated as part of the accretion of multiple continental and oceanic terranes from 3.7 to 2.6 Ga.

One of the earlier classifications of the Superior Province is attributed to Card and Ciesielski (1986) who divided the province into four types of litho-tectonics domain: volcano-plutonic, metasedimentary, plutonic, and high-grade gneisses, which are differentiated from each other by structural style, lithology, geochronology, geophysics, and metallogenic attributes. Subsequently, Stott et al. (2010) proposed a revised classification into domains and terranes based on results of previous studies generated in provincial and federal mapping programs, Lithoprobe and Natmap programs, along with geochronological and geochemical studies. This classification defined "terranes," "domains," and "basins" (Fig. 2.1). Stott et al. (2010) defined "terranes" as a tectonically delimited region with internal characteristics different from the adjacent regions; "domains" as a typically young, lithologically distinct portion of a terrane, but with either juvenile crust or sharing a common basement; whereas they defined metasedimentary basins as a subdivision of terranes that are interpreted to have formed on the margin of larger terranes during the assembly of the Superior Province.

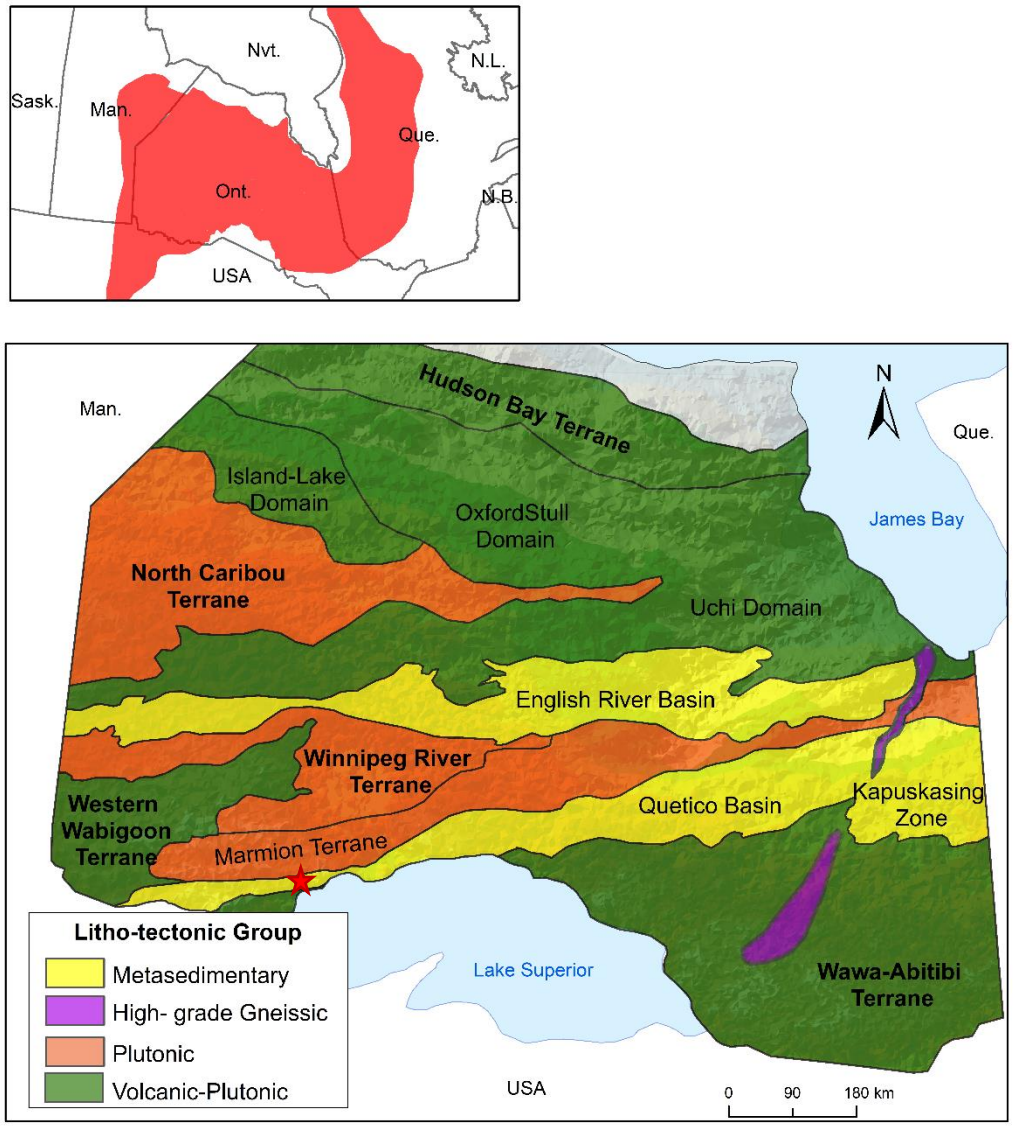

Figure 2.1 Schematic map of the western Superior Province. Modified from Stott et al. (2010). The red star indicates the location of the study area.

The plutonic subprovinces, such as the Winnipeg River, Marmion, and North Caribou, have U-Pb ages of zircons from 2.7 to 3.1 Ga (Li et al., 2020), are characterized by felsic and tonalitic plutons, and the rocks record a high degree of regional metamorphism and variable deformation (Card & Ciesielski, 1986). The volcano-plutonic provinces (U-Pb ages of zircons ranging from 2.7 to 3 Ga; Krogh & Turek, 1982) are characterized by metavolcanic supracrustal sequences, which are

intruded and bordered by plutonic rocks and that are commonly known as greenstone belts due to the low-grade metamorphism; they include the Wawa-Abitibi, Western Wabigoon, and Uchi subprovinces (Card & Ciesielski, 1986). The high-grade gneiss subprovinces, such as the Kapuskasing subprovince, have plutonic origins and are commonly characterized by amphibolite and granulite metamorphic facies (Card & Ciesielski, 1986) and have U-Pb ages of zircons ranging from 2.7 to possibly 3.0 Ga in metamorphosed areas in the late Archean or early Proterozoic (Percival & Card, 1983; Percival & Krogh, 1983). The metasedimentary subprovinces, such as the Quetico and English River subprovinces, are characterized by turbiditic wacke and pelite, with metamorphic grades that vary gradually from low-grade greenschist facies to high-grade granulite facies (Card & Ciesielski, 1986).

Percival et al. (2006) divided the tectonic evolution of the western Superior Province into five accretionary events: 1) the earliest episode consisted of the collision between the Northern Superior superterrane and the North Caribou superterrane at 2.72 Ga; 2) subsequently, the Winnipeg River terrane collided with the North Caribou superterrane (2.72-2.7 Ga), leading to the trapping of the synorogenic English River turbidites on the Uchi terrane margin; 3) later on, the Western Wabigoon terrane accreted to the Winnipeg River terrane margin between 2.71 and 2.70 Ga; 4) then, the Wawa Abitibi terrane collided with the Superior superterrane at 2.695 Ga; and 5) finally, the last event involved the accretion of the Minnesota River Valley terrane at 2.68 Ga and the entrapment of Pontiac turbidites.

2.1.1 Quetico Basin

The country rocks surrounding the Current deposit, the focus of this thesis, are part of the Quetico basin. The basin comprises an assemblage of metasedimentary rocks bounded by the volcanic and plutonic terranes of the Marmion and Western Wabigoon to the north and Wawa-Abitibi to the south (Mackasey et al., 1974). The basin extends through Minnesota, Ontario, and Quebec (Williams, 1991) and varies from 10 to 100 km wide (Percival, 1989). Davis et al. (1990) reported U-Pb dates on detrital zircons of 2.70-2.97 Ga in the north of the basin, whereas Zaleski et al. (1999) reported ages of <2.69 Ga in the south.

The Quetico Basin is primarily comprised of turbiditic quartz-rich metasedimentary rocks and igneous intrusions such as carbonatites and granites (Valli et al., 2004). According to Percival & Williams (1989), the sediments of the basin are thought to have formed in a forearc basin associated with turbiditic currents generated in submarine canyons (Percival & Williams, 1989). The metamorphic facies are mostly greenschist in the center of the basin; however, amphibolite and granulite facies have also been described (Percival & Williams, 1989). The northern boundary of the Quetico with the Wabigoon terrane is marked on the western end by the Rainy Lake-Seine River fault, which merges with the Quetico dextral fault that borders the Marmion terrane (Fig. 2.1; Percival, 1989). The total displacement of these faults is estimated at 100 km in a right lateral direction (Mackasey et al., 1974).

In the Lake Superior area, Paleoproterozoic Animikie Group sedimentary rocks are found overlaying the Quetico, specifically in the Thunder Bay area where sequences of the Gunflint Formation have been described, and these are overlain by Rove Formation shales and greywackes

(Kuntz et al., 2022). To the south of Lake Nipigon, sedimentary rocks of the Sibley Group (1,670 Ma to 1,450 Ma) are found above the Animikie Group (Kuntz et al., 2022). The final major Proterozoic event in the region was the deposition of the late Mesoproterozoic (Stenian) Keweenawan Supergroup (1,140 Ma and 1,090 Ma) which comprises a thick layer of subaerial lava flows, intrusive rocks in localized areas, and an upper sequence of sedimentary rocks that were deposited within grabens, developed within and around the Midcontinent Rift (Kuntz et al., 2022).

2.2 Midcontinent Rift System

The Midcontinent Rift System (MRS) formed at the end of the Mesoproterozoic in the interior of the Laurentian continent (Hinze & Chandler, 2020). Magnetic and gravity anomaly maps show that the MRS is 2500 km long (Hinze & Chandler, 2020), extending across the axis of Lake Superior to Michigan and Kansas in the United States (Sutcliffe, 1991).

Seismic reflection profiles demonstrate that the MRS extends for several kilometers along normal-graben faults, generating volcanic accumulations and flood basalts from the head of the Keweenawan mantle plume (Nicholson et al., 1997). Swanson-Hysell et al. (2019) suggested that the upwelling of this mantle plume was associated with an avalanche of subducted material between 1110 and 1085 Ma as the Laurentian continent moved from high to low latitudes with movements of about 27 cm/yr; this rapid movement resulted in collisional tectonics between Laurentia and the southernmost continents, Amazonia and Kalahari, which generated thermal subsidence and rift inversion along the MRS faults, and the Grenville orogeny between 1090 and 980 Ma in the assembly of the supercontinent Rodinia.

Woodruff et al. (2020) and Hinze & Chandler (2020) have divided the MRS and related mineral deposit type into five episodes: i) the early magmatism or Plateau stage between 1112 to ~1105 Ma, is attributed to a period of extension of the lithosphere with a massive magmatic event of mafic volcanic rocks and mafic-ultramafic intrusions, with conduit-type Ni-Cu-PGE sulfide deposits hosted in picritic and magnesium-rich magmas. The best-documented deposits of this type are Tamarak in Minnesota, Eagle in Michigan, and Current in Ontario. ii) the Rift stage, from ~1105 to ~1102 Ma, is characterized by voluminous eruptions of predominantly aluminum-rich flood basalts from shallower depths compared to the Plateau stage; these flows filled basins that subsided to form the modern Lake Superior basin. The magmatic deposits in this stage are associated with contact-type Cu-Ni-PGE sulfide deposits, found near the lower contact or margin of mafic to ultramafic layered intrusions (Zientek, 2012), as is the case of the basal contact between the magmas of the Duluth complex that intruded Archean and Paleoproterozoic rocks. iii) the late-stage Rift, from ~1090 to ~1083 Ma, is characterized by increased sedimentation, decreased magmatic activity, and accelerated basin subsidence associated with thermal relaxation consistent with decreasing Keweenawan mantle plume temperatures and intrusive activity. This stage is associated with magmatic-hydrothermal mineral deposits in the Mamainse Point and Thunder Bay areas, Ontario. iv) the post-rift stage, from ~1083 Ma to ~1040 Ma, is described as continuous sedimentation and subsidence of the Basin. This stage is associated with sediment-hosted stratiform Cu deposits near the Porcupine Mountains on the south shore of Lake Supeior. v) the compressional stage, the final episode, is attributed to northeasterly compression created by the Grenville orogeny, which created the current Lake Superior geometry of basalts riding over younger sedimentary rocks. This stage is associated with hydrothermal deposits such as native Cu and native Ag in basalt and interflow conglomerates in Michigan's western Upper Peninsula.

Two models have been proposed to explain the mechanism behind the continental rifting. One is an active rifting model (Cannon & Hinze, 1992), where crustal thinning and later extension spread laterally beneath the lithosphere was triggered by an upwelling mantle plume. Alternatively, a passive rifting model argues that the regional extension was induced by the collision and subduction of the Grenville Orogeny (Cannon & Hinze, 1992; Sutcliffe, 1991). Hollings and Cundari (2020) recently questioned the applicability of the active rifting model given the long duration of magmatic activity compared with the short time of other large igneous provinces and the lack of radiating dike swarms.

2.2.1 Thunder Bay North Intrusive Complex

The Mesoproterozoic Thunder Bay North Intrusive Complex (TBNIC) is located 50 km northeast of Thunder Bay, Ontario, Canada. The complex belongs to the Keweenawan Supergroup and consists of mafic to ultramafic intrusive rocks that comprise the Current, Escape, and Lone Island North and South intrusions (Fig. 2.2; Bleeker et al., 2020; Kuntz et al., 2022), which appear to be connected by a complex of dikes and sills confined to the Escape fault zone that is part of the southern zone of the Quetico fault system in the northeast portion of the MRS (Kuntz et al., 2022). Lithologically, the intrusions have been classified into varitextured and layered gabbro, lherzolite, feldspathic lherzolite, and olivine melagabbro, all of them lacking significant deformation or metamorphism (Kuntz et al., 2022). The TBIC intruded clastic metasedimentary rocks and granitoids of the Quetico Terrane (Kuntz et al., 2022).

The mineralization in the TBNIC has been considered to be associated with conduit-type deposits that intruded the Quetico Archean rocks (Woodruff et al., 2020; Brzozoski et al., 2023). The Escape

and Current intrusions contain most of the mineralization in the complex (Kuntz et al., 2022) with indicated mineral resources of 14.033 million tonnes grading 0.41% Cu, 0.25% Ni, and 2.7g/t Pt+Pd and an inferred mineral resource of 2.272 million tonnes grading 0.31% Cu, 0.19% Ni, and 1.6g/t Pt+Pd (Clean Air Merals Inc, 2023). The Lone Island Intrusion also contains some Pt-Pd-Cu-Ni mineralization (Kuntz et al., 2022).

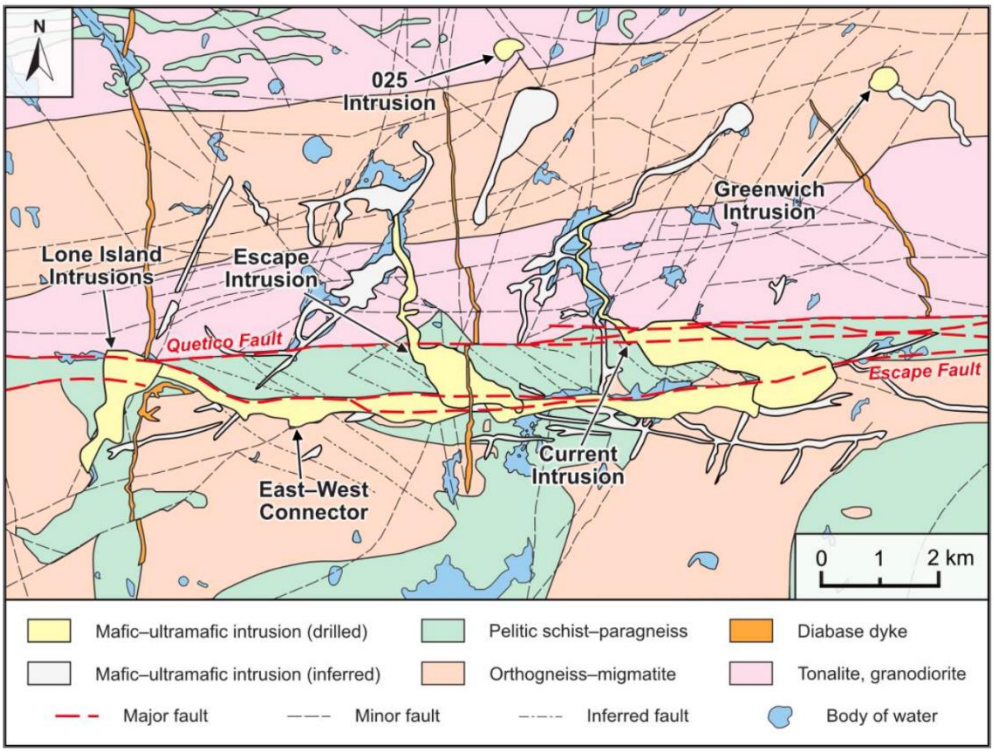

Figure 2.2: Regional geology map of the Thunder Bay North Intrusive Complex (modified after Thomas et at., 2011 and Caglioti, 2023)

2.2.1.1 Current Intrusion

The 1,106.6 ± 1.6 Ma Current Intrusion (Bleeker et al., 2020) comprises a melanocratic gabbro and peridotites hosting Cu-Ni sulfide mineralization linked to conduit-type magmas that intruded the Quetico rocks in the initial magmatic stages of the MRS (Woodruff et al., 2020; Bleeker et al.,

2020; Kuntz et al., 2022; Brzozowski et al., 2023). The intrusion is associated with multiple faults in the Quetico system, such as the Escape fault, part of the regional shear zone that crosses the boundaries between the Quetico basin and the Wabigoon terrane (Fig. 2.2; Williams, 1991). The intrusion present indicated minerals resource of 8.2 million tonnes grading 0.33% Cu, 0.22% Ni, and 2.7g/t Pt+Pd and an inferred mineral resource of 1.6 million tonnes grading 0.32% Cu, 0.20% Ni, and 1.7g/t Pt+Pd (Clean Air Merals Inc, 2023).

To date, the Current Intrusion has been divided into four mineralized zones (Fig. 2.3); i) the Current zone, from 30 to 70 meters wide and up to 70 meters thick, is hosted within a subhorizontal magmatic conduit or chonolith with a "bell shape," dipping to the southeast (Kuntz et al., 2022). The mineralization consists of sulfides such as pyrrhotite, pentlandite, chalcopyrite, pyrite, and rare cubanite and violarite (disseminated evenly throughout the ultramafic rock; Bleeker et al., 2020; Kuntz et al., 2022). ii) the Bridge zone resembles the Current zone in terms of geometry, but there are slight textural variations from disseminated to net textured sulfides (mineral grains connected to each other; Kuntz et al., 2022). iii) the Cloud and Beaver zones; the Cloud zone contains low percentages of sulfides with fine-grain size and disseminated texture (>1% modal abundances; Kuntz et al., 2022), whereas the Beaver zone is subdivided into East and West zones and is described as a tabular body; with dimensions from 100 to 500 m wide and from 15 to 150 m thick; the mineralization is located mainly along the basal contact of the intrusion with the Quetico metasedimentary rocks (Bleeker et al., 2020; Kuntz et al., 2022). In the Beaver West zone, the sulfides are accumulated in the depressions at the base of the intrusion that varies from massive to net and disseminated texture (Bleeker et al., 2020; Kuntz et al., 2022). Given the modal percentages of sulfides greater than 25%, this zone is considered as the area with the most prominent mineralization (Kuntz et al., 2022). The Beaver East zone, 200 meters thick and around

550 meters wide, contains disseminated mineralization accumulated in depressions at the base of the intrusion with modal percentages of sulfides from very low to 25% (Kuntz et al., 2022). iv) the 437-Southeast circular magnetic Anomaly (SEA) zone, described as the deepest part of the intrusion, hosts weak sulfide mineralization at the bottom of the zone (Kuntz et al., 2022). The Current deposit was emplaced along active conduits that served as magmatic pathways underlying older intrusions known as hybrids (Kuntz et al., 2022).

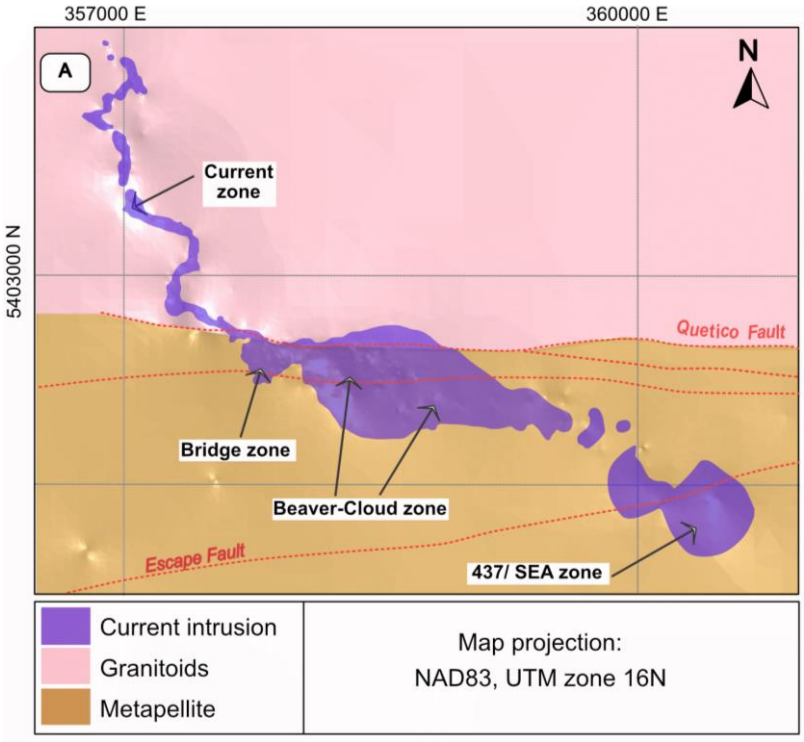

Figure 2.3: Geological model of the Current Intrusion and the country rock. Illustration modified from Thomas et al. (2011) and Good et al. (2015).

The initial magmatic phases of the TBNIC, the hybrids, are lithologically mafic to intermediate intrusions of leucogabbro, leucotroctolite, and monzonite, which contain large percentages of assimilated country rock and are located at the top of the mineralized intrusions (Kuntz et al., 2022). The hybrid rocks in the Current zone are relatively thin and begin to thicken in the Cloud-

Beaver zone becoming substantially thicker in the SEA zone (Kuntz et al., 2022). The hybrid/ultramafic contact is typically sharp; however, locally, it can be gradational over one to two meters (Kuntz et al., 2022).

According to Brzozowski et al. (2023), the crystallization in the intrusion began with the Current-Bridge Zone, followed by the Beaver-Cloud Zone, and ended with the 437-SEA Zone. These authors proposed that the sulfide was added to the system from two external sources: a shallow source attributed to the country rocks of the Quetico basin represented by $\Delta^{33}S$ values in the intrusion of <0.3‰ and high S/Se and a deeper source characterized by $\Delta^{33}S$ <3‰ and mantle S/Se values.

3. METHODS

3.1 Sampling

Sampling of the Current Intrusion was conducted in the summer of 2022. The drill holes used were distributed throughout the four mineralized zones of the deposit (Current, Bridge, Beaver-Cloud, and 347/SEA zone). To encompass a representative distribution of the ultramafic intrusion, the samples were selected based on the relationship between sulfides and silicates with distinctive degrees of alteration at different depths.

The 19 selected drillholes (Fig. 3.1) are distributed as follows: three from the Current zone (TBND086, TBND027, TBND097), two from the Bridge zone (BL09-163, BL10-329), nine from the Beaver-Cloud Zone (BL08-39, CL22-036A, BL10-267, BL08-15, BL10-258, BL08-69, BL11-390, BL11-399, BL10-341), and five from the 347/SEA zone (BL11-431, BL11-430, BL11-437, BL12-444, BL12-457). Four of the holes were selected for detailed petrographic, geochemical, and stable isotopic description and analysis (drill holes TBND086, BL08-39, CL22-036A, and BL11-431). From those four holes, a total of 83 hand samples were collected, of which 36 were made into thin sections, 25 were used for whole-rock geochemical analyses, and ten for oxygen and hydrogen isotopic analysis. Twenty-five samples from the remaining 15 drill holes were collected for whole rock geochemistry and hydrogen and oxygen isotopes; additionally, 10 of those 25 samples were selected for studies of radiogenic neodymium and strontium isotopes. Finally, three country rock samples (from drill holes TBND080, BL10-272, BL09-163, BL10-278) to represent the granitoid and the metapelites of the Quetico basin were collected for whole rock geochemical studies, oxygen and hydrogen isotopes, and thin sections.

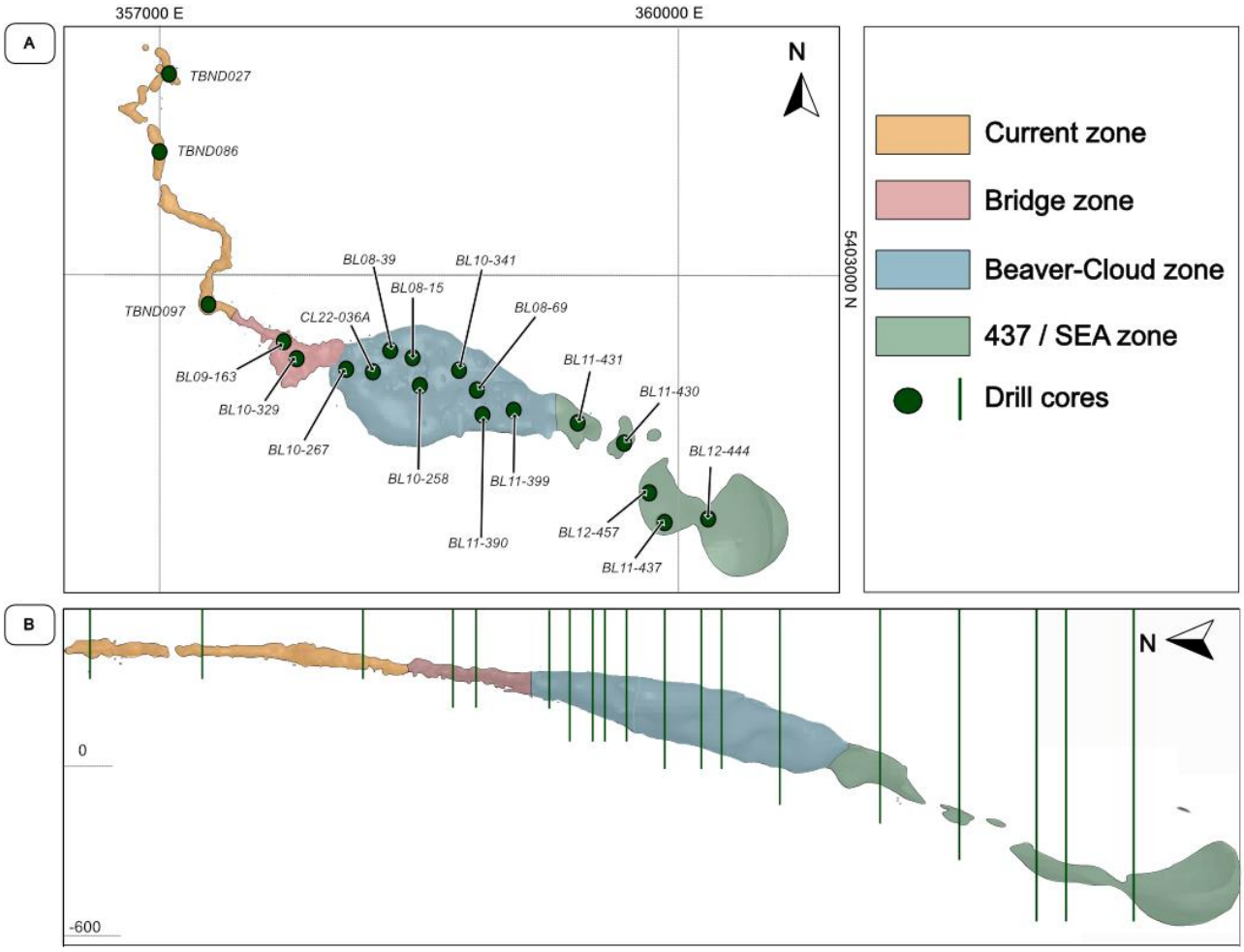

Figure 3.1: Distribution of selected drill cores within the intrusion. A. Plan view of the Current Intrusion and location of the drillholes (green dots). B. Location of the drill holes at depth in the long section facing east. Illustration compiled in Leapfrog using data provided by Clean Air Metals Inc.

3.2. Analytical Methods

3.2.1 Petrography

Polished thin sections were analyzed using the Olympus BX2M Microscope. The photomicrographs were taken using the Olympus SC180 camera in the Lakehead University Geology Department. Twenty-six polished thin sections were prepared at the Department of

Geology Lapidary Facility of Lakehead University, with an addition of ten prepared by Precision Petrographic Ltd, in Vancouver. Thirty-two thin sections are representative of the Current Intrusion, and four are of the country rock. Full petrographic descriptions of each thin section can be found in Appendix A.

3.2.2 Scanning Electron Microscopy

A scanning electron microscope (SEM) equipped with an Oxford Aztec 80mm/124eV Energy-dispersive X-ray spectrometer (EDS) in the Instrumentation Laboratory at Lakehead University was used for the chemical characterization of primary and secondary silicate minerals. The SEM electron gun operated with a voltage of 20 Kv. To ensure the X-ray measurement accuracy, the EDS was calibrated using a calcium silicate standard. The working distance between the thin section surface and detector was established at 15 mm, and the Z value, indicative of the stage height, was individually calibrated for each analysis. Prior to analysis, polished thin sections were carbon coated using an Edwards Auto 306 Carbon Coater. The complete data set for the SEM-EDS analysis is provided in Appendix C**.**

3.2.3 Whole Rock Geochemistry

Fifty-three samples (50 from the Current Intrusion and three from the country rock) were sent to ALS Geochemistry in Thunder Bay and analyzed using their complete characterization package (CCP-PKG01). The samples were prepared prior to analysis by grinding at least 70% of the sample to sizes smaller than 2 mm (package CRU-31); additionally, each split was pulverized to about 85% of particles passing 75 μm (package SPL-21). Inductively coupled plasma atomic emission

spectroscopy (ICP-AES) was used to obtain major-element oxides, infrared spectroscopy (LECO) to obtain total carbon and sulfur, aqua regia digestion and lithium borate fusion to obtain trace elements, and four-acid digestion and ICP-AES to obtain base metals. Prior to interpretation, all whole-rock data was recalculated on a volatile-free basis. The complete major and trace element dataset for the samples is provided in Appendix B.

3.2.4 Oxygen and Hydrogen Isotopes

Thirty-five representative samples (Appendix E) of the intrusion from the four mineralized zones of the deposit were selected for analysis of the bulk-rock $\delta^{18}O$ and $\delta^{2}H$ at the Queen's Facility for Isotope Research (QFIR). For oxygen isotope analysis, QFIR extracted approximately 5mg of oxygen from silicate samples at 550-600°C using the conventional BrF5 procedure of Clayton and Mayeda (1963) and analyzed via a dual inlet on a Thermo-Finnigan DeltaPlusXP Isotope-Ratio Mass Spectrometer (IRMS). For the hydrogen isotopic methodology, QFIR weighed the samples into silver capsules, degassed for 1 hour at 100°C; then the samples were crushed, and loaded into a zero-blank autosampler. The hydrogen isotopic composition was measured using a MAT 253 Stable Isotope Ratio Mass Spectrometer coupled to a Thermo Scientific TC/EA High-Temperature Conversion Elemental Analyzer.

$\delta^{18}O$ and $\delta^{2}H$ values are reported using the delta (δ) notation in units per mill (‰) relative to the Vienna Standard Mean Ocean Water (VSMOW) international standard, with a precision of 0.4‰ for O isotopes and 1.5‰ for H isotopes.

3.2.5 Strontium and Neodymium Isotopes

Ten bulk-rock samples from the Current Intrusion were submitted for Sm-Nd isotope analyses at the Isotope Geochronology and Geochemistry Research Centre (IGGRC) at Carleton University. Prior to dissolution in a concentrated HF-HNO_3 solution, the bulk-rock was doped with a ^{148}Nd mixed spike. In preparation for ion exchange chromatography, the sample residues were brought up in 1.5 mL of 2.5 N HCl. A thermo-Finnigan Neptune multi-collector ICP-MS was utilized to measure Sr and Nd isotope ratios. The Sr and Nd isotopic ratios were standardized to $^{86}Sr/^{88}Sr$ = 0.1194 and $^{146}Nd/^{144}Nd$ = 0.7219. The $^{143}Nd/^{144}Nd$ ratios were rectified for the offsets using bracketing JNdi-1 mean values against an IGGRC Thermo-Finnigan Triton TIMS average JNdi-1 value of 0.512100. Sr and Nd isotopes ratios are reported as initial values (Sr_i and ε_{Nd}) and are recalculated to an age of 1106.6 Ma, which is the time of the Current Intrusion crystallization (Bleeker et al., 2020). The full data set can be found in Appendix D.

4. RESULTS

4.1 Petrography

Petrographic descriptions were completed using polished thin sections under transmitted and reflected light for mineralogical and textural characterization of both primary and secondary silicates, sulfides, and oxides (Appendix A). The methodology of Simmons and Christenson (1994) was utilized to describe the alteration intensity (increase of secondary minerals over primary minerals measured in percentage: weak alteration 0-33.3%, moderate alteration 33.4-66.6%, and strong alteration 66.7-100%). Grain sizes are reported as very fine-grained (<0.01 mm), fine-grained (0.01-1 mm), medium-grained (1-5 mm), and coarse-grained (5 mm-2 cm). The point counting grid method was used to determine accurately mineral abundance (the 20 x 20 mm grid was divided into 2 mm square cells; the percentage of mineral abundance was calculated: #grids containing a specific mineral*total of grids/ total of grids*100)

4.1.1 Rock Type

Samples for the Current Intrusion comprise a peridotite unit (n=28) consisting of fine-grained wehrlite and lherzolite (Fig. 4.1B and Fig. 4.2A), characterized by modal abundances of 40-70% olivine, 0-3% orthopyroxene, 5-25% clinopyroxene, and 5-15% plagioclase. In addition, a gabbro unit was also identified (n=4), specifically, olivine gabbronorite ± troctolite (Fig. 4.1A and 4.2B), distinguished by modal abundances of 40-55% plagioclase, 35-45% olivine, and 5-10% pyroxene.

Subhedral plagioclase and pyroxene were observed in 10% of the samples analyzed; in the remaining 90%, the crystals were anhedral. In contrast, olivine crystals had anhedral habits in all

samples analyzed. Texturally, the rocks demonstrate up to 100% replacement of pre-existing primary minerals with variations in the intensity of alteration between selective and pervasive.

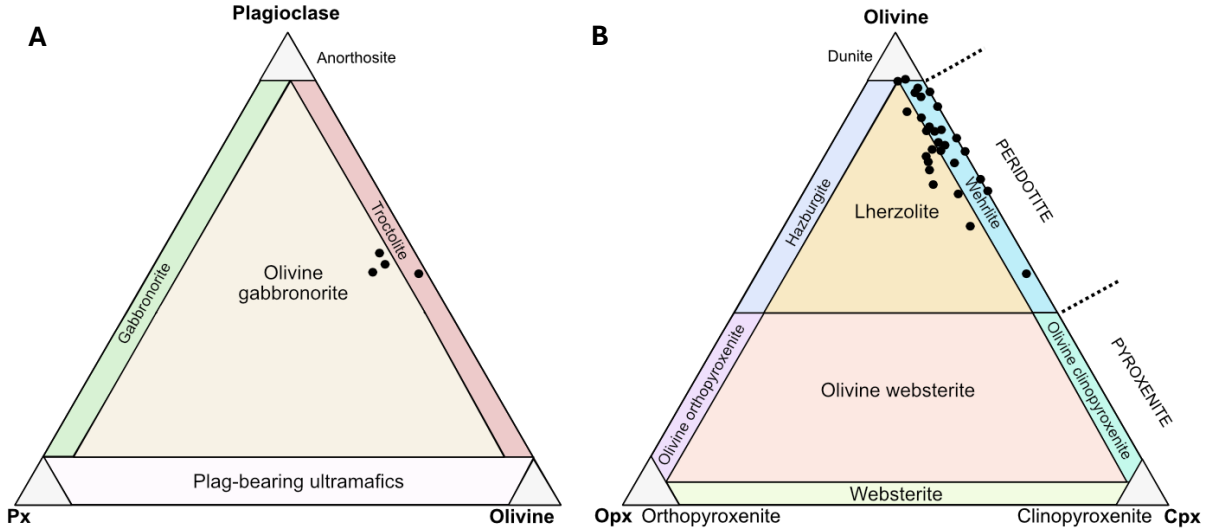

Figure 4.1: IUGS ternary diagrams for mafic (A) and ultramafic (B) rocks for samples from this study (after Streckeisen, 1974). The modal classification was based on the proportions of pyroxenes, olivine, and plagioclase.

The primary sulfides are disseminated and interstitial to silicates, with abundances from absent to 9%, averaging 50% pyrrhotite, 40% chalcopyrite, 9% pentlandite, 1%cubanite. The sulfides are characterized by subhedral to anhedral habits and subsolidus textures such as pentlandite flames in pyrrhotite. Replacement textures are visible with up to 100% replacement by secondary sulfides or magnetite.

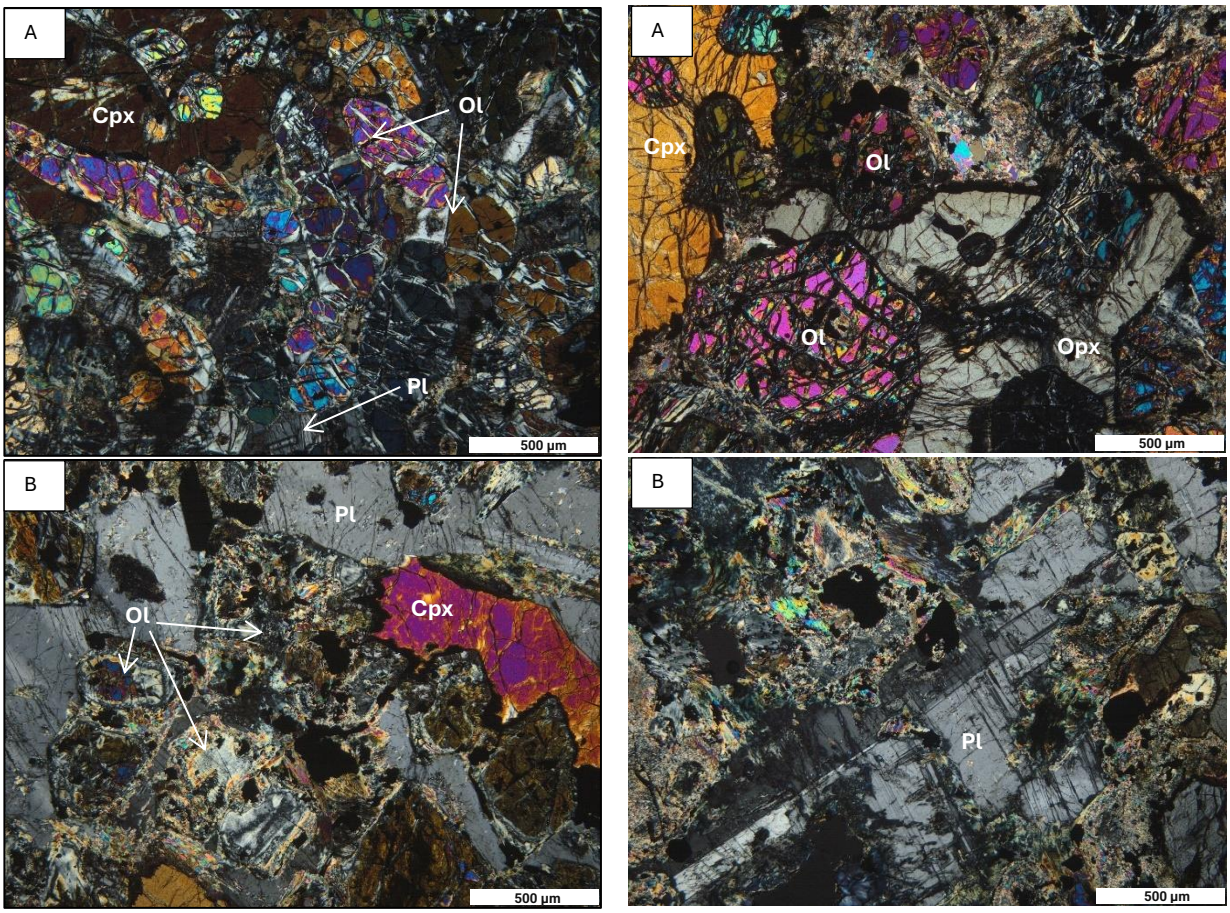

Figure 4.2: Photomicrographs in XPL. A: fine-to-medium-grained wehrlite with poikilitic texture (sample CAM-AC-22-50 from drillhole Bl11-431 at 458.63m depth). B: medium-grained olivine gabbronorite with poikilitic texture (sample CAM-AC-22-84 from drillhole CL22-036A at 211.93 m depth). Abbreviations: Ol- olivine; Cpx-clinopyroxene; Opx-orthopyroxene; Pl- plagioclase.

The percentage of alteration intensity was measured based on the replacement of the major minerals, olivine, plagioclase, and pyroxene (Fig. 4.3). Samples for the Current zone are characterized by weak alteration in most samples (five samples) and moderate alteration in one sample (CAM-AC-22-05). The Beaver-Cloud zone samples exhibit moderate alteration in the majority of samples (nine samples) and weak alteration in four samples (in drillhole BL08-39; samples CAM-AC-22-15, CAM-AC-22-31, CAM-AC-22-33 and in drillhole CL22-036A the

sample CAM-AC-22-77). The 437-SEA zone samples are characterized by strong alteration located at the top and bottom of the intrusion (four samples: CAM-AC-22-35, CAM-AC-22-36, CAM-AC-22-41, and CAM-AC-22-66) and weak to moderate alteration in the center of the intrusion (eight samples).

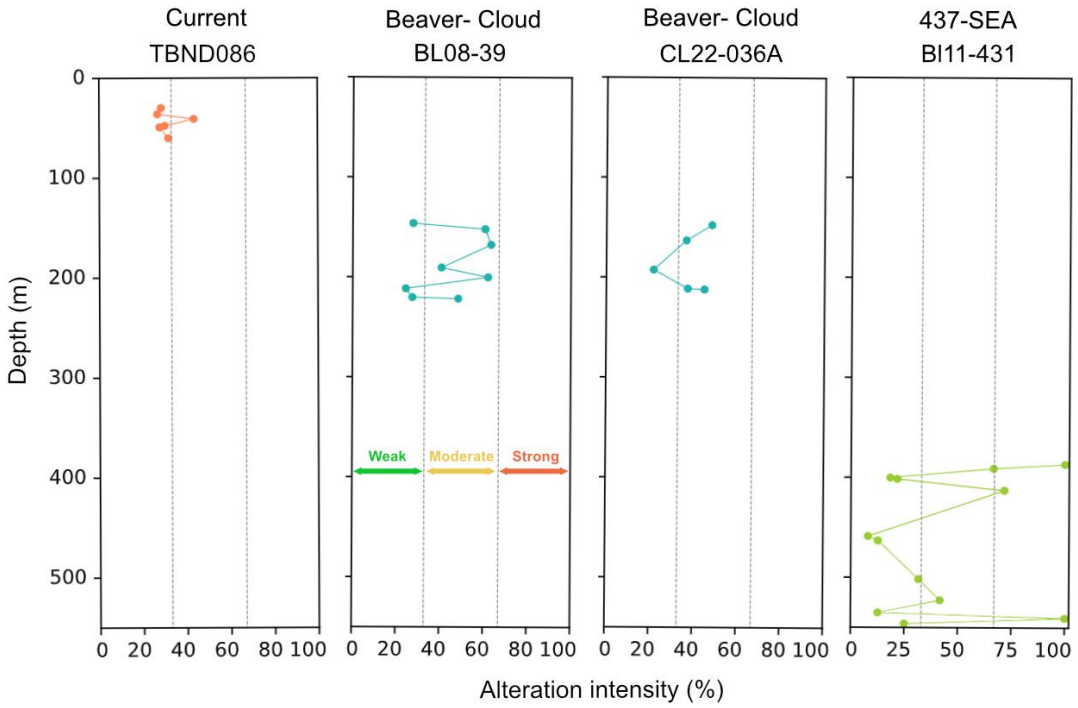

Figure 4.3: Alteration intensity in percentage versus depth in four drillholes of three mineralized zones of the Current Intrusion. Drillhole TBND086 in the Current zone, drillhole BL08-39 and CL22-036A in the Beaver-Cloud zone, and drillhole Bl11-431 in the 437-SEA zone. The intensity of alteration is defined as weak (0 and <33.3%), moderate (>33.34 and <66.66%), and strong (<66.67 and 100%).

Three assemblages of secondary minerals have been identified in the intrusion (Table 4.1 and Fig.4.4). Domain A is characterized by the replacement of 10-90% of olivine by antigorite, secondary magnetite ± actinolite-tremolite, as well as the replacement of pyroxenes in boundaries and along fractures by actinolite-tremolite, chlorite, antigorite (weak to moderate replacement; 10 to 60%), and epidote, sericite, and chlorite after plagioclase with weak to moderate replacement

(5-60%). Domain B is characterized by the replacement of 20-100% of the antigorite, olivine, and pyroxene by lizardite-chrysotile, and chlorite, epidote, sericite replacing plagioclase, with moderate to strong alteration intensity (30-80%). This Domain presents an increase of sizes and modal abundance of sericite, epidote, and chlorite compared to Domain A. Domain C is characterized by the replacement with up to 100% of secondary minerals from domains A and C by talc and carbonates. Secondary magnetite and secondary pyrite are present in domains A and B, replacing pyrrhotite, chalcopyrite, pentlandite, and primary magnetite, with up to 100% replacement in pyrrhotite and primary magnetite, 50% in pentlandite and, 20% in chalcopyrite. Secondary pyrrhotite after secondary pyrite is observed only in Domain A.

Table 4.1: Mineral assemblages (domains) of secondary minerals in the Current Intrusion.

	Secondary silicates							Secondary Sulfides		Secondary oxides	
Mineral domains	Antigorite	Lizardite-chrysotile	Chlorite	Epidote	Actinolite-tremolite	Talc	Sericite	Pyrite	Pyrrhotite	Magnetite	Carbonates
Domain A	+		+	+	+		+	+	+	+	
Domain B	+	+	+	+			+	+		+	
Domain C						+					+

+major mineral (>1%)

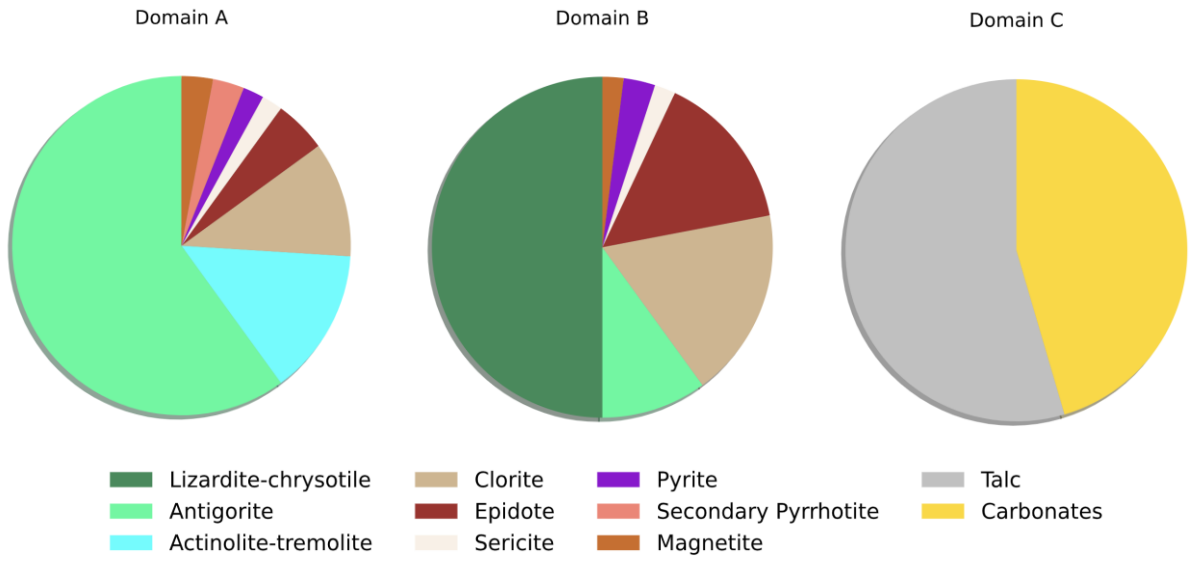

Figure 4.4: Average modal abundances of secondary minerals in Domains A, B, and C.

4.1.2 Primary Magmatic Phases

4.1.2.1 Primary Silicates

Olivine is typically fine- to medium-grained, with alteration intensity that varies from weak to strong (Fig. 4.5) by serpentine group minerals, magnetite ± actinolite-tremolite. The typical textures are mesh texture (initial stage of replacement by serpentine group minerals with concentric growth in fractures and boundaries of the olivine; Fig. 4.5 A) and bastite texture (final stage of replacement characterized by the pervasive alteration of olivine by secondary silicates and magnetite; only relict textures are recognized; Fig. 4.5 B).

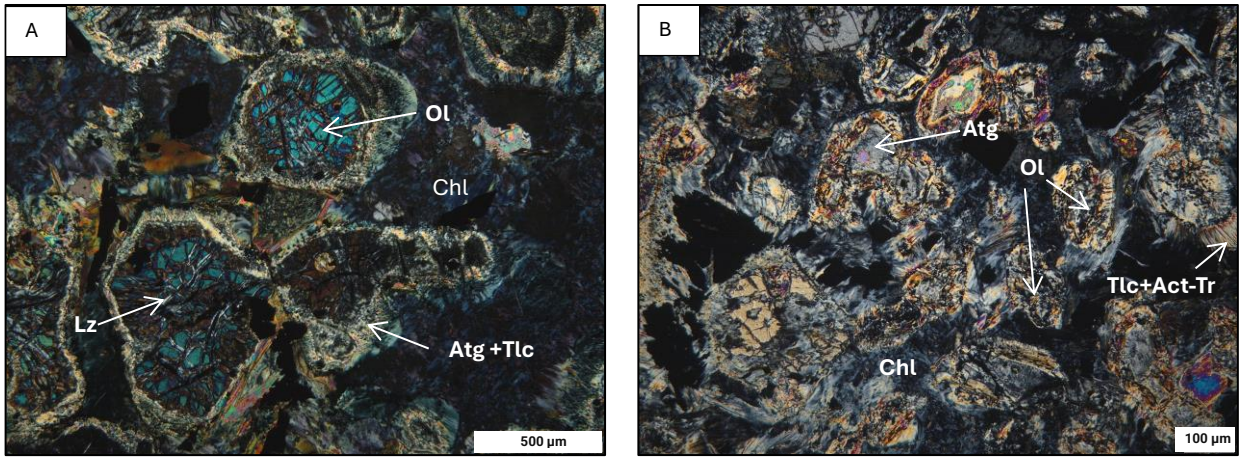

Figure 4.5: Photomicrographs in XPL. A: lherzolite with fine-grained olivine with mesh texture due to the replacement of serpentine group minerals and talc (sample CAM-AC-22-52 from drillhole Bl11-431 at 463.13m depth). B: troctolite with fine-grained olivine with bastite texture generated by the replacement of serpentine group minerals and talc, actinolite-tremolite (sample CAM-AC-22-69 from drillhole CL22-036A at 147.57 m depth). Abbreviations: Ol- olivine; Atg- antigorite; Lz- lizardite; Tlc- talc; Tr- tremolite; Act- actinolite; Chl-Chlorite.

Plagioclase (anorthite ± labradorite) is commonly medium-grained, exhibits polysynthetic and Carlsbad twinning, and occurs interstitially in pyroxenes and olivine. The alteration intensity varies from weak to strong but is dominantly weak. Plagioclase is typically replaced by fine- to medium-grained epidote and chlorite and, in selective areas, to sericite (Fig. 4.6).

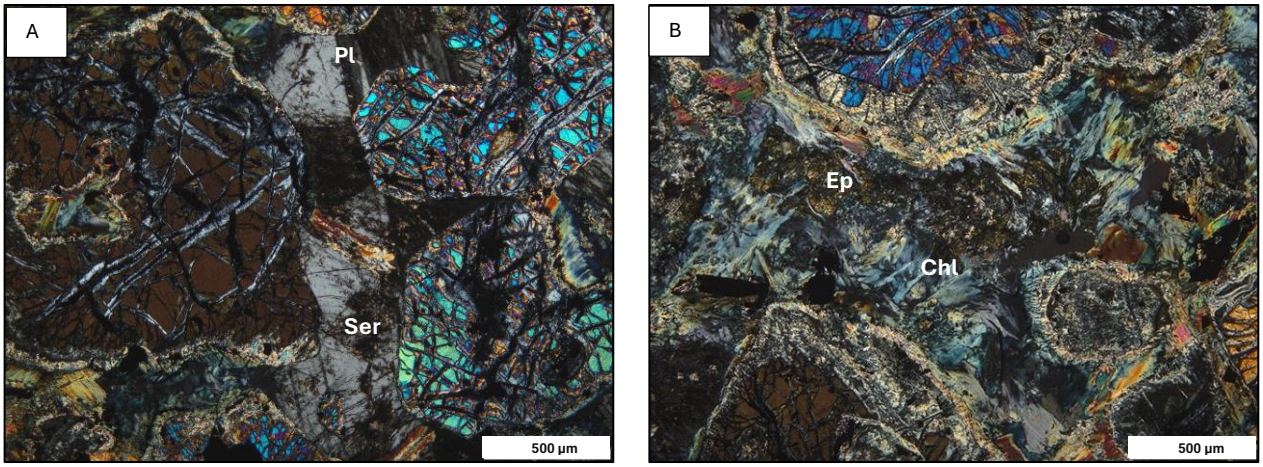

Figure 4.6: Photomicrographs in XPL. A: wehrlite with medium-grained plagioclase with weak alteration to sericite (sample CAM-AC-22-28 from drillhole Bl11-431 at 200.08m depth). B: lherzolite with medium-grained plagioclase with strong alteration to epidote (sample CAM-AC-22-77 from drillhole CL22-036A at 192.4m depth). Abbreviations: Pl- plagioclase; Ser- sericite; Ep- epidote; Chl- chlorite.

Fine- to medium-grained pyroxenes occur as oikocrysts enclosing smaller olivine. Augites, and enstatite are common. The intensity of alteration varies between weak to moderate but is generally weak. Replacement occurs along fractures and edges of pyroxenes, with common crystallization of chlorite, actinolite-tremolite, and serpentine (Fig. 4.7).

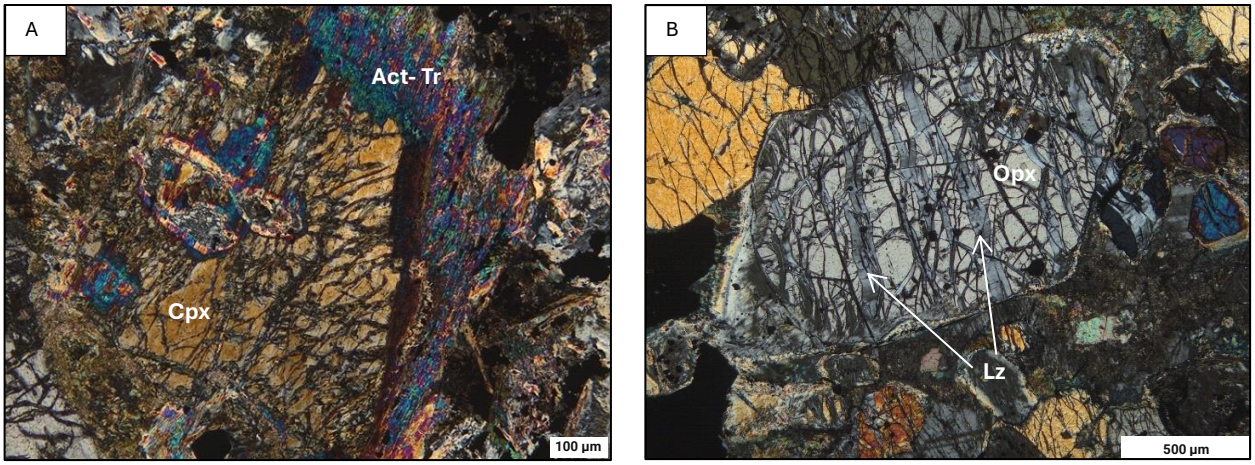

Figure 4.7: Photomicrographs in XPL. A: wehrlite with fine-grained pyroxene with moderate alteration to actinolite-tremolite (sample CAM-AC-22-34 from drillhole Bl11-431 at 221.55m depth). B: wehrlite with medium-grained clinopyroxene with strong alteration to lizardite-chrysotile (sample CAM-AC-22-37 from drillhole CL22-036A at 400.1m depth). Abbreviations: Cpx- clinopyroxene; Opx- orthopyroxene Lz- lizardite; Tr- tremolite; Act- actinolite.

4.1.2.2 Primary Sulfides

Sulfides occur interstitially in silicates; the abundance varies systematically with depth in the intrusion, from absent to 9% (the highest percentages are accumulated at the bottom of the intrusion). In order of abundance, the sulfide assemblages consist of pyrrhotite, chalcopyrite, pentlandite ± cubanite (Fig. 4.8). The intensity of alteration of primary sulfides varies from absent to strong, commonly along fractures and mineral boundaries. The alteration minerals in order of abundance are pyrite and magnetite.

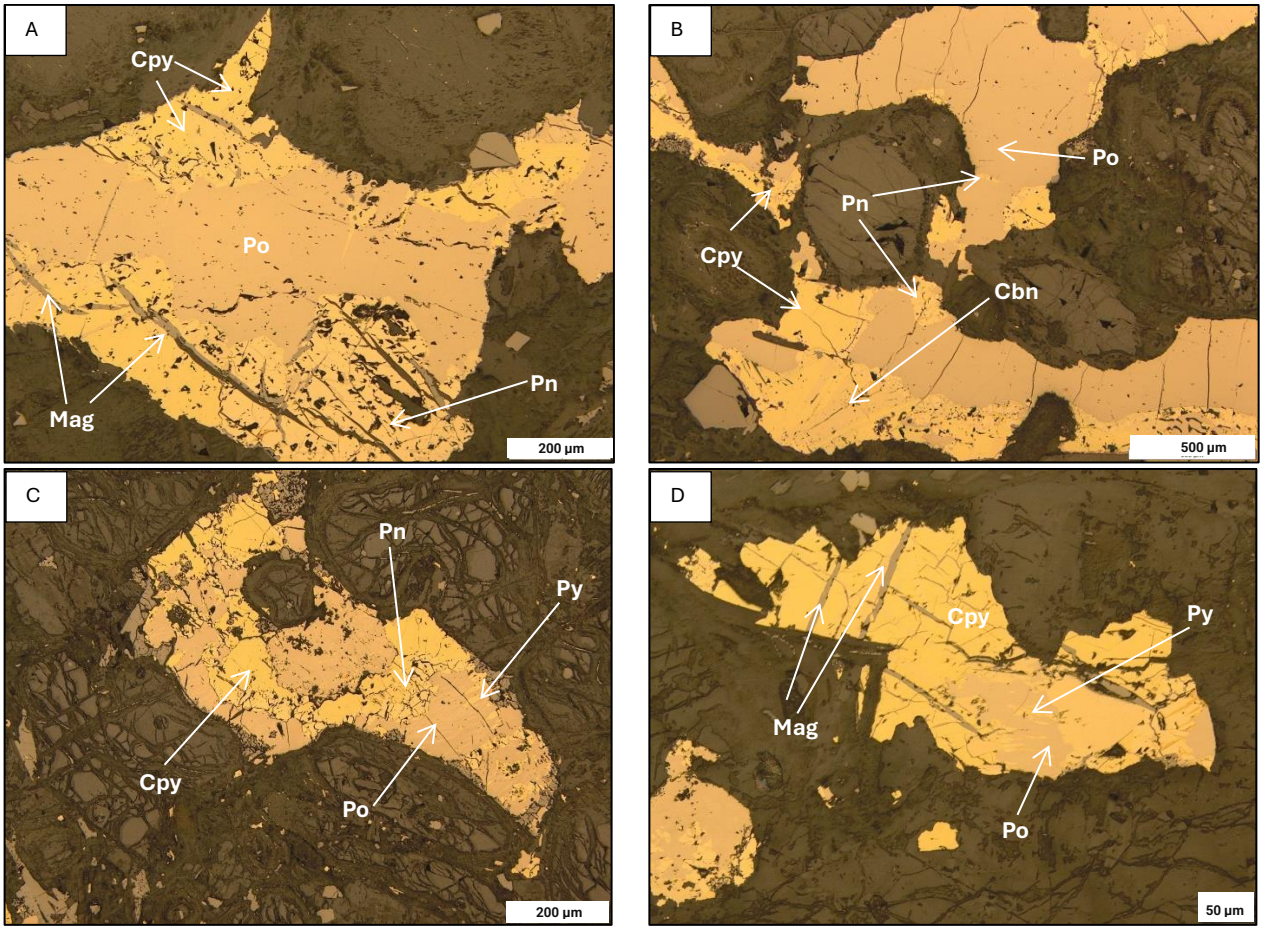

Figure 4.8: Photomicrographs in PPL. A: wehrlite with fine-to-medium-grained pyrrhotite, fine-grained chalcopyrite, and fine-grained pentlandite. Pentlandite and chalcopyrite are weakly altered by magnetite (sample CAM-AC-22-37 from drillhole Bl11-431 at 400.1m depth). B: lherzolite with medium-grained pyrrhotite with very fine-grained pentlandite exsolutions. Medium-grained chalcopyrite with fine-grained cubanite exsolutions (sample CAM-AC-22-38 from drillhole Bl11-431 at 401.46m depth). C: lherzolite with fine -grained pyrrhotite, chalcopyrite and pentlandite. Pyrrhotite is weakly altered by pyrite (sample CAM-AC-22-56 from drillhole Bl11-431 at 501.49m depth). D: wehrlite with fine-grained pyrrhotite and chalcopyrite. Chalcopyrite is weakly altered to magnetite and Pyrrhotite is moderate altered by pyrite (sample CAM-AC-22-31 from drillhole BL08-39 at 211.42 m depth). Abbreviations: Po- pyrrhotite; Cpy- chalcopyrite; Pn- pentlandite; Mag- magnetite, Cbn- cubanite.

4.1.2.3 Primary Oxides

The oxides of primary magmatic origin, in order of abundance, are magnetite, chromite, and ilmenite (Fig. 4.9). Very fine-grained chromite commonly occurs within phenocrysts of pyroxene and olivine, with abundances from 0.1-0.5%. Fine-grained magnetite occurs interstitially between silicates; the abundance varies from 1-2%. Magnetite is observed with strong alteration in some samples at the top of the intrusion, replaced by chlorite and pyrite. Ilmenite was observed as an exsolution of magnetite with trellis and sandwich-type lamellae with an abundance of 0.1%.

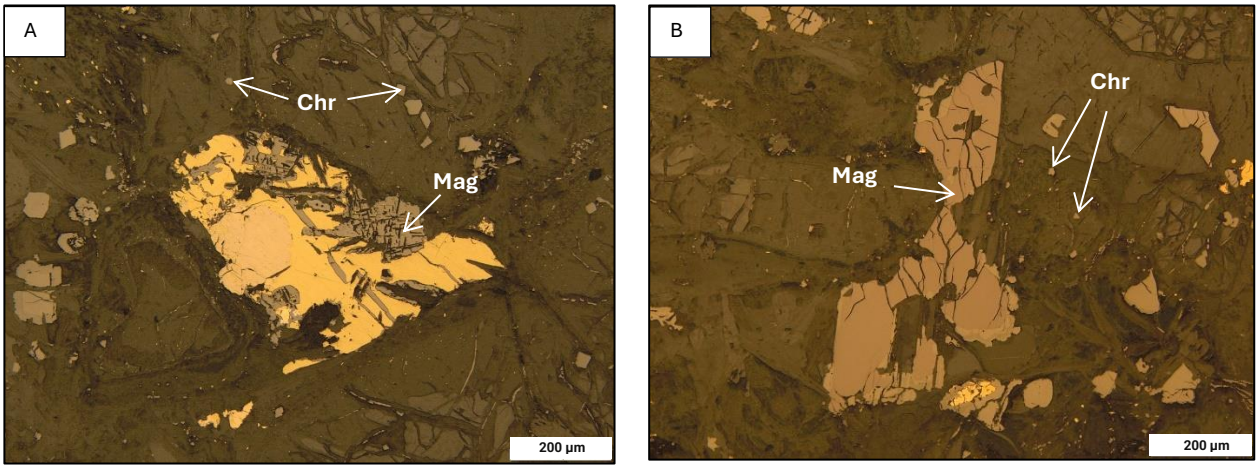

Figure 4.9: Photomicrograph in XPL: A and B: lherzolite with fine-grained magnetite and very fine-grained ilmenite and chromite (sample CAM-AC-22-71 from drillhole CL22-036A at 162.94 m depth). Abbreviations: Mag- magnetite; Ilm- ilmenite, Chr- chromite.

4.1.3 Secondary Phases

4.1.3.1 Secondary Silicates

Serpentine group minerals vary in abundance with depth. Generally, antigorite is located at the upper and lower areas of the intrusion, whereas lizardite-chrysotile is dominant in the center. The lizardite presents hourglass, mesh (Fig. 4.10 A), and bastite textures (Fig. 4.10 D) due to the replacement of olivine, pyroxene, and antigorite, commonly occurring in fractures and the centers

of olivine and pyroxenes. The chrysotile occurs in irregular veins with fibrous texture (Fig. 4.10 B), crosscutting primary and secondary silicates and intergrowing with lizardite in the replacement of olivine, pyroxenes, and antigorite (with abundances varying from absent to 80% compared to other secondary silicates). Antigorite occurs as felted fibrous shapes with flaky crystals (abundance of 0 to 40%), mainly observed replacing the edges of olivine and pyroxenes phenocrysts (Fig. 4.10 A) and, in some cases, with bastite texture (Fig. 4.10 C).

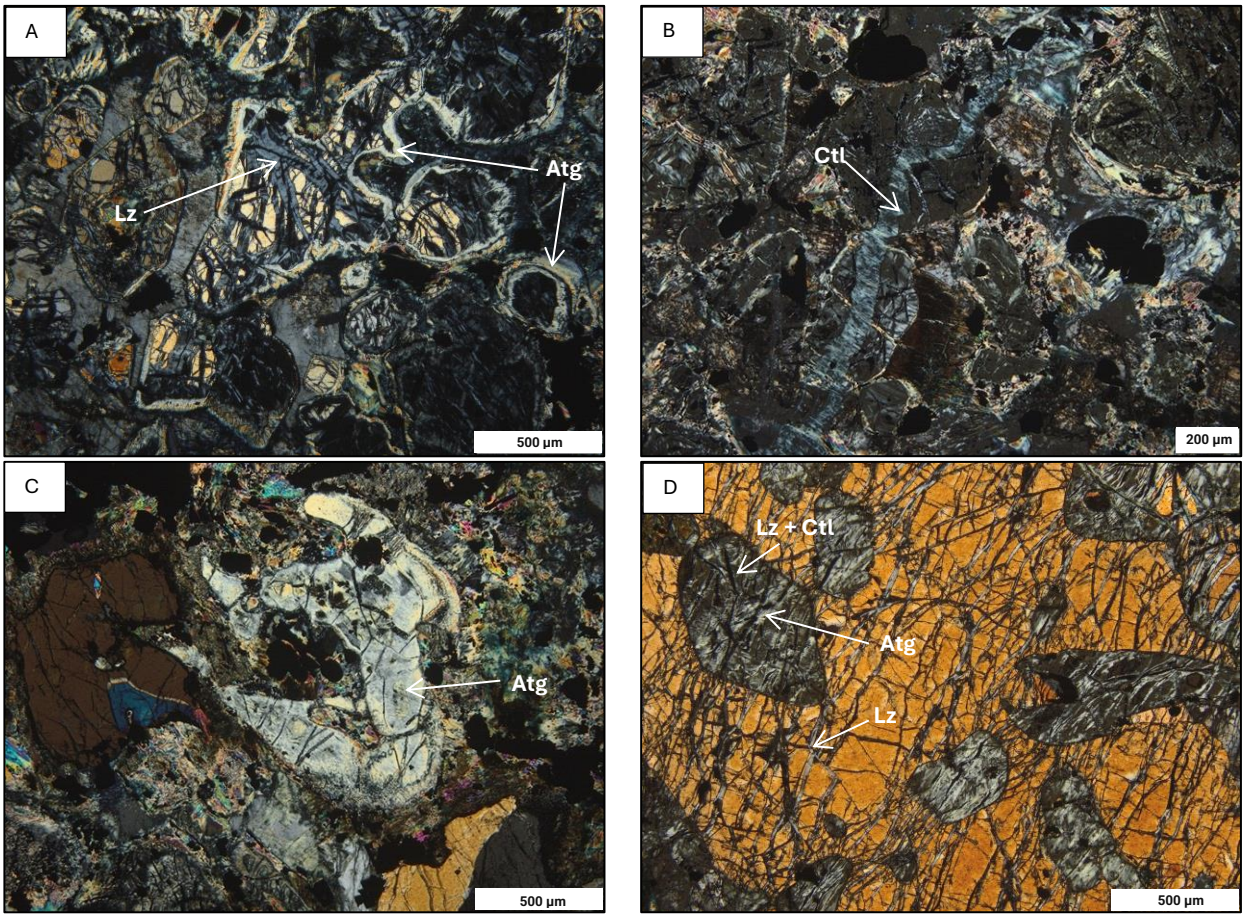

Figure 4.10: Photomicrographs in XPL. A: lherzolite with antigorite replacing the boundaries of olivine and lizardite-chrysotile alteration along fractures in olivine (sample CAM-AC-22-71 from drillhole CL22-036A at 162.94m depth). B: wehrlite with vein of chrysotile (sample CAM-AC-22-28 from drillhole BL08-39 at 199.98m depth). C: wehrlite with olivine with bastite texture due to antigorite replacement (sample CAM-AC-22-83 from

drillhole CL22-036A at 211.93m depth). D: wehrlite with olivine with bastite texture due to antigorite and Lizardite replacement (sample CAM- AC-22-83 from drillhole CL22-036A at 211.93m depth). D: wehrlite with olivine with bastite texture due to antigorite and lizardite replacement (sample CAM- AC-22-12 from drillhole TBND086 at 60.07 m depth). Abbreviations: Lz- lizardite; Atg- antigorite; Ctl- chrysotile.

Fine- to very fine-grained chlorite is closely associated with the alteration of plagioclase; however, it is also selectively observed in magnetite and ferromagnesian minerals such as pyroxene and actinolite-tremolite. It occurs with a blue fibrous texture and low birefringence. Its abundance varies from absent to 60% (Fig. 4.11).

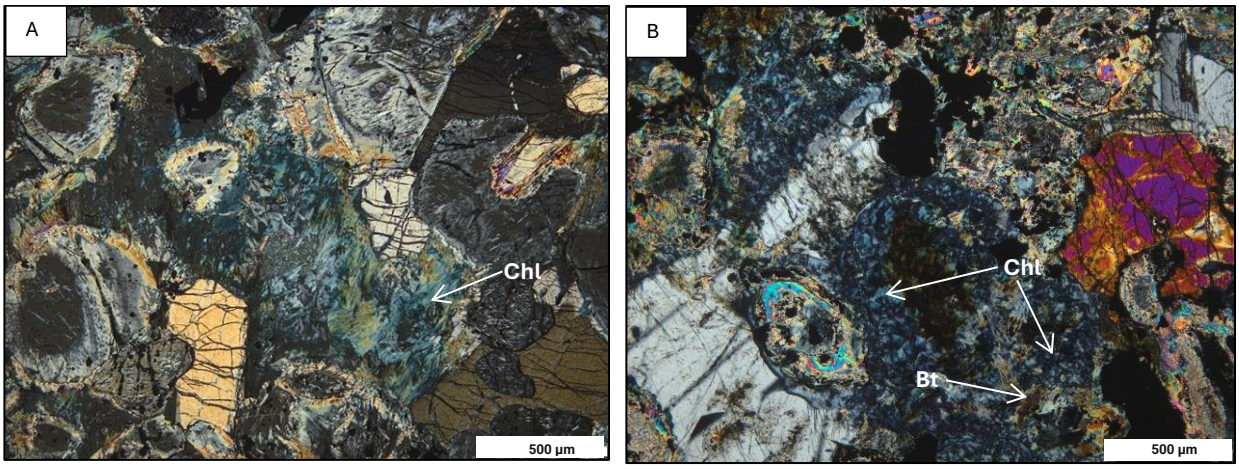

Figure 4.11: Photomicrographs in XPL. A: wehrlite with fine- to very fine-grained chlorite altering plagioclase (sample CAM-AC-22-37 from drillhole Bl11-431 at 400.1 m depth). B: wehrlite with fine- to very fine-grained chlorite altering plagioclase and ferromagnesian minerals (sample CAM-AC-22-83 from drillhole CL22-036A at 211.93 m depth). Abbreviations: Chl- chlorite; Bt- biotite.

Actinolite-tremolite with acicular to fibrous textures. The grain size varies from fine- to very fine-grained with abundances from absent to 5%. Actinolite-tremolite is observed as alteration rims around pyroxenes (uralite) with weak to moderate replacement (Fig. 4.12) and is associated with

talc altering the boundaries of olivine. Selective weak alteration of actinolite-tremolite to chlorite was also observed.

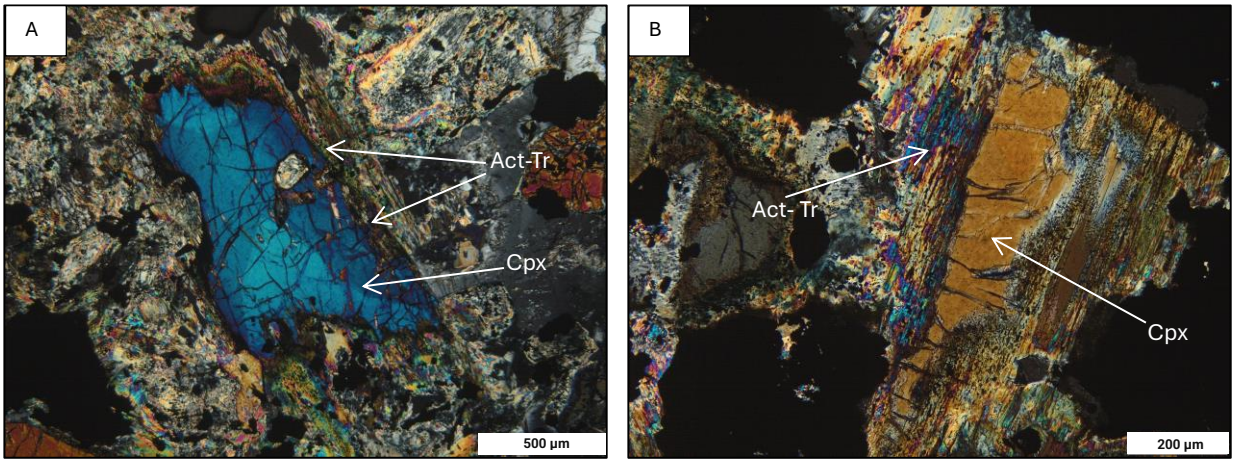

Figure 4.12: Photomicrographs in XPL. A: wehrlite with fine- to very fine-grained actinolite-actinolite-tremolite altering clinopyroxene (sample CAM-AC-22-82 from drillhole CL22-036A at 211.09 m depth). B: wehrlite with fine- to very fine-grained actinolite-actinolite-tremolite altering clinopyroxene (sample CAM-AC-22-83 from drillhole CL22-036A at 211.93 m depth). Abbreviations: Cpx- clinopyroxene; Tr- tremolite; Act- actinolite.

Talc occurs as fine- to very fine-grained aggregates with fibrous to radial textures with abundances that vary from absent to 50%. Talc is associated with the replacement of serpentine (Fig. 4.13 A) with up to 100%. Talc was observed widely associated with carbonates.

Epidote occurs as fine- to very fine-grained aggregates. Generally, epidote has high birefringence that varies from strong green to yellow pinkish with abundances that vary from absent to 40%. Epidote alters the plagioclase pervasively and mainly at the top and bottom of the intrusion (Fig. 4.13 B), with lower occurrence in the center of the intrusion.

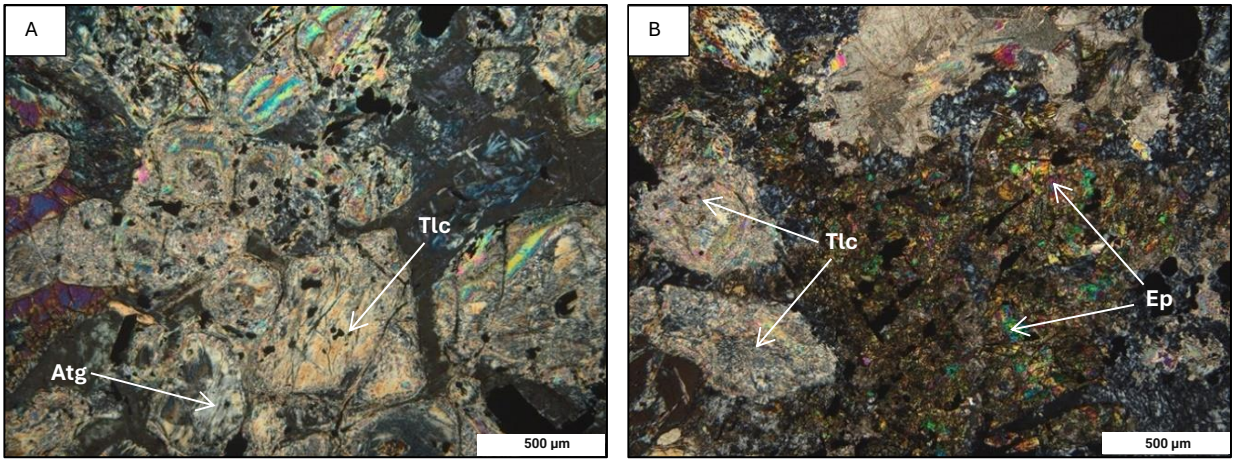

Figure 4.13: Photomicrographs in XPL. A: wehrlite with very fine-grained talc replacing serpentine group minerals (sample CAM-AC-22-34 from drillhole BL08-39 at 221.55 m depth). B: wehrlite with fine- to very fine-grained epidote replacing plagioclase (sample CAM-AC-22-41 from drillhole Bl11-431 at 412.62 m depth). Abbreviations: Tcl- talc; Atg- antigorite; Ep- epidote.

The classification of biotite as primary or secondary silicate was inconclusive due to its high alteration along the boundaries; however, given the size and anhedral boundaries in less altered phases, it appears to be secondary. The mica, typically fine-grained, varies from absent to 5% with anhedral outlines and birds eye textures. It commonly occurs interstitially in silicates, and its abundance typically increases towards the top of the intrusion. The biotite is replaced by chlorite with a moderate to strong alteration intensity (Fig. 4.14).

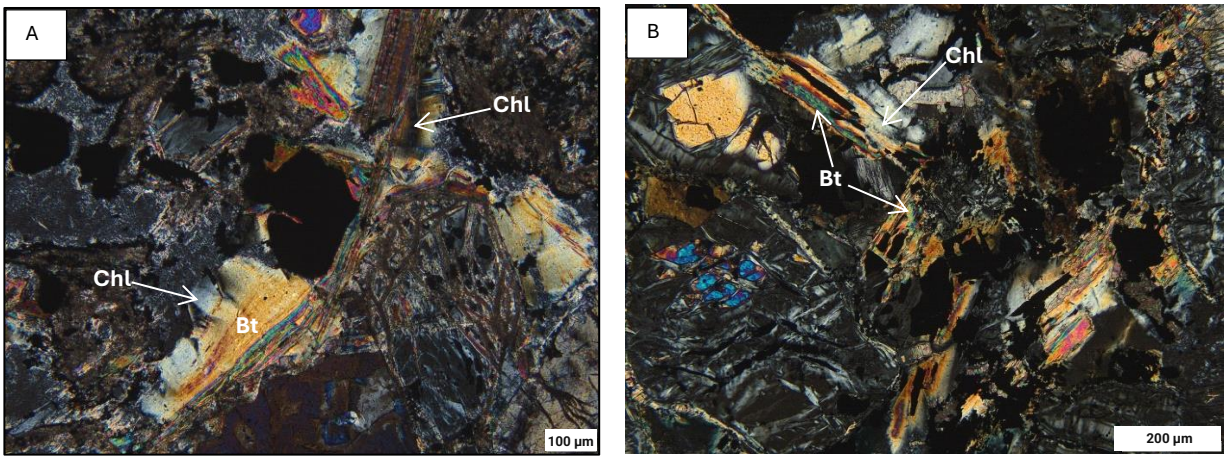

Figure 4.14: Photomicrographs in XPL. A: wehrlite with fine-grained biotite with weak to moderate alteration to chlorite (sample CAM-AC-22-03 from drillhole TBND086 at 36m depth). B: wehrlite with fine-grained biotite with weak alteration to chlorite (sample CAM-AC-22-02 from drillhole TBND086 at 29.9m depth). Abbreviations: Chl- chlorite; Bt- biotite.

4.1.3.2 Secondary Sulfides

In order of abundance, the secondary sulfides are pyrite (from absent to 5%) and pyrrhotite (from absent to 2%). Commonly, pyrite alteration begins at the boundaries and fractures in pyrrhotite with alteration ranging from weak to strong. Secondary pyrrhotite was observed after secondary pyrite (Fig. 4.15 B) with alteration rates from moderate to strong. Figures 4.15 A show relict textures of magnetite with exsolution of ilmenite with trellis and sandwich-type lamellae replaced by pyrite.

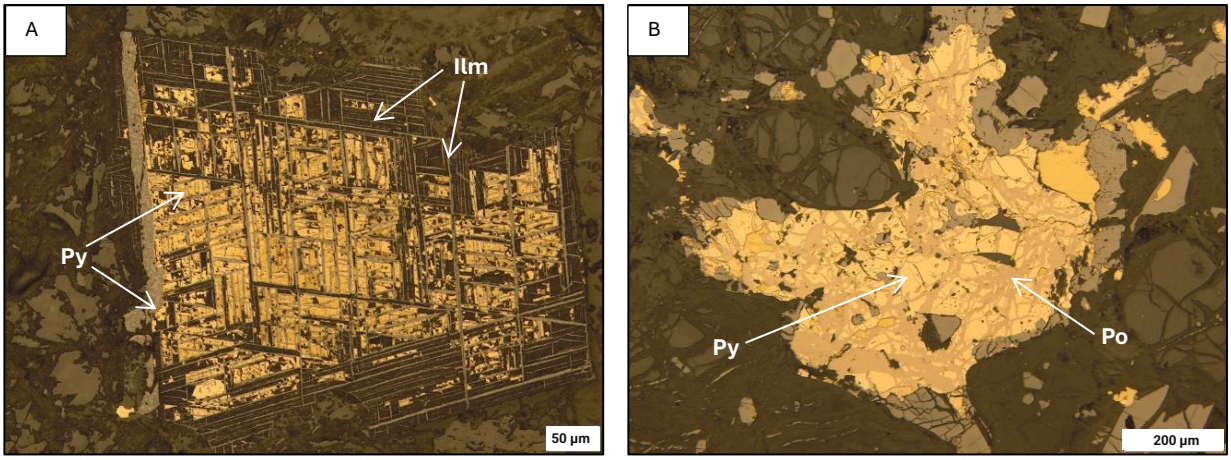

Figure 4.15: Photomicrographs in PPL. A: olivine gabbronorite with alteration of primary magnetite by pyrite (sample CAM-AC-22-35 from drillhole Bl11-431 at 386.6m depth). B: wehrlite with secondary pyrrhotite replacing secondary pyrite (sample CAM-AC-22-61 from drillhole Bl11-431 at 522.7m depth). Abbreviations: Po- pyrrhotite; Cpy- chalcopyrite; Py-pyrite; Ilm- ilmenite.

4.1.3.3 Secondary Oxides

Magnetite (from absent to 2% abundance) occurs altering primary sulfides such as chalcopyrite, pyrrhotite, and pentlandite (Fig. 4.16 A), with alteration from absent to 25%. Magnetite was also observed in olivine fractures with serpentine replacement (Fig. 4.16 B).

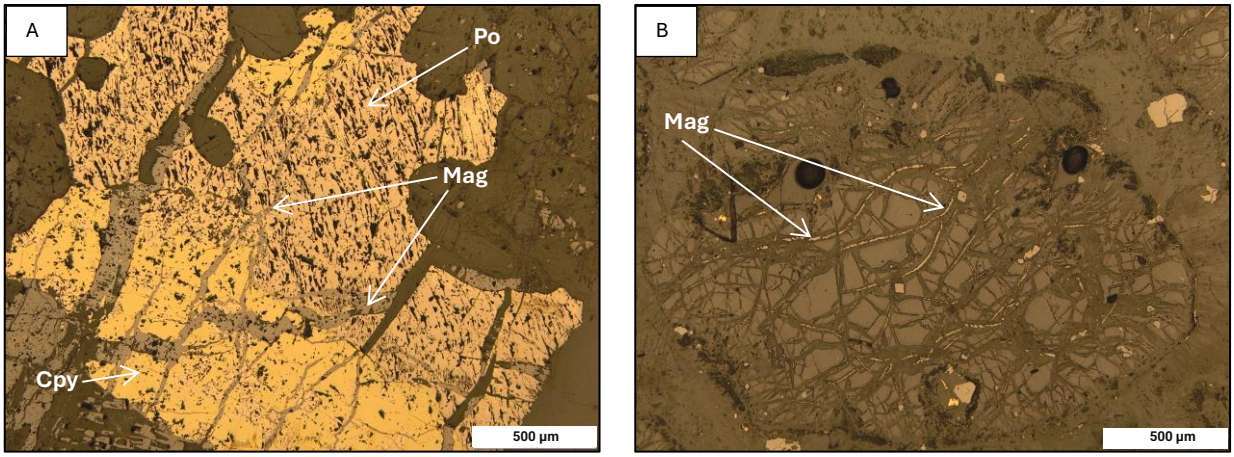

Figure 4.16: Photomicrographs in PPL. A: wehrlite with magnetite replacing primary sulfides (sample CAM-AC-22-02 from drillhole TBND086 at 29.9 m depth). B: lherzolite with magnetite precipitated in olivine fractures (sample CAM-AC-22-77 from drillhole CL22-036A at 192.4 m depth). Abbreviations: Po- pyrrhotite; Cpy- chalcopyrite; Mag- magnetite.

4.1.3.4 Carbonates

The carbonates were observed as veins (Fig. 4.17 A) crosscutting early alteration and as mineral aggregates (Fig. 4.17 B) pervasively altering magnesium-rich minerals such as actinolite-tremolite. The grain size varies from fine to coarse.

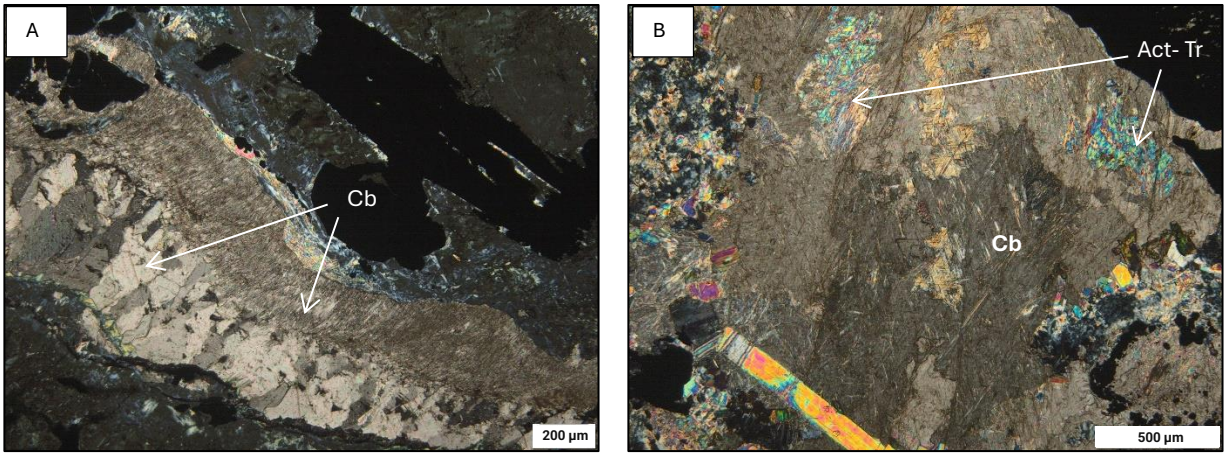

Figure 4.17: Photomicrographs in PPL. A: olivine gabbronorite with vein of carbonate crosscutting earlier alterations (sample CAM-AC-22-36 from drillhole Bl11-431 at 390.8m depth). B: wehrlite with carbonates overprinting earlier alterations (sample CAM-AC-22-41 from drillhole Bl11-431 at 412.62m depth). Abbreviations: Cb- carbonates; Tr-tremolite; Act- actinolite.

A total of 53 samples were collected for lithogeochemical analysis; 50 samples were taken from the four zones of the Current Intrusion, and three samples were taken from the country rock of the Quetico basin. The complete anhydrous major and trace element dataset for these samples is provided in Appendix B.

4.2.1 Major Elements

According to Le Maitre (1989), ultramafic rocks are differentiated from mafic rocks by SiO_2 contents < 45 wt%. The samples analyzed demonstrate that CaO, Na_2O, Al_2O_3, and K_2O show a positive correlation with SiO_2, whereas MgO and Fe_2O_3 show a negative correlation (Fig. 4.18). Eight of the 50 samples (one in the Current zone, two in the 437 SEA zone, and five in the Beaver-Cloud zone) plot as mafic/gabbroic rocks (>45% SiO_2); the rest of the samples plot as ultramafic rocks.

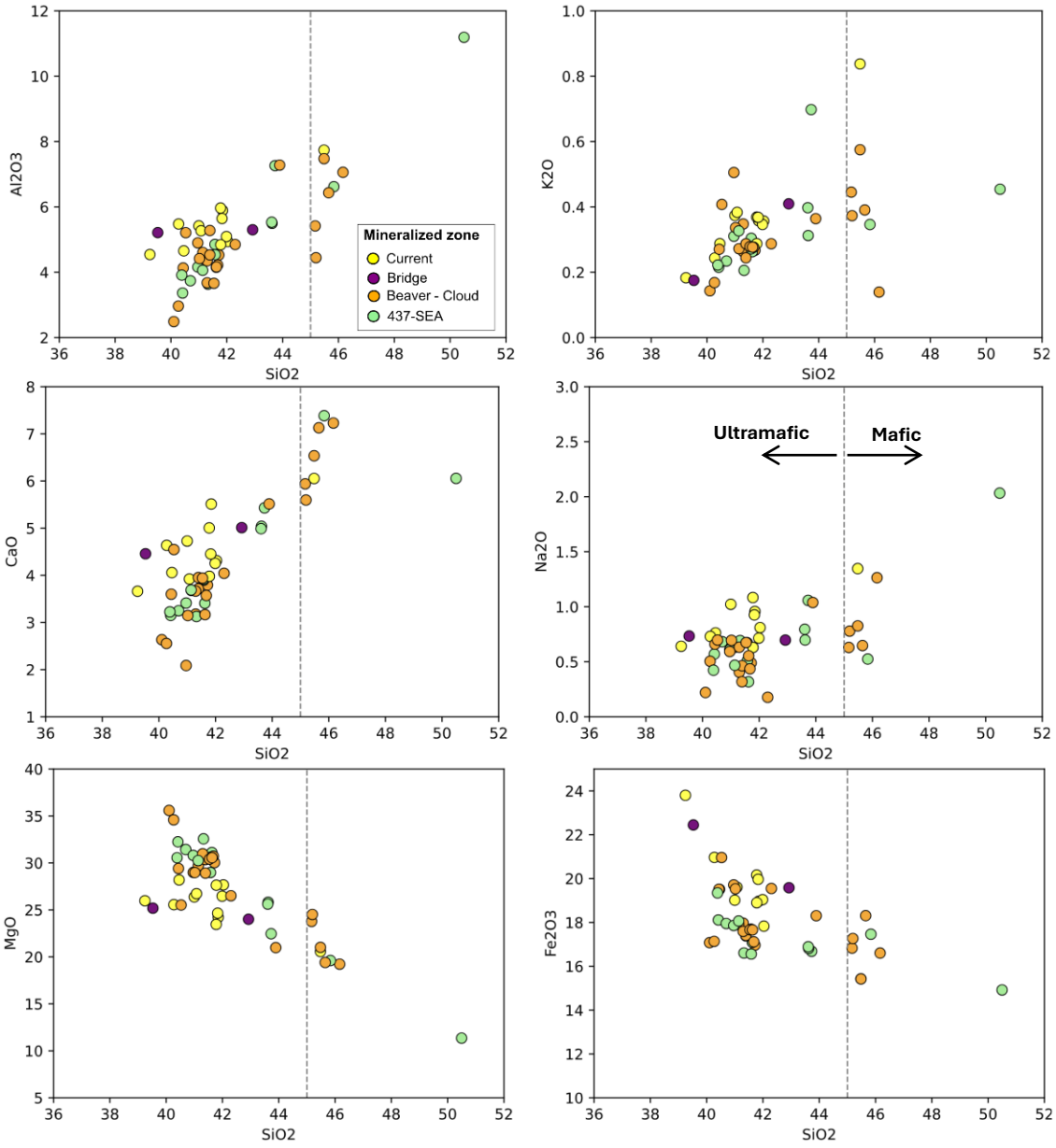

Figure 4.18: Binary diagrams of major elements (MgO, Fe_2O_3, CaO, Na_2O, $Al2O_3$, K_2O) versus SiO_2 in the four mineralized zones of the Current Intrusion. The dotted gray line represents the separation between mafic and ultramafic rocks according to Le Maitre (1989).

4.2.2 Trace Elements

Samples in the intrusion show values of Ta/Yb from 0.5 to 1. In contrast, the distribution of Th/Yb reflect values 0.5 to 0.8 (Fig. 4.19).

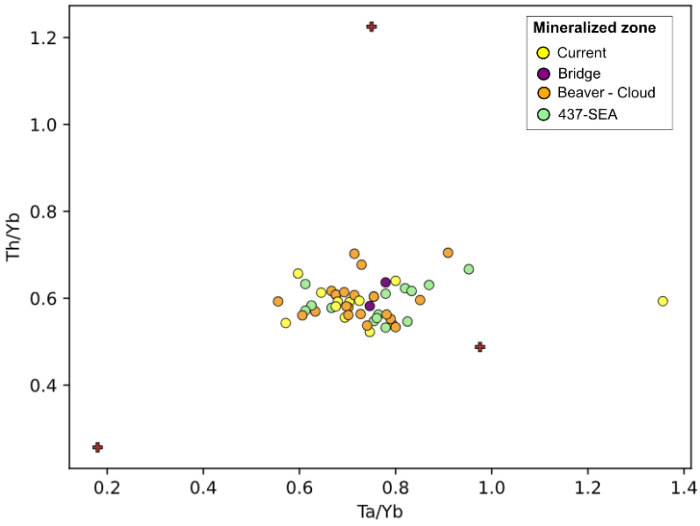

Figure 4.19: Th/Yb versus Ta/Yb in the four mineralized zones of the Intrusion

Primitive mantle normalized multi-element diagrams show that the Current Intrusion is light rare earth element (LREE) enriched with slightly elevated Nb, La, and Ce over Th (Fig. 4.20 A). The Quetico country rock has negative Nb and Ti anomalies and elevated concentrations of Th (Fig. 4.20 B).

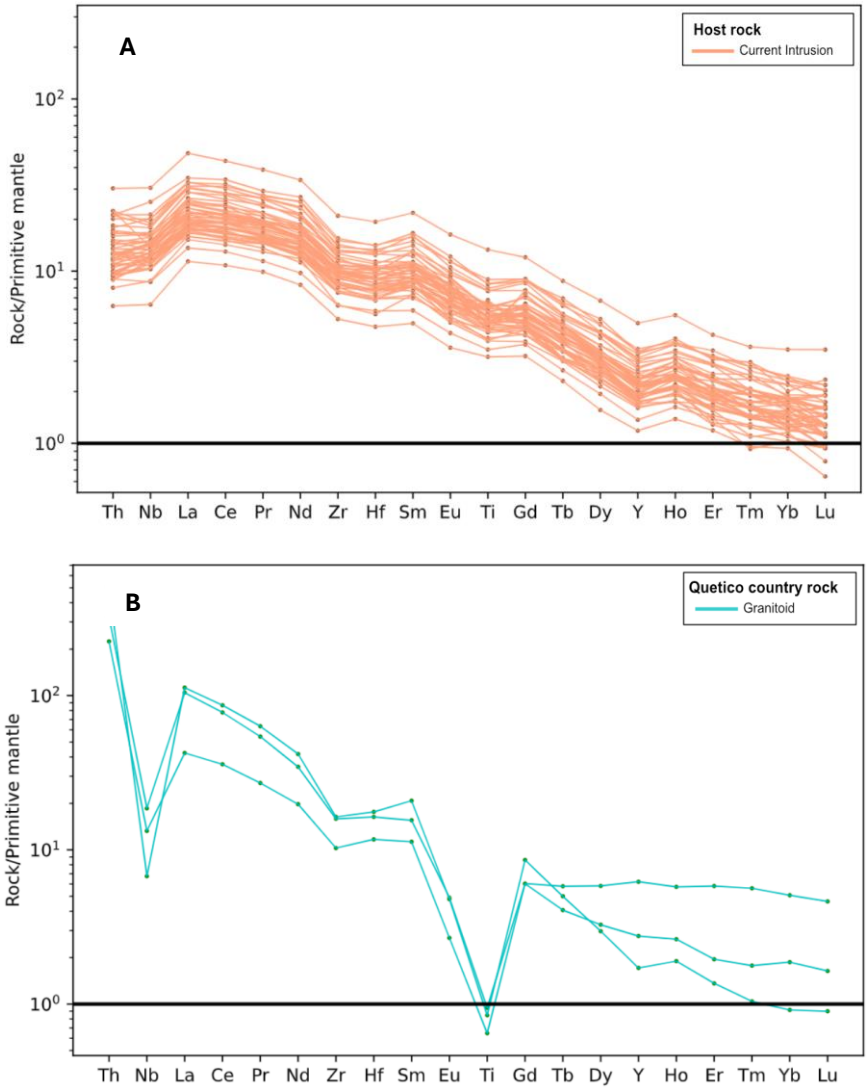

Figure 4.20: Primitive mantle-normalized spider diagram for; A: Current Intrusion and B: Quetico country rocks. Normalizing values from Sun & McDonough (1989).

The intrusive samples are characterized by La/Sm_n values from 1.8 to 2.6, Gd/Yb_n from 3 to 4.4 (Fig. 4.21), Th/Nb from 0.08 to 0.2, Th/La from 0.06 to 1.11, and Th/Ta from 0.4 to 1.6. The Quetico granitoid country rock is characterized by La/Sm_n values ranging from 3.7 to 6.8, Gd/Yb_n values ranging from 0.9 to 8.8, Th/Nb from 2 to 9, Th/La from 0.35 to 0.71, and Th/La from 13 to 60.

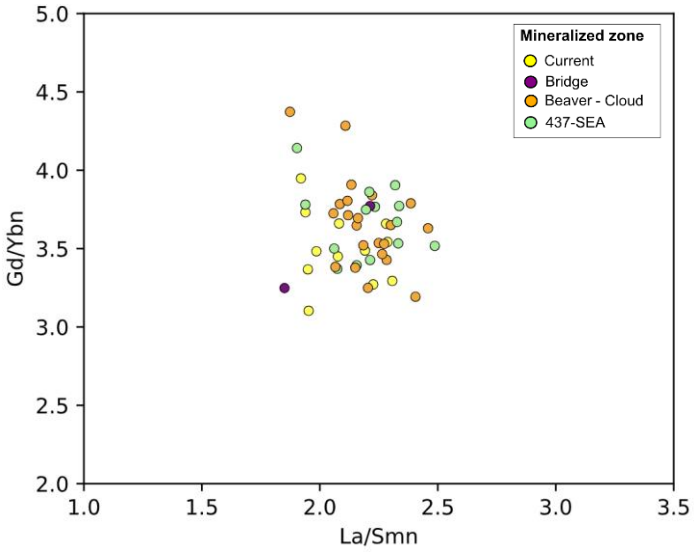

Figure 4.21: Chondrite-normalized, whole-rock REE ratio variation for the Current Intrusion. Normalizing values from Sun & McDonough (1989).

4.3 Stable Isotopes

4.3.1 Oxygen-Hydrogen Isotopes

The complete data set for the O-H isotope composition of 35 bulk rock samples is provided in Appendix E. Figure 4.22 illustrates the variation of $\delta^{18}O$ and $\delta^{2}H$ in the different mineralized zones in the Current Intrusion and the Quetico country rock. The data for the intrusion is characterized by values of $\delta^{18}O$ from 3.1 to 7.7‰ and values of $\delta^{2}H$ from -116 to -63‰ and overall show a positive trend. In contrast, the Quetico country rock shows $\delta^{18}O$ values between 9.5 and 10.2‰ and $\delta^{2}H$ values from -81 to -113‰.

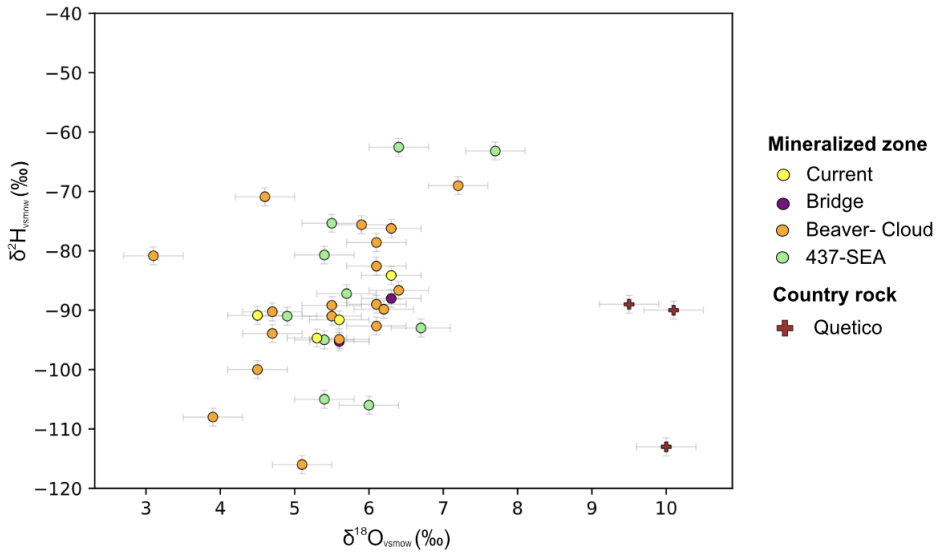

Figure 4.22: $\delta^{18}O$ and $\delta^{2}H$ values of bulk rock samples in the four mineralized zones of the Current Intrusion (Current, Bridge, Beaver-Cloud, and 437-SEA) and the surrounding country rock of the Quetico basin. The error for the $\delta^{18}O$ and $\delta^{2}H$ are 0.4 and 1.5‰, respectively.

4.4 Radiogenic Isotopes

4.4.1 Strontium-Neodymium Isotopes

Radiogenic isotopes of Sr and Nd for ten bulk rock samples is provided in Appendix D. Figure 4.23 illustrates the variation of ε_{Nd} and initial $^{87}Sr/^{86}Sr$ ratios (Sr_i), recalculated at 1106.6 Ma, for the different mineralized zones of the Current Intrusion. The rock suite analyzed have values of ε_{Nd} from -1.18 to -4.02, $^{147}Sm/^{144}Nd$ from 0.1200 to 0.1289, $^{143}Nd/^{144}Nd$ (initial) from 0.511003 to 0.511148, and $^{143}Nd/^{144}Nd$ (current) from 0.51190 to 0.51208. Additionally, it has values of Sr_i from 0.7021 to 0.7043, $^{87}Rb/^{86}Sr$ from 0.065 to 0.549, and $^{87}Sr/^{86}Sr$ (current) from 0.703589 to 0.713084.

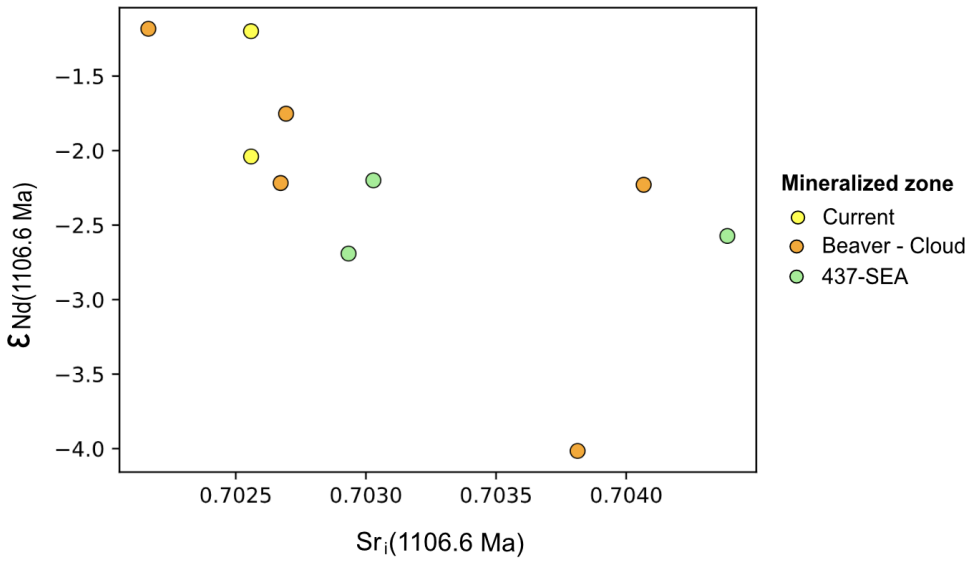

Figure 4.23: Binary diagrams of ε_{Nd} (1106.6 Ma) versus Sr_i (1106.6 Ma) for samples of three mineralized zones of the Current Intrusion (Current, Beaver-Cloud, and 437-SEA).

4.5 Mineral Chemistry

4.5.1 Major Element Chemistry

A population of pyroxenes, serpentine, and chlorite groups minerals were identified by SEM-EDS. Calculation of the serpentine and chlorite structural formula based on 14 and 28 oxygens, respectively (Calculated assuming full site occupancy; method Reference: Deer et al., 1992). The complete data set is provided in Appendix C.

The antigorite (n=5) and the lizardite-chrysotile (n=10) show a negative trend of SiO_2 respect MgO and H_2O (Fig. 4.24 A, B). The lizardite-chrysotile is characterized by higher percentages of MgO wt.% (>40.5 wt.%) and H_2O (>13 wt.%) and lower values of SiO_2 (<43 wt.%) compared to antigorite.

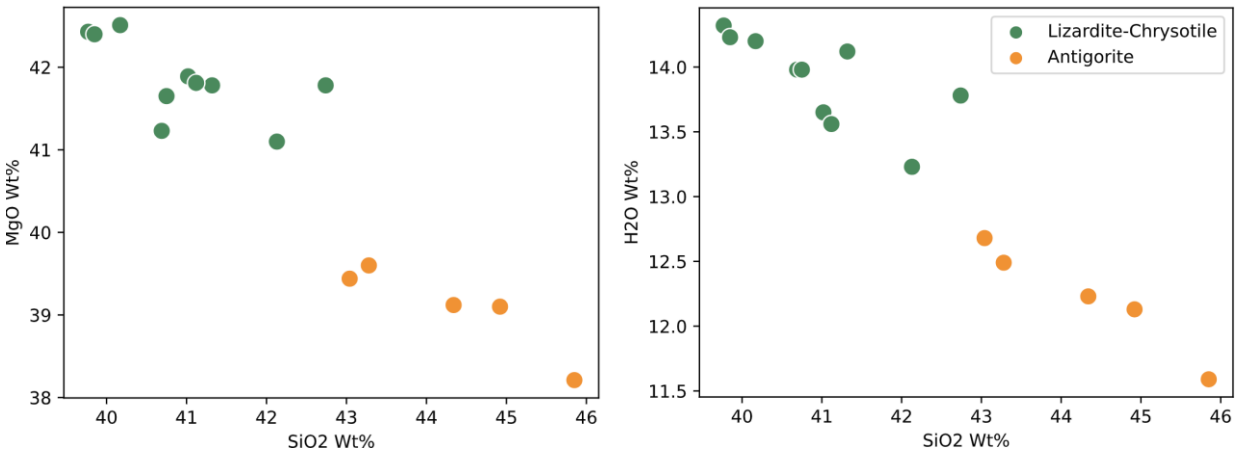

Figure 4.24: Binary diagrams plots of the weight percentages of: A: MgO versus SiO2, B: H_2O versus SiO_2, in two populations of the serpentine group minerals, antigorite and lizardite-chrysotile.

Eleven chlorite samples were characterized as clinochlore and four as chamosite. The clinochlore is rich in magnesium (the analysis was taken from plagioclases and pyroxenes replaced by chlorite), whereas the chamosite is rich in iron (the analysis was taken from magnetite replaced by chlorite). A population of clays from the smectite group was identified in the chlorite analyzed, classified as saponite (n=18), which is a clay closely related to chlorite in hydrothermal systems (Schiffman & Staudigel, 1995; Robinson & De Zamora, 1999; Fig. 4.25).

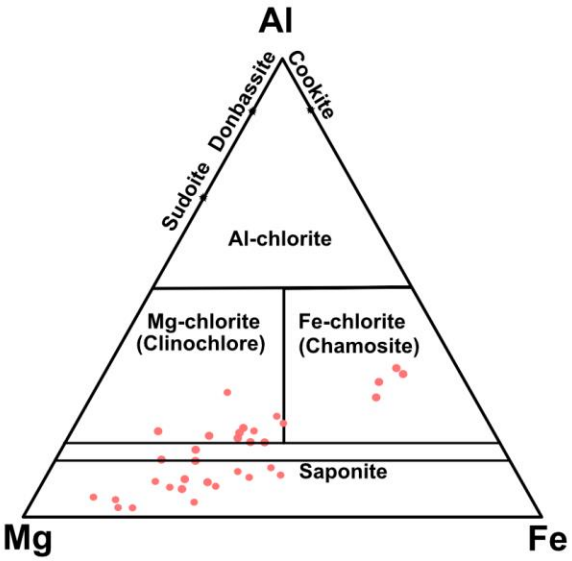

Figure 4.25: Ternary diagram of the atomic weight portions of Al, Mg, and Fe in the chlorite group minerals. The red dots represent the 33 chlorites analyzed.

Four pyroxene samples were characterized as augite, clinopyroxene rich in Ca and low Fe, and two as enstatite, orthopyroxene rich in Mg and low Fe (Fig. 4.26).

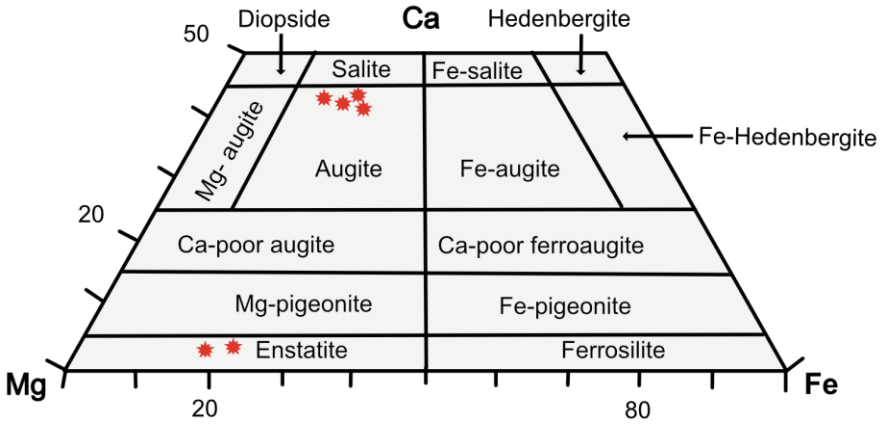

Figure 4.26: Ternary diagram of the atomic weight portions of Ca, Mg, and Fe in the pyroxene group minerals. The red stars represent the six pyroxenes analyzed.

5. DISCUSSION

5.1 Paragenetic Sequence

The mafic-ultramafic Current Intrusion comprises an assemblage of primary magmatic phases overprinted by alteration(s) event(s). A mineral paragenesis of the Current Intrusion has been developed through petrographic observations to establish mineral associations and crosscutting relationships, coupled with the integration of geochemical data (Table 5.1).

Table 5.1: Paragenetic sequence of crystallization for the Current Intrusion

Mineral	Magmatic phase	Hydrothermal phase
Silicates		
Olivine	----------	
Pyroxene	----------	
Plagioclase	----------	
Biotite	?---------- ?	
Antigorite		----------
Lizardite-Chrysotile		----------
Epidote		----------
Clinochlore		----------
Chamosite		----------
Sericite		----------?
Actinolite-tremolite		----------?
Talc		----------
Carbonates		----------
Sulfides		
Pyrrhotite	----------	------?
Pentlandite	----------	
Chalcopyrite	----------	
Cubanite	----------	
Pyrite		----------?
Oxides		
Chromite	-----	
Magnetite	----------	----------?
Ilmenite	----------	

5.1.1 Magmatic Phases

Based on petrographic observations, samples for the Current Intrusion comprise a peridotite and a gabbro unit consisting of fine-grained wehrlite and lherzolite and an olivine gabbronorite ± troctolite. Petrographic analysis suggests early formation of fine- to medium-grained olivine phenocrysts enclosing very fine-grained chromite crystals, suggesting that the chromite crystallized prior to olivine (Fig. 5.1). Subsequently, as the temperature in the magmatic system decreased, oikocrysts of pyroxene enclosed some of the olivine crystals, followed by the crystallization of medium-grained subhedral plagioclase filling the remaining interstices.

The paragenesis of biotite was difficult to determine based on textural-petrographic observations given the high degrees of chlorite alteration, mainly located on boundaries; nevertheless, in less altered phases, the biotite, seems secondary due to its fine-grained and anhedral features. Kushiro (1979) discussed the complexity of forming primary biotite from tholeiitic magma given the low content of volatiles in residual mantle liquids, which are typically insufficient for biotite formation. The Basaltic Volcanism Study Project (1981) demonstrated that H_2O content in some Keweenawan lavas from the North Shore Volcanic Group and rift-related continental flood basalts range from 2 to 4 wt.%, which could potentially provide sufficient water content (~3.7 wt.%; Snelling, 1957) for biotite crystallization, however, there is no direct evidence of the primary water content in the Current Intrusion magma.

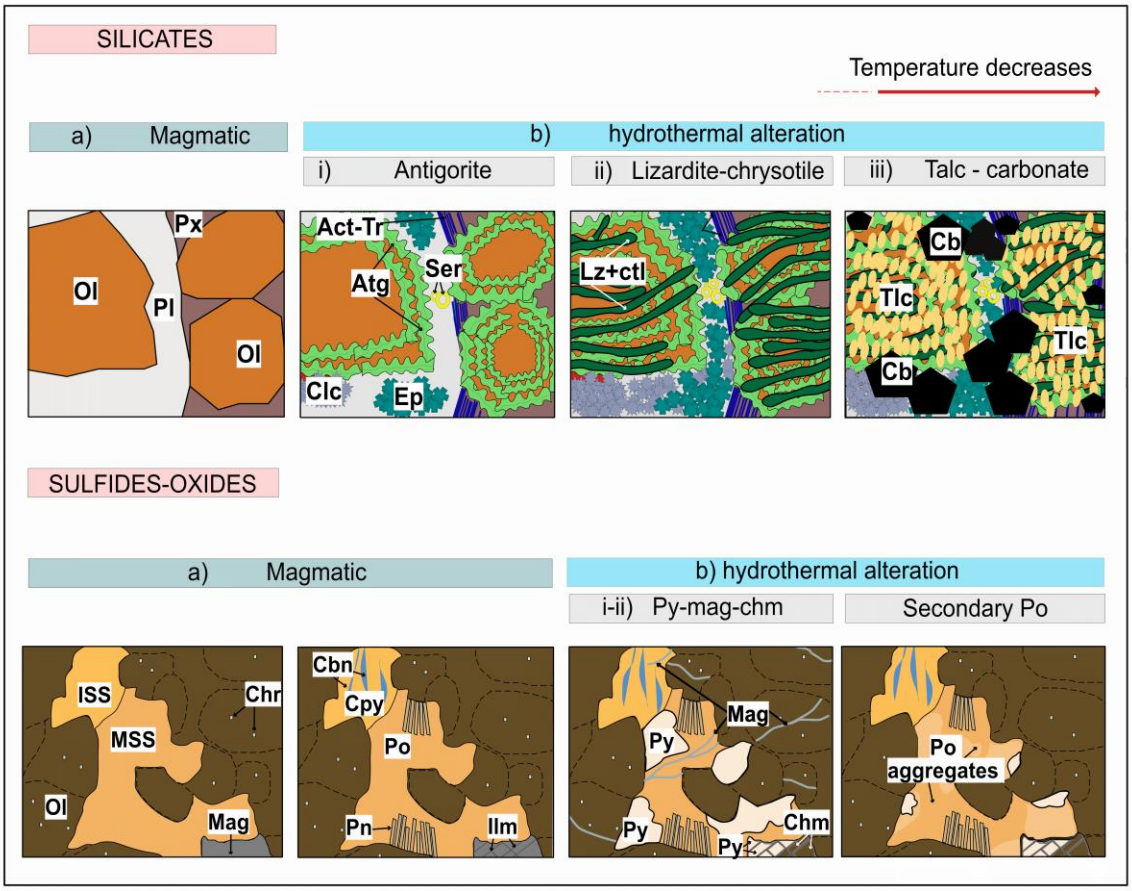

Figure 5.1: Schematic sequence of the paragenetic events of the Current Intrusion from the magmatic to the hydrothermal phase followed by localized anhydrous phases that facilitated the crystallization of secondary pyrrhotite after pyrite. Mineral Abbreviations: Ol- olivine; Px- pyroxene; Pl- plagioclase; Atg- antigorite; Lz- lizardite; Ctl- chrysotile; Tlc- talc; Tr- tremolite; Act- actinolite; Clc-clinochlore; Ser- sericite; Ep- epidote; Cb- carbonates; MSS- monosulfide solid solution; ISS- intermediate solid solution; Po- pyrrhotite; Cpy- chalcopyrite; Pn- pentlandite; Mag- magnetite; Chr- chromite; Cbn- cubanite, Py- pyrite; Chm- chamosite.

Fine-grained magnetite and sulfides were observed interstitial to the mafic silicates, suggesting crystallization after the olivine and pyroxenes. The magnetite and ilmenite exsolution (with trellis and sandwich-type lamellae) mostly occur next to apparently coeval monosulfide solid solution (MSS), and intermediate solid solution (ISS) recrystallized as pyrrhotite, pentlandite, and chalcopyrite (Fig. 5.1). This is consistent with Naldrett (1969) and Fonseca et al. (2008)

observations who proposed that magnetite undergoes a two-stage crystallization process from the sulfide liquid: initially, at high temperatures, magnetite starts crystallizing at the same time as the MSS. As the temperature decreases, magnetite continues to crystallize, as does ISS (Craig & Kullerud, 1969; Fleet & Pan, 1994). During the cooling process, at subsolidus temperatures (<600°C), ilmenite exsolves from titanomagnetite (Dare et al., 2012), and pyrrhotite and pentlandite recrystallize from the MSS and chalcopyrite from the ISS (Barnes et al., 2001a,b; Holwell & McDonald, 2010; Dare et al., 2011).

5.1.2 Hydrothermal Phase

The degree of pre-existing primary mineral replacement by secondary minerals was assessed using alteration intensity, where the increase of secondary minerals over primary minerals was quantified: weak alteration (0-33.3%), moderate alteration (33.4-66.6%), and strong alteration (66.7-100%).

Three distinct assemblages (domains) of secondary minerals were identified within the intrusion (Figs. 5.1, 5.2). In Domain A, the alteration of olivine led to the formation, mostly in boundaries and fractures, of magnetite, antigorite ± actinolite-tremolite, with alteration intensities ranging from weak to strong; also, the alteration of pyroxenes by actinolite-tremolite, antigorite, and clinochlore and plagioclase by epidote, sericite, and clinochlore, with alteration intensities varying from weak to moderate. In addition, pyrite after pyrrhotite, secondary magnetite after chalcopyrite, pyrrhotite, and pentlandite and chamosite-pyrite after magmatic magnetite, as well as secondary pyrrhotite (pyrrhotite aggregates) after the secondary pyrite. In Domain B, antigorite and olivine were replaced by lizardite-chrysotile with up to 100% alteration intensity, accompanied by an increase of modal abundance of epidote, sericite, and clinochlore with alteration intensities ranging

from moderate to strong, along with pyrite and magnetite after pyrrhotite, chalcopyrite, and pentlandite compared to Domain A. Domain C is characterized by talc-carbonate minerals replacing up to 100% of secondary minerals from domains A and B.

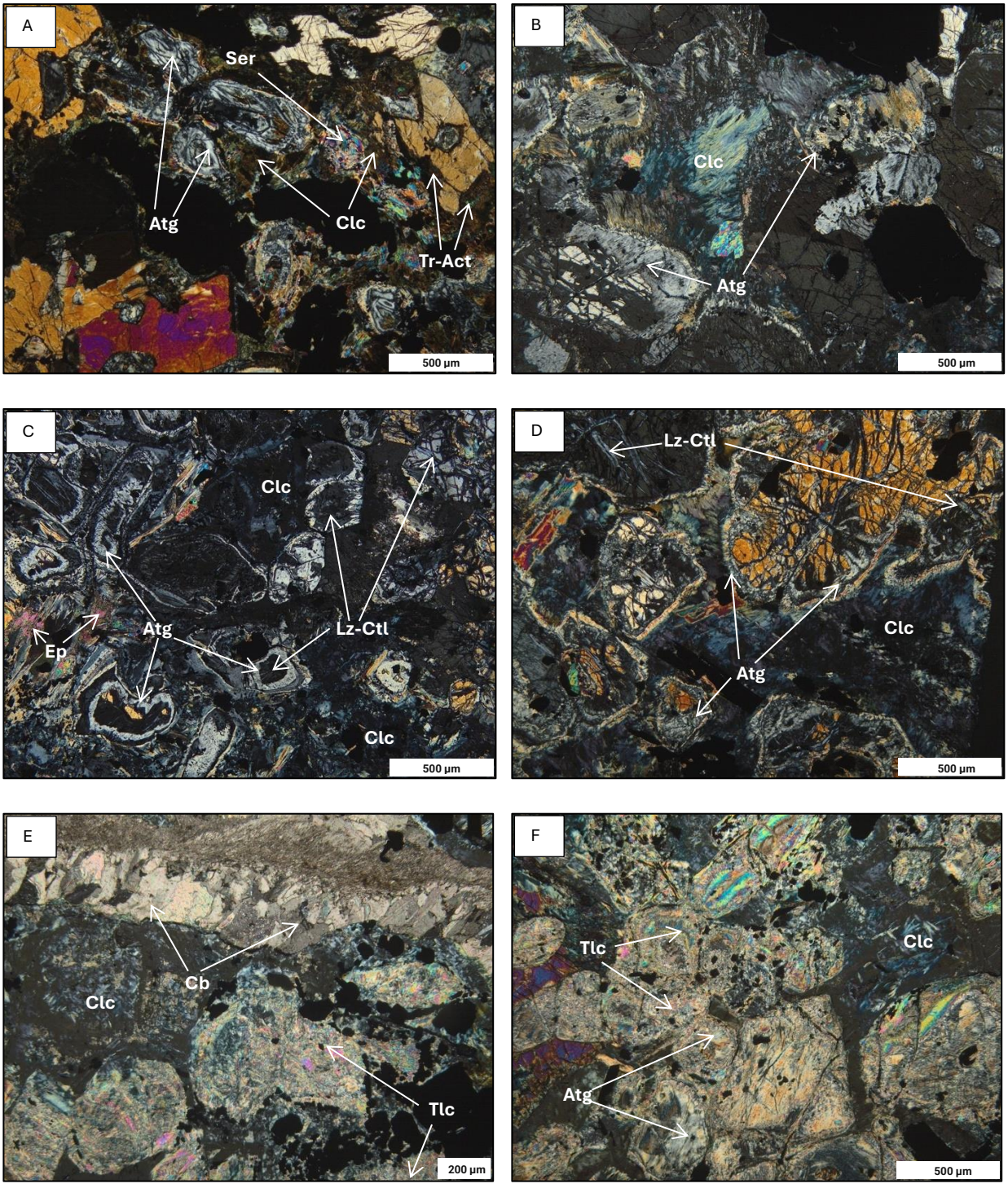

Figure 5.2: Photomicrographs in XPL. A: Domain A (sample CAM-AC-22-83 from drillhole CL22-036A at 211.83 m depth). B: Domain A (sample CAM-AC-22-37 from drillhole Bl11-431 at 400.1 m depth). C: Domain B (sample CAM-AC-22-71 from drillhole CL22-036A at 162.9 m depth). D: Domain B (sample CAM-AC-22-77 from drillhole CL22-036A at 192.3 m depth). E: Domain C (sample CAM-AC-22-36 from drillhole Bl11-431 at 390.8 m depth). F: Domain C (sample CAM-AC-22-36 from drillhole Bl11-431 at 390.8 m depth). Abbreviations: Lz- lizardite; Atg- antigorite; Ctl- chrysotile; Tlc- talc; Tr- tremolite; Act- actinolite; Ep- epidote; Cb- carbonates; Clc-clinochlore; Ser- sericite.

The primary magmatic pyrrhotite was initially replaced by pyrite, which was subsequently replaced by secondary pyrrhotite (Domain A; Fig. 5.3). In the intrusion, such replacement was observed in a few samples mostly at depth in the Current and Beaver-Cloud zones and in the shallowest areas of the 437-SEA zone. This is consistent with the work of Brzozowski et al. (2023) who proposed that thermal metamorphism caused by late crystallization of the deepest zones of the intrusion, would have affected the early-crystallized zones that underwent hydrothermal processes, resulting in secondary pyrrhotite replacing pyrite.

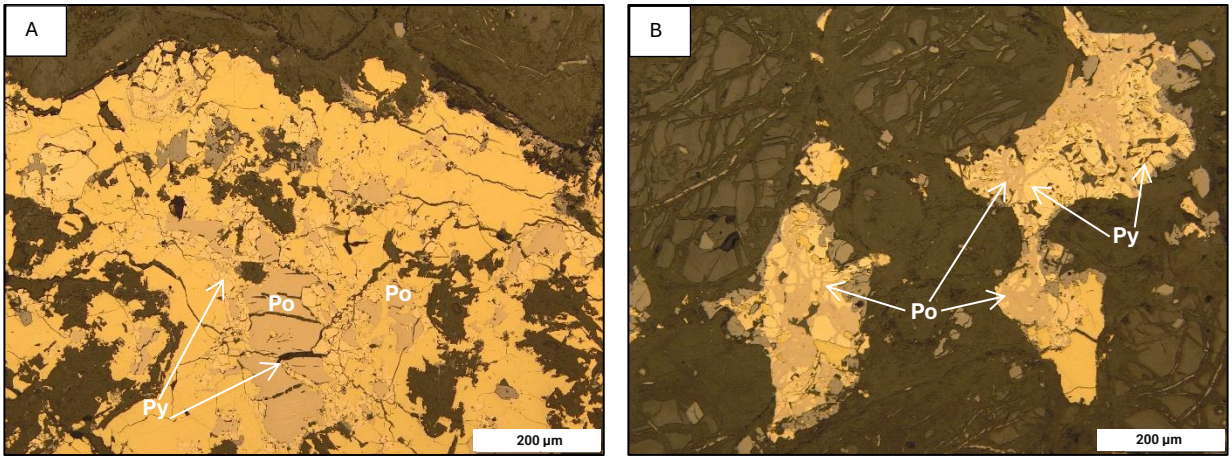

Figure 5.3: Photomicrographs in PPL. A: wehrlite with secondary pyrite replacing primary pyrrhotite (sample CAM-AC-22-64 from drillhole Bl11-431 at 535.15 m depth). B: wehrlite with secondary pyrrhotite replacing secondary pyrite (sample CAM-AC-22-61 from drillhole Bl11-431 at 522.70 m depth). Abbreviations: Po- pyrrhotite; Py- pyrite.

The mineralogy of the different alteration domains within the Current Intrusion suggests the involvement of fluids at varying temperatures (>300°C to <50°C; Fig. 5.1). Domain A is characterized by a secondary mineralogy that, likely crystallized at temperatures exceeding 300°C based on work by Arnason et al. (1993), Evans (2004), Lagat (2009), and Welch and Marshall (2015) who investigated crystallizing temperatures of similar assemblages. Conversely, lizardite-chrysotile of Domain B has been interpreted to crystallized from fluids below 300°C according to research conducted on mafic rocks by Keith et al. (1968), Evans (2004), and Li et al. (2019). Subsequently, alteration in Domain C was likely triggered by CO_2-bearing fluids, as reported by Schoklitsch (1935) in similarly altered rocks in Austria. The mineralogy in Domain C is thought to have crystallized at temperatures below 50°C based on work by Barnes et al. (1973) and Kelemen and Matter (2008), which determined the crystallization temperatures of this secondary assemblage in mafic rocks. The secondary mineralogy of domains A and B is consistent with an acidic pH, given the work of O'Hanley (1996) and Fulignati (2020), who determined the

physicochemical conditions required for these secondary assemblages to crystallize. In contrast, according to Chaliulina (2019), in similar mineralogical studies, Domain C assemblages would have crystallized under basic pH conditions.

The replacement of magmatic pyrrhotite, chalcopyrite, pentlandite, and magnetite by secondary pyrite, secondary magnetite, and chamosite due to the interaction of fluids with the rock can result in significant mobilization of key elements. Holwell et al. (2017) showed this in hydrothermally altered rocks of the Bushveld Complex, with losses of Fe-S-Ni-Cu and substantial reduction in mineral volume (estimated at 40-90% reduction). Most of the samples analyzed in the Current Intrusion exhibit mobilization of elements and significant volume reduction of primary minerals in the alteration process, with, for example chalcopyrite replaced by secondary magnetite (Fig. 5.4A), chalcopyrite replaced by pyrite and secondary magnetite (Fig. 5.4B), primary magnetite with relict texture replaced by pyrite and chamosite, leaving behind exsolutions of ilmenite with trellis and sandwich-type lamellae (Fig. 5.4C-D). Brzozowski et al. (2023) proposed that in the Current Intrusion, the iridium-group PGE (Ir, Os, and Ru), Cu, and Pd are retained in the alteration minerals; whereas Ni, As, and Co were enriched, and Ag was depleted during the hydrothermal processes.

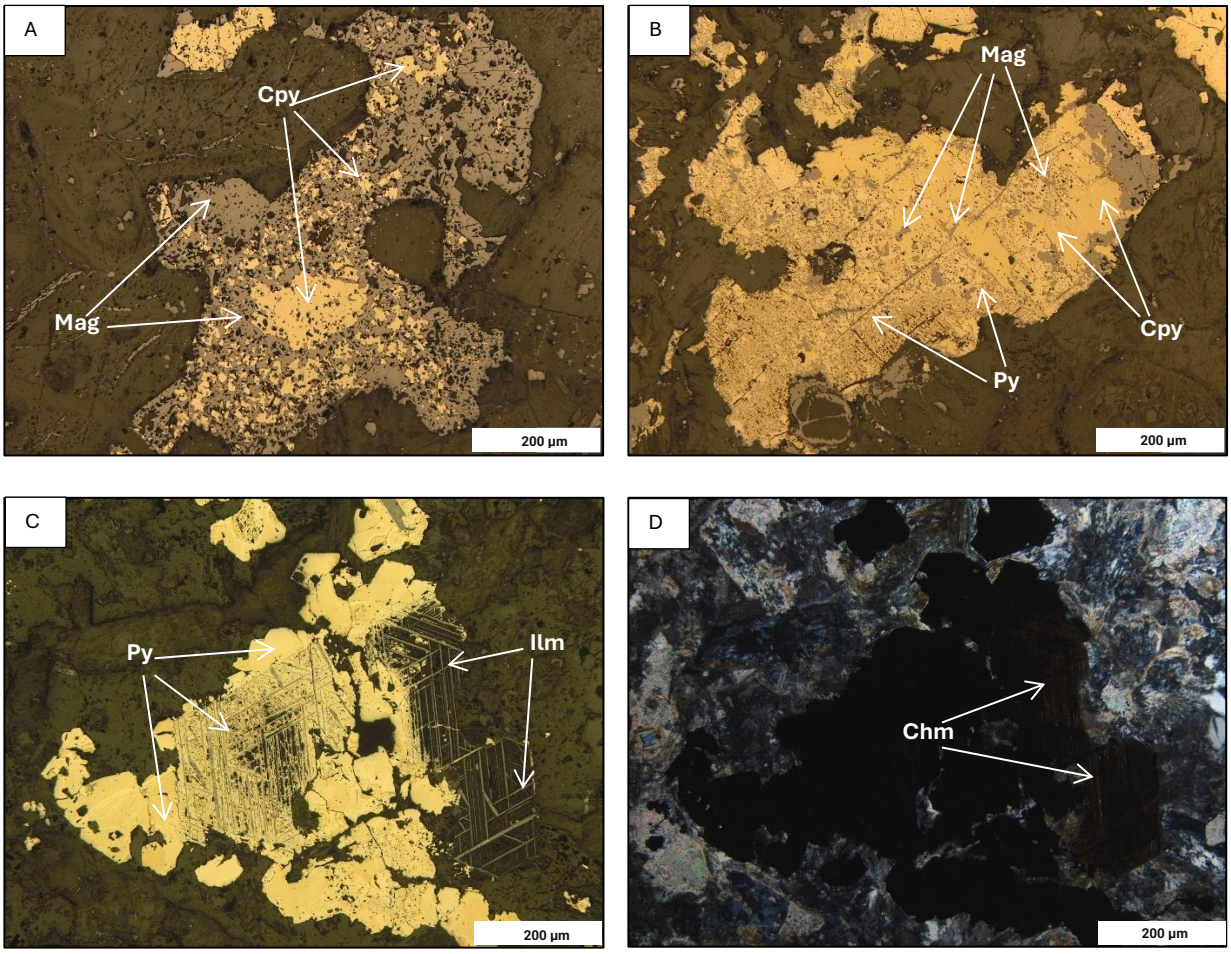

Figure 5.4: Photomicrographs in PPL and XPL. A: lherzolite with secondary magnetite replacing primary chalcopyrite (sample CAM-AC-22-15 from drillhole BL08-39 at 146.13 m depth). B: wehrlite with secondary pyrite and magnetite replacing chalcopyrite (sample CAM-AC-22-33 from drillhole BL08-39 at 220.11 m depth). C: olivine gabbronorite with secondary pyrite replacing primary magnetite (sample CAM-AC-22-35 from drillhole Bl11-431 at 386.6 m depth). D: olivine gabbronorite with chamosite replacing primary magnetite (sample CAM-AC-22-35 from drillhole Bl11-431 at 386.6 m depth) Abbreviations: Cpy- chalcopyrite; Mag- magnetite; Py- pyrite; Chm- chamosite.

5.2 Sources of Contamination

Certain Ni-Cu-PGE deposits have been attributed to upwelling plumes that ascend through the mantle and then undergo lateral movement along the base of the SCLM (Begg et al., 2010). Along

active extension structures, the mantle melts find pathways within the crust (Begg et al., 2010) where the rising magmas reach sulfur saturation (Li & Naldrett, 1993; Li et al., 2002; Ripley et al., 2003; Holwell & McDonald, 2010) through two primary processes (Robertson et al., 2015). Firstly, via thermal aureoles, where the transfer of mass from the wall rock to the magma occurs through the thermal decomposition of sulfide minerals present in the wall rock (this can be induced by the diffusion of heat emanating from the magma) transported through fractures and pore spaces to the magma chamber. Secondly, mass transfer that takes place through the assimilation, melting, and/or dissolution of xenoliths from the country rock. It has been suggested that the magmas related to the MRS were contaminated by either sedimentary rocks, Archean basement rocks, or SCLM during transportation from the mantle into the crust, based on the Th/Nb ratios, radiogenic ε_{Nd}, Sr_i, and γOs_i values, MgO and SiO_2 wt% (Hollings et al., 2007a,b; Cundari, 2012; Trevisan, 2014; Brzozowski et al., 2022). The source of the Current Intrusion parental magma and the effect of potential contamination can be investigated using whole-rock trace elements and radiogenic (ε_{Nd}, Sr_i) and stable (O) isotope signatures.

5.2.1 Whole-Rock Geochemistry

5.2.1.1 Primary Signature

Samples from the Current Intrusion plot in the field of mantle array in the diagram of Th/Yb versus Ta/Yb reflecting a chemical affinity with melts derived from an OIB-type mantle source (Fig. 5.5), with insignificant crustal contamination.

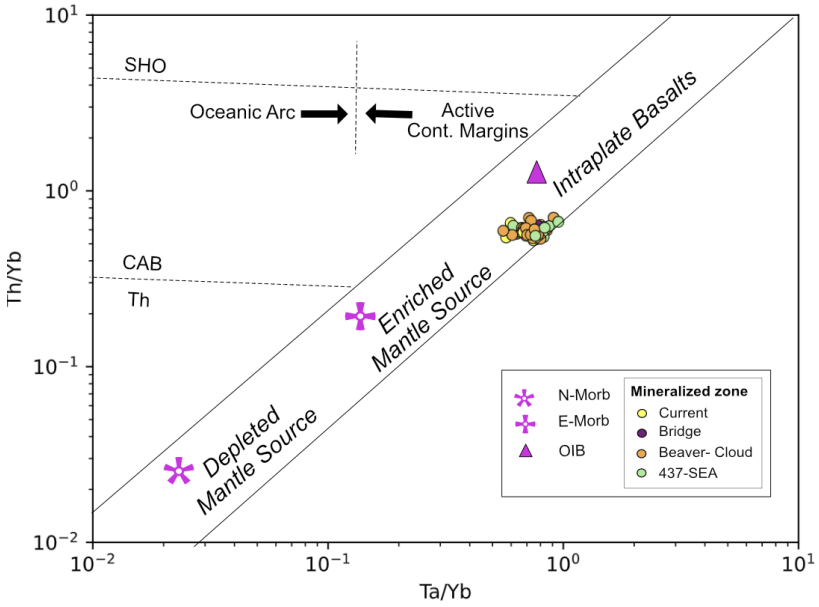

Figure 5.5: Ta/Yb-Th/Yb distribution diagram (Pearce, 1983) for the four mineralized zones of the Current Intrusion. N-MORB, E-MORB, and OIB values are Sun & McDonough (1989).

The intrusion displays a well-defined primitive mantle-normalized pattern (similar to ocean island basalt, OIB; Sun & McDonough, 1989) characterized by LREE enrichment and small positive Nb, La, and Ce anomalies over Th (Fig. 5.6), indicating the absence of crustal contamination, which would have produced negative Nb and Ta anomalies (Hofmann, 1997; Hollings et al., 2007a,b). The mineralized Escape Intrusion, which is also part of the MRS magmatism associated with the upwelling Keweenaw plume, shares a similar uncontaminated pattern (Caglioti, 2023). In contrast, the Quetico country rocks show a greater degree of LREE enrichment, along with enrichment in Th and La (Fig. 5.6). Therefore, direct melting or assimilation of Quetico country rock is not likely to have been a significant source of contamination in the intrusion.

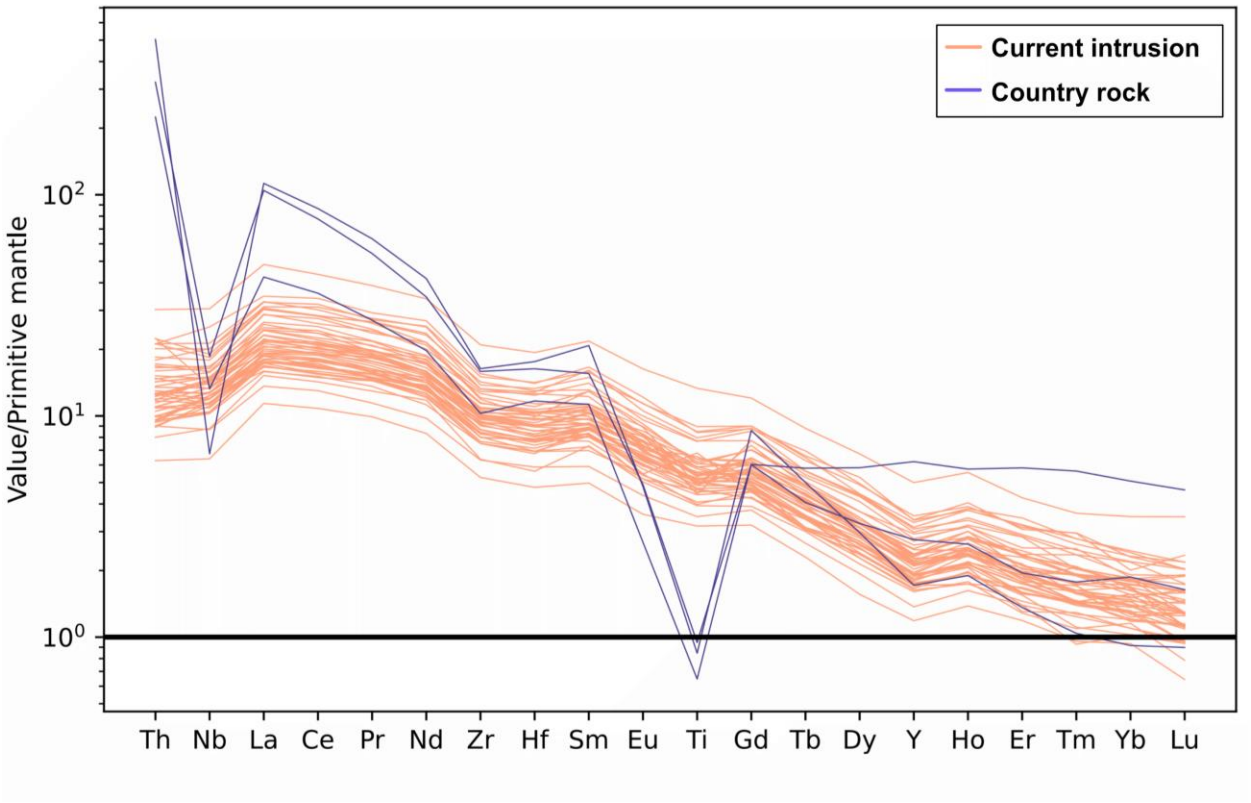

Figure 5.6: Primitive mantle-normalized spider diagram for Current Intrusion and Quetico country rocks. Normalizing values from Sun & McDonough (1989).

The La/Sm_n values of the Current Intrusion samples (1.8 to 2.6; Fig. 5.7), are consistent with studies by Nicholson and Shirey (1990) who propose a parental basaltic magma derived from an enriched mantle plume with a chondrite-normalized La/Sm_n of 2 to 3. The elevated La/Sm_n of the magma in the Current Intrusion resembling other mineralized and unmineralized intrusions that are part of the MRS, including Escape (1.4 to 2.3), Seagull (0.78 to 5.21), Lone Island intrusion (1.4 to 3.3), and those in the Nipigon Embayment (1 to 4; Fig. 5.7; Heggie, 2005; Hollings et al., 2007b; Caglioti, 2023; Yahia, 2023). Brzozowski et al. (2022) proposed that certain MRS magmas may have originated from a depleted source within the Keweenawan plume, based on the presence of radiogenic γOs_i values, a LREE-depleted signature compared to OIB, and high degrees of partial melting akin to primitive mantle compositions as seen in the Nipigon sills. The Gd/Yb_n values in

the Nipigon Embayment are lower (1 to 3; Fig. 5.7) compared to the Seagull intrusion (2.09 to 3.71) and the Current (3 to 4.4), Lone Island (1.5 to 4.5) and Escape (3 to 5) intrusions. This suggests the parental magmas originated from distinct mantle sources and magmas generated through varying degrees of partial melting, as shown in studies by Heggie (2005), Hollings et al. (2007b), Caglioti (2023), and Yahia (2023). For example, Hollings et al. (2007a) proposed that the Nipigon sills likely crystallized from a melt derived by high degrees of partial melting at relatively shallow depths in the spinel stability zone. In contrast, the Current Intrusion values would suggest a lower degree of partial melting at greater depths in the garnet stability zone.

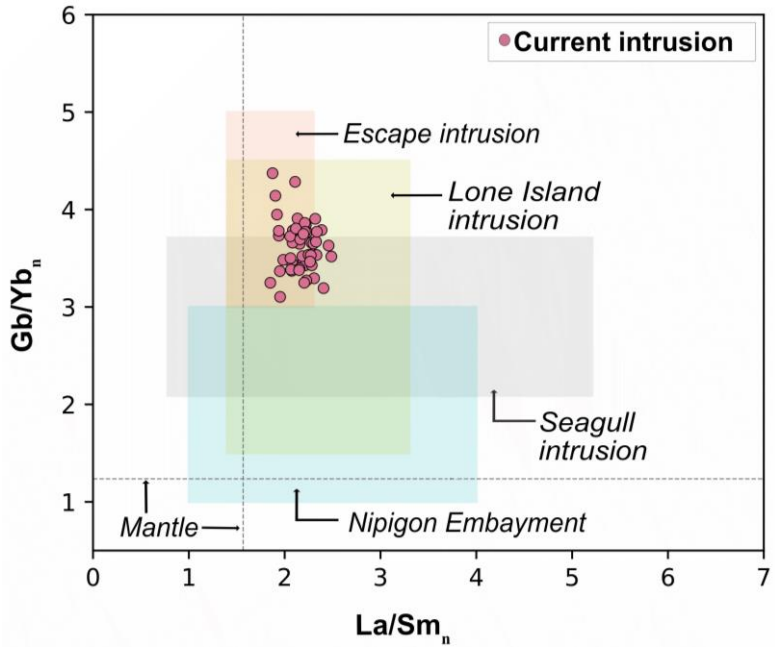

Figure 5.7: Chondrite-normalized, whole-rock REE ratio variation for Current Intrusion. Nipigon Embayment, Escape, Lone Island, and Seagull Intrusion values were taken from Heggie (2005), Hollings et al. (2007b), Caglioti (2023), and Yahia (2023). Mantle values and normalizing values from Sun & McDonough (1989).

The absence of evidence for continental crust contamination in the samples requires alternative models for sulfide saturation beyond country rock interaction by melting of xenolith and/or wall

rock. Robertson et al. (2015) proposed the thermal aureole model, which requires the thermal breakdown (devolatilization, dissolution, and direct melting) of sulfide minerals within the surrounding country rock, with subsequent transfer to the magma body. This model presents an additional alternative through which sulfide saturation could be achieved, which could be the case for the Current Intrusion. But Robertson et al. (2015) indicate that additional studies are required to support this model, including studies of the sulfide assemblages in the surrounding country rock, as well as experimental studies to reproduce the processes of dissolution and melting of sulfide minerals within the country rock and its transfer to the magma body.

5.2.2 Radiogenic Isotopes

The Sr_i values of the majority of the samples (0.7021 to 0.7043) are slightly lower than typical values of the mantle source at 1100 Ma, which has a composition of 0.703 to 0.705 (Hergt et al., 1989; Nicholson & Shirey, 1990). Similarly, the ε_{Nd} values of the intrusion (-1.18 to -4.02; Fig. 5.8) are lower than both enriched mantle (close to 0) and depleted mantle (around +6), as documented by Nicholson and Shirey (1990) and Shirey et al. (1994), and consistent with previous work on the Nipigon Sills, Seagull intrusion, and Coubran volcanics (Heggie, 2005; Hollings et al., 2007a; Cundari, 2012). Potential sources of contamination or contribution include: i) the Quetico Basin, with reported Sr_i compositions ranging from 0.701 to 0.717 and ε_{Nd} values of -16 to -24 according to Henry et al. (1998) and Pan et al. (1999); and ii) enriched SCLM with ε_{Nd} values of -9 (Shirey, 1997). Nonetheless, despite the lack of Nb, La, Ta anomalies that indicate crustal contamination in the Current Intrusion, an enriched SCLM is more probable, as Brzozowski et al. (2022) proposed.

An enriched SCLM beneath the MRS (Shirey, 1997) was presumably built by metasomatism through southward-dipping subduction (Shirey et al., 1994), possibly during the 1220 Ma Shawinigan orogeny (Swanson-Hysell et al., 2019). Good and Lightfoot (2019), Good et al. (2021), and Rooney et al. (2022) proposed an interaction between the parental magma and the metasomatized (enriched) SCLM given the variation in large ion lithophile elements (LILE), LREE, and radiogenic isotopes within the Coldwell Complex. Brzozowski et al. (2022) provided additional evidence supporting this model, proposing that the slightly negative ε_{Nd} values of MRS-related basalts may indicate that plume-derived magmas interacted with an enriched SCLM, as in the case of Eva Kitto, Seagull, and Thunder intrusions. Collectively, these arguments point towards an enriched SCLM contributing to the slightly negative ε_{Nd} signature of the Current Intrusion at 1106.6 Ma relative to enriched and depleted plume sources (Fig. 5.8).

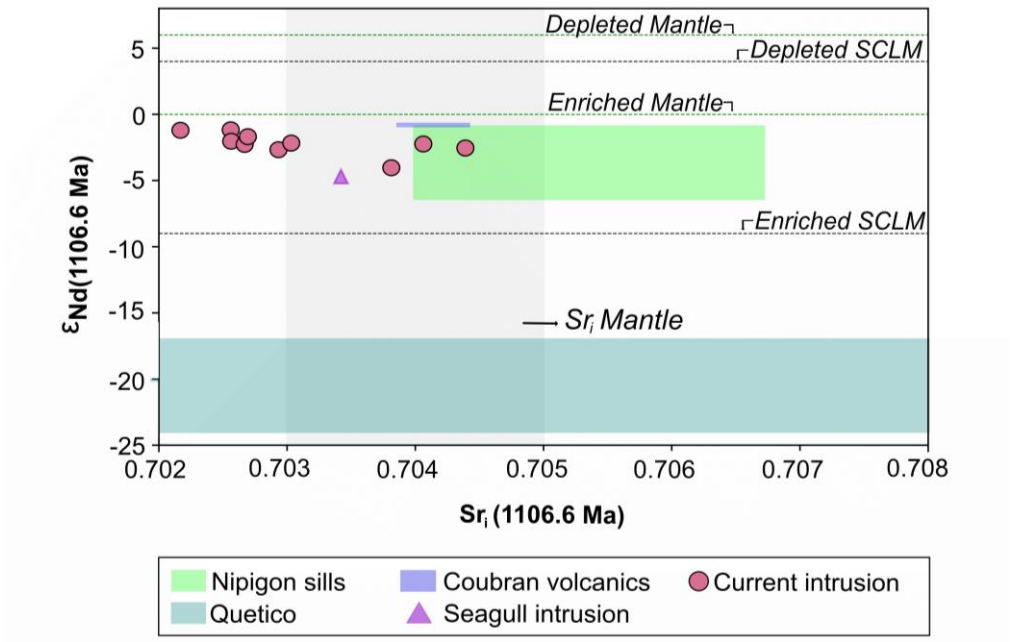

Figure 5.8: Binary diagrams of ε_{Nd} versus Sr_i for samples of three mineralized zones of the Current Intrusion (Current, Beaver-Cloud, and 437-SEA). Mantle, SCLM, and Quetico country rock values were taken from Hergt et al. (1989); Nicholson and Shirey (1990); Shirey et al. (1994); Shirey (1997); Henry et al. (1998); Pan et al. (1999); Rooney et al. (2022), and the Coubran volcanics, Nipigon sills, and Seagull intrusion data were taken from Heggie (2005), Hollings et al. (2007a), and Cundari (2012).

5.3 Stable Isotopes

Oxygen isotopes can indicate the potential sources of interaction/contamination of parental magmas with other reservoirs, as well as geological settings. Additionally, the pairing of oxygen and hydrogen isotopes can be used to better constrain the potential fluid sources where such interaction occurs (Rollinson & Pease, 2021). Six samples from the Beaver-Cloud and 437-SEA zones display δ^2H values ranging from -63 to -80 ‰ and $\delta^{18}O$ values from 5.5 to 7.0‰, characteristic of magmatic fluids sourced from mantle-derived magmas (δ^2H from -40 to -80 ‰ and $\delta^{18}O$ from 5.5 to 7.0‰; Taylor, 1968; Kyser et al., 1982; Kyser, 1986; Mattey et al., 1994;

Eiler et al., 1997; Loewen et al., 2019; Moine et al., 2020; Bindeman et al., 2022; Fig. 5.9). In contrast, samples from the Current and Bridge zones and most from the Beaver-Cloud and 437-SEA zones have values outside those typical of mantle-derived fluids (δ^2H <-80‰, $\delta^{18}O$ <5.5‰; Fig. 5.8). Additionally, two samples display $\delta^{18}O$ values greater than mantle-derived fluids ($\delta^{18}O$ >7‰; CAM-MB-21-177 and CAM-MB-21-101, situated proximal to the base of the intrusion at 667.85m in 437-SEA and 230.07m in the Beaver-Cloud zone, respectively). The Quetico country rocks display $\delta^{18}O$ values from 9.5 to 10.2‰ and δ^2H from -81 to -113‰ (Fig. 5.9).

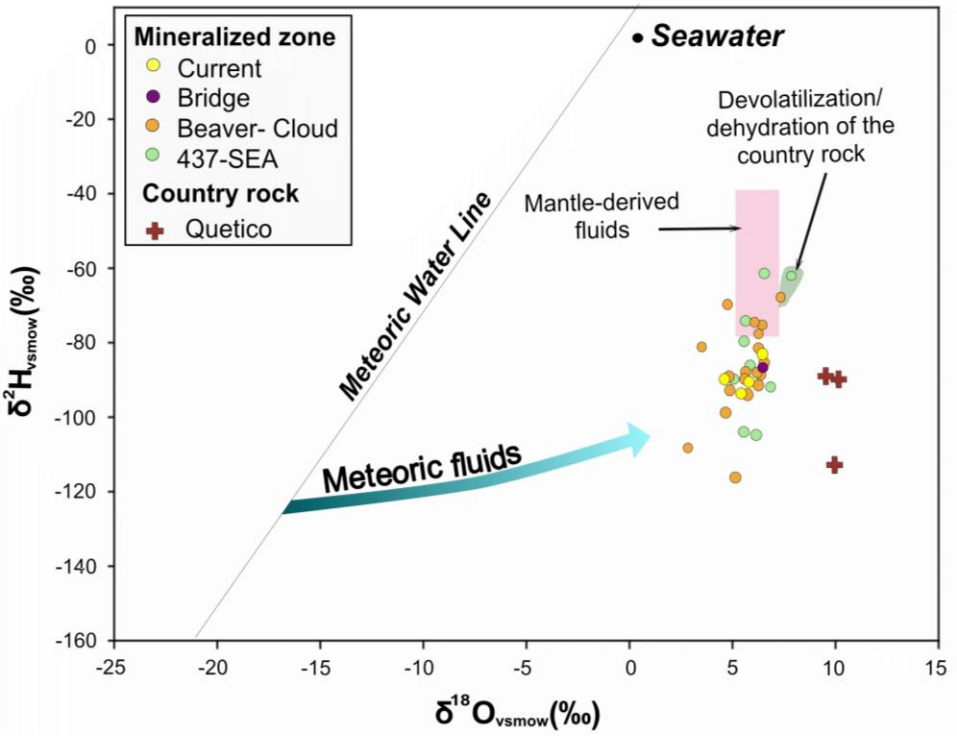

Figure 5.9: $\delta^{18}O$ and δ^2H values of bulk rock in the four mineralized zones of the Current Intrusion (Current, Bridge, Beaver-Cloud, and 437-SEA) and the surrounding country rock of the Quetico basin. The mantle fluids values were obtained from Taylor (1968); Kyser et al. (1982); Kyser (1986) Mattey et al. (1994); Eiler et al. (1997); Loewen et al. (2019); Moine et al. (2020); and Bindeman et al. (2022).

Ripley and Li (2007) suggested that mantle-derived rocks with $\delta^{18}O$ values exceeding typical mantle-derived values ($\delta^{18}O$ >7‰) could potentially indicate crustal contamination along the mantle-crustal pathway or within the upper crust resulting from melting of xenoliths or footwall rocks, as exemplified by the elevated $\delta^{18}O$ values in the Eagle Cu-Ni-PGE deposit in northern Michigan and in the Babbit Cu-Ni deposit in Minnesota ($\delta^{18}O$ values up to 12.2‰ and 15.5‰, respectively), which were interpreted to be the result of crustal contamination (Ripley & Al-Jassar, 1987; Ding et al., 2012). However, the absence of geochemical anomalies that support contamination in the Current Intrusion, as previously discussed, precludes crustal contamination for the samples with stable isotopes values exceeding the mantle values and instead suggests the possibility of the addition of heavy oxygen by devolatilization/dehydration of the country rock during the emplacement of the intrusion; this heavy oxygen can remain bound to hydrogen and subsequently be incorporated into hydrated minerals. A similar model was advocated by Ripley and Al-Jassar (1987) as one of the potential sources of contamination in the Babbit deposit.

The interaction of mantle-derived rocks with ocean water results in enrichment of the heavier H isotope (>-60‰) to mantle values (-40 to -80‰), as argued by LéCuyer et al. (1996) for the Proterozoic Chukotat Group in northern Quebec, where this interaction resulted in $\delta^{2}H$ values from -40 to -53‰ in the mafic-ultramafic rocks. In contrast, rocks interacting with meteoric fluids will have: i) $\delta^{18}O$ values lower than those expected from mantle-derived sources (<5.5‰; Li, 1991) and ii) $\delta^{2}H$ values lower than expected in mantle-derived rocks (<-80‰), as described by Ripley et al. (1993) and Park and Ripley (1999) for the Babbit Cu-Ni deposit. The interaction of meteoric fluids with the Current Intrusion could explain the $\delta^{2}H$ and $\delta^{18}O$ values that are lighter than those anticipated values for mantle-derived rocks in some of the samples (Fig. 5.9).

Based on the stable isotopes data, three possible sources of fluids, all independent of the alteration intensity, could have been involved in the hydrothermal alteration of the Current Intrusion: i) mantle-derived fluids, preserved chiefly at the bottom of the intrusion in the 437-SEA and Beaver-Cloud zones, generated the secondary mineralogical assemblages of Domain A and B (antigorite, lizardite-chrysotile, clinochlore, epidote, actinolite-tremolite, sericite) crystallized at temperatures above and below 300°C. ii) meteoric fluids, recorded mostly at the top of the intrusion along the four mineralized zones and, characterized by a secondary mineralogy similar to the derived from the mantle-derived fluids (Domain A and B) at temperatures above and below 300°C. iii) Devolatilization of the country rock (dehydration of the Quetico basin through contact aureoles), transporting fluids below 300°C, evident in Domain C with minerals, such as talc and carbonates that crosscut and alter the secondary mineralogy previously crystallized in domains A and B.

The mineralization appears to be strongly and similarly altered in domains A and B derived from both mantle-derived and meteoric sources, which substantially reduced the mineral volume of the primary sulfides and oxides (chalcopyrite, pyrrhotite, pentlandite, and magnetite) in the process of replacement by pyrite, secondary magnetite, and chamosite (Figs. 5.3, 5.4). Domain C (alteration episode overprinted on Domains A and B) does not show additional mineralization replacements with respect to Domains A and B.

5.5 Model for the Current Intrusion

5.5.1 Magmatic Evolution

During the transportation of the MRS related melt from its source in the mantle through the lithosphere to the base of the crust, varying levels of contamination may occur (Fig. 5.10). Brzozowski et al. (2022) proposed two scenarios: i) melts may originate from a depleted section

of the Keweenawan Plume that subsequently underwent contamination by Archean crustal material, such as the Nipigon sills and the Coubran basalt, based on their radiogenic γOs_i values and elevated Th, and ii) melts derived from partial melting of an enriched (metasomatized) SCLM underwent minimal to no contamination from Archean crustal materials during their emplacement, such as is the case for the Eva Kitto, Seagull, and Thunder intrusions, as well as the Shillabeer and Jackfish sills (given their positive γOs_i and negative ε_{Nd}). The Current Intrusion exhibits negative ε_{Nd} values ranging from -1.18 to -4.02, which are not consistent with depleted and enriched plume values, indicating instead potential interaction by SCLM. The geochemistry of the Current Intrusion suggests that it was not contaminated by the Quetico country rock, as indicated by the absence of anomalies in the HFSE relative to Th and instead that an enriched SCLM may be the likely source of the depleted ε_{Nd} values in the Current Intrusion. Similarly, the oxygen isotopes are also not consistent with contamination by Quetico rock; rather, they suggest devolatilization of the country rock. Upon emplacement of the melt, sulfide saturation likely occurred through the thermal aureole method (Robertson et al., 2015) given the lack of evidence of assimilation of continental crust.

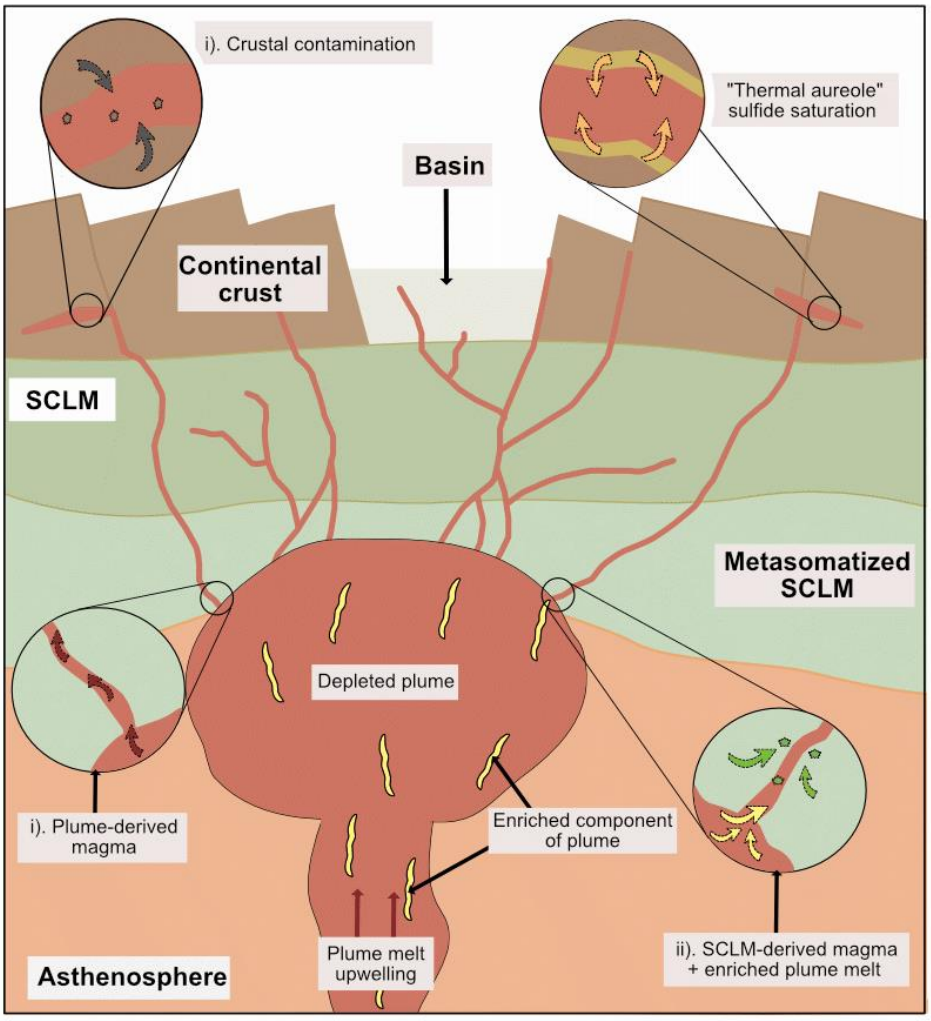

Figure 5.10: Schematic model of the Keweenawan Plume showing two potential scenarios. Scenario i) depleted plume-derived magma + crustal contamination, scenario proposed for the Coubran basalts and Nipigon sills by Brzozowski et al. (2022). ii) SCLM-derived magma + enriched plume melt and sulfide saturation by thermal aureole in the crust, scenario proposed for the Current Intrusion.

5.5.2 Hydrothermal Evolution

The stable isotope analysis of rocks from the Current Intrusion suggests interaction between mantle-derived fluids, meteoric fluids, and crust-derived fluids (Fig. 5.11). Through an assessment of alteration intensity and micro-textural features in the Current Intrusion, three mineralogically distinct alteration domains were identified. Domains A and B were the result of the interaction of

rock with meteoric and mantle-derived fluids. In contrast, Domain C is related to fluids sourced from devolatilization of the country rock (crustal-derived fluids) and was superimposed on domains A and B. The alteration in Domain A involved the replacement of olivine by magnetite, antigorite ± actinolite-tremolite, pyroxene by actinolite-tremolite, antigorite, clinochlore, and plagioclase by epidote, clinochlore and sericite; additionally, pyrite after pyrrhotite, secondary magnetite after chalcopyrite, pyrrhotite, and pentlandite, as well as secondary pyrrhotite after pyrite, and chamosite and pyrite after primary magnetite. In Domain B, antigorite, and unaltered olivine and pyroxene were replaced by lizardite-chrysotile, accompanied by an increase of modal abundance of epidote, sericite, and clinochlore, along with pyrite, secondary magnetite, and chamosite. Domain C is characterized by talc-carbonate minerals altering the secondary minerals of domains A and B. The replacement of primary minerals by secondary minerals in each domain suggests the involvement of different temperatures and fluid compositions during the alteration with acidic pH in domains A and B and basic Ph in Domain C. The alteration processes to which the Current Intrusion was subjected also involved an important reduction in mineral volume in the replacement of primary sulfides by secondary sulfides and oxides.

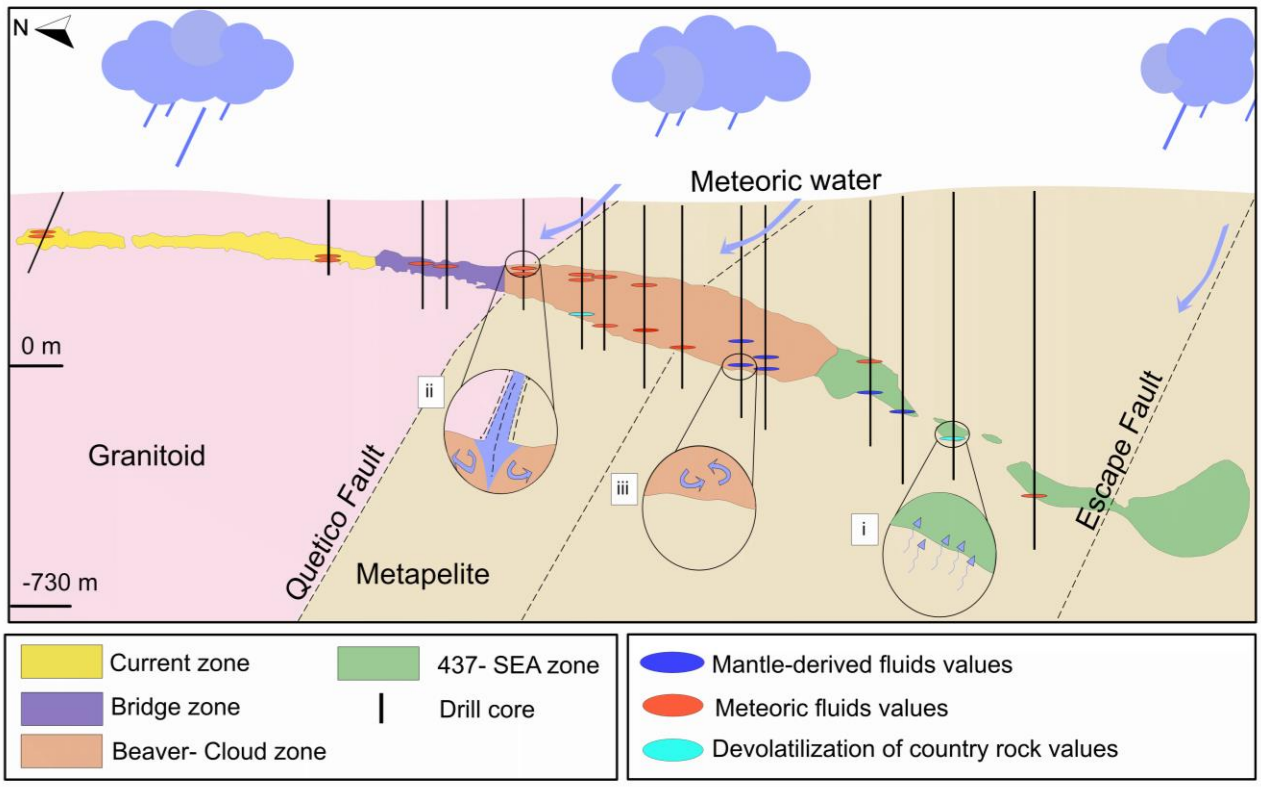

Figure 5.11: Schematic model illustrating the Current Intrusion and its interaction with three sources of fluids: i) devolatilization of the country rock; ii) meteoric fluids; iii) mantle-derived fluids.

6. CONCLUSIONS

The Current deposit, part of the Thunder Bay North Intrusive Complex, is related to the MRS and consists of mafic-ultramafic intrusion that hosts high-grade PGE-Cu-Ni magmatic mineralization. The main goals of this thesis were to: i) investigate the alteration assemblages and the fluids that formed them and ii) investigate the magmatic evolution of the intrusion and potential sources of contamination.

The Current Intrusion comprises wehrlite, lherzolite, olivine gabbronorite ± troctolite, based on petrographic and major elements analysis. The trace element data reveals a well-defined mantle-normalized pattern similar to OIB, with the enriched nature of the magma indicating a basaltic parental magma derived from an enriched mantle plume that was not contaminated by the Quetico country rock. However, the slightly lower ε_{Nd} values in the samples compared to the enriched plume are consistent with the parental magma having interacted with an enriched SCLM beneath the MRS.

Petrographic analysis suggests the early formation of euhedral and very fine-grained chromite, followed by phenocrysts of fine- to- medium-grained olivine crystallized to enclose the chromite. Subsequently, as the temperatures of the magmatic system decreased, oikocrysts of pyroxene enclosed olivine crystals, followed by the crystallization of plagioclase filling the remaining interstices. Magnetite-ilmenite and sulfides (pyrrhotite, chalcopyrite, and pentlandite) were observed interstitial to the mafic silicates, indicating crystallization after the olivine and pyroxenes and probably coeval with the plagioclase.

The Current zone is characterized by weak alteration intensity in most samples (<33.3% of alteration). The Beaver-Cloud zones exhibit moderate alteration in the majority of the samples (>33.33%, <66.66%). The 437-SEA samples are characterized by strong alteration intensity (>66.66%) at the top and bottom of the intrusion, but with weak to moderate alteration in the center of the intrusion. Three different assemblages of secondary minerals have been characterized the intrusion: i) Domain A, typified by antigorite-magnetite ±actinolite-tremolite replacing 10-60% of olivine, actinolite-tremolite, antigorite, and clinochlore altering pyroxene in boundaries and fractures with weak to moderate replacement (10 to 60%), epidote-sericite-clinochlore replacing plagioclase with weak to moderate replacement (5-60%). The stable isotope analysis in this domain indicates mantle-derived and meteoric fluids. ii). Domain B is characterized by the replacement of up to 100% of the olivines, pyroxenes, and antigorite by lizardite-chrysotile and an increase in the size and abundance of epidote, sericite and clinochlore (replacing plagioclase and pyroxenes with moderate to strong alteration intensity from 30-80%) with respect to Domain A. The stable isotope analysis in this domain suggests interaction with mantle-derived and meteoric fluids. Secondary magnetite and secondary pyrite, as well as chamosite are present in Domain A and B, replacing pyrrhotite, chalcopyrite, pentlandite, and primary magnetite with up to 100% replacement in pyrrhotite and primary magnetite, 50% in pentlandite and, 13% in chalcopyrite. Secondary pyrrhotite after secondary pyrite is observed only in Domain A. iii). Domain C, consisting of talc and carbonates, is characterized by the replacement of 100% secondary minerals from Domain A and B. Crustal fluids (devolatilization-dehydration), located at the bottom of the Beaver-Cloud and 437-SEA zone at the contact with the Quetico country rock, were defined for this domain given the stable isotope values.

The fluids have strongly altered the mineralization in domains B and A from both mantle-derived and meteoric sources, leading to a reduction in the volume of primary sulfides and oxides such as chalcopyrite, pyrrhotite, pentlandite, and magnetite by pyrite, secondary magnetite, and chamosite. Domain C represents an alteration episode superimposed on domains B and A; however, this domain does not show any additional replacement or mobilization of mineralization compared to domains A and B.

REFERENCES

Arnason, J. G., Bird, D. K., & Liou, J. G. (1993). Variables controlling epidote composition in hydrothermal and low-pressure regional metamorphic rocks, 17-25.

Arnold, R. G., Coleman, R. G., & Fryklund, V. C. (1962). Temperature of crystallization of pyrrhotite and sphalerite from the Highland-Surprise Mine, Coeur D'Alene District, Idaho. Economic Geology, 57(8), 1163-1174.

Barnes, I., O'Neill, J. R., Rapp, J. B., & White, D. E. (1973). Silica-Carbonate Alteration of Serpentine; Wall Rock Alteration in Mercury Deposits of the California Coast Ranges. Economic Geology and The Bulletin Of The Society Of Economic Geologists, 68(3), 388-398. https://doi.org/10.2113/gsecongeo.68.3.388

Barnes, S. J., & Liu, W. (2012). Pt and Pd mobility in hydrothermal fluids: evidence from komatiites and from thermodynamic modelling. Ore Geology Reviews, 44, 49-58.

Barnes, S. J., Achterbergh, E., Makovicky, E., & Li, C. (2001a). Proton probe results for partitioning of platinum group elements between monosulphide solid solution and sulphide liquid. South African Journal of Geology, 104, 275-286. https://doi.org/10.2113/gssajg.104.4.275

Barnes, S., & Lightfoot, P.C. (2005). Formation of magmatic nickel-sulfide ore deposits and processses affecting their copper and platinum-group element contents. Economic Geology, 100, 179-213. https://doi.org/10.5382/AV100.08

Barnes, S., Melezhik, V. A., & Sokolov, S. V. (2001b). The composition and mode of formation of the Pechenga Nickel deposits, Kola Peninsula, Northwestern Russia. Canadian Mineralogist, 39(2), 447-471. https://doi.org/10.2113/gscanmin.39.2.447

Basaltic Volcanism Study Project. (1981). Basaltic volcanism on the terrestrial planets. Pergamon Press, Inc. New York (pp.1286). https://ads.harvard.edu/books/bvtp/

Begg, G. C., Hronsky, J. A. M., Arndt, N. T., Griffin, W. L., O'Reilly, S. Y., & Hayward, N. (2010). Lithospheric, Cratonic, and Geodynamic Setting of Ni-Cu-PGE Sulfide Deposits. Economic Geology, 105(6), 1057-1070. doi:10.2113/econgeo.105.6.1057 10.2113/econgeo.105.6.1057

Bindeman, I. N., Ionov, D. A., Tollan, P. M., & Golovin, A. V. (2022). Oxygen isotope (δ18O, Δ′ 17O) insights into continental mantle evolution since the Archean. Nature Communications, 13(1), 3779.

Bleeker, W., Smith, J., Hamilton, M., Kamo, S., Liikane, D., Hollings, P., Cundari, R., Easton, M., and Davis, D., (2020). The Midcontinent Rift and its mineral systems: Overview and temporal constraints of Ni-Cu-PGE mineralized intrusions. Targeted Geoscience Initiative 5: Advances in the understanding of Canadian Ni-Cu-PGE and Cr ore systems Examples from the Midcontinent Rift, the Circum-Superior Belt, the Archean Superior Province, and Cordilleran Alaskan-type intrusions, (ed.) W. Bleeker and M.G. Houlé; Geological Survey of Canada, Open File 8722, 7-35. https://doi.org/10.4095/326880

Brzozowski, M. J., Hollings, P., Heggie, G. J., MacTavish, A. D., Wilton, D. H. C., & Evans-Lamswood, D. (2023). Characterizing the supra- and subsolidus processes that generated the current PGE-Cu-Ni deposit, Thunder Bay North Intrusive Complex, Canada: Insights from trace elements and multiple S isotopes of sulfides. Mineralium Deposita, 58(8), 1559-1581. https://doi.org/10.1007/s00126-023-01193-9

Brzozowski, M. J., Hollings, P., Zhu, J., & Creaser, R. A. (2022). Osmium isotopes record a complex magmatic history during the early stages of formation of the North American Midcontinent rift-Implications for rift initiation. Lithos, 436-437, 106966. https://doi.org/10.1016/j.lithos.2022.106966

Caglioti, C. (2023). PGE-Cu-Ni sulfide mineralization of the Mesoproterozoic Escape intrusion, northwestern Ontario (MSc). Lakehead University, Thunder Bay, Ontario (pp. 242). https://knowledgecommons.lakeheadu.ca/handle/2453/5195

Cannon, W. F., & Hinze, W. J. (1992). Speculations on the origin of the North American Midcontinent rift. Tectonophysics, 213(1-2), 49-55.

Card, K. D., & Ciesielski, A. (1986). Subdivisions of the Superior province of the Canadian Shield. Geoscience Canada, 13(1), 5-13.

Chaliulina, R. (2019). Precipitated Calcium Carbonates: Recycling Carbon Dioxide and Industrial Waste Brines. University of Aberdeen, United Kingdom (pp. 259) DOI:10.13140/RG.2.2.27644.05765

Chalokwu, C. I. (1985). A geochemical, petrological, and compositional study of the Partridge River Intrusion, Duluth Complex, Minnesota. Miami University (pp. 232).

Clean Air Metals Inc. (2023, May 4). Clean Air Metals Announces the New SLR Mineral Resource Estimate for the Thunder Bay North Critical Metals Project with an Indicated Resource of 14.0 million tonnes containing 1.2 million ounces of 2PGE (Pt+Pd) 57,500 tonnes of Cu and 34,300 tonnes of Ni. 2023 News Releases. https://cleanairmetals.ca/news-media/news-releases/clean-air-metals-announces-the-new-slr-mineral-res-122566/

Craig, J. R., & Kullerud, G. (1969). Phase Relations in the Cu-Fe-Ni-S System and Their Application to Magmatic Ore Deposits. Economic Geology, 344-358. https://doi.org/10.5382/mono.04.25

Cundari, R. (2012). Geology and Geochemistry of Midcontinent rift-related igneous rocks (MSc). Lakehead University, Thunder Bay, Ontario (pp. 154). https://knowledgecommons.lakeheadu.ca/handle/2453/399

Dare, S. A., Barnes, S. J., Prichard, H. M., & Fisher, P. C. (2011). Chalcophile and platinum-group element (PGE) concentrations in the sulfide minerals from the McCreedy East deposit, Sudbury, Canada, and the origin of PGE in pyrite. Mineralium Deposita, 46, 381-407 https://doi.org/10.1007/s00126-011-0336-9

Dare, S. A., Barnes, S. J., & Beaudoin, G. (2012). Variation in trace element content of magnetite crystallized from a fractionating sulfide liquid, Sudbury, Canada: Implications for provenance discrimination. Geochimica et Cosmochimica, 88, 27-50. https://doi.org/10.1016/j.gca.2012.04.032

Davis, D. W., Pezzutto, F., & Ojakangas, R. W. (1990). The age and provenance of metasedimentary rocks in the Quetico Subprovince, Ontario, from single zircon analyses: implications for Archean sedimentation and tectonics in the Superior Province. Earth and Planetary Science Letters, 99(3), 195-205.

Deer, W. A., Howie, R.A., Zussman, J. (1992). Rock forming minerals. Mineralogical Magazine, 56(385), 617-619.

Ding, X., Ripley, E. M., Shirey, S. B., & Li, C. (2012). Os, Nd, O and S isotope constraints on country rock contamination in the conduit-related eagle Cu-Ni-(PGE) Deposit, Midcontinent Rift System, Upper Michigan. Geochimica et Cosmochimica, 89, 10-30. https://doi.org/10.1016/j.gca.2012.04.029

Eiler, J. M., Farley, K. A., Valley, J. W., Hauri, E., Craig, H., Hart, S. R., & Stolper, E. M. (1997). Oxygen isotope variations in ocean island basalt phenocrysts. Geochimica et Cosmochimica Acta, 61(11), 2281-2293.

Evans, B. W. (2004). The serpentinite multisystem revisited: Chrysotile is metastable. International Geology Review, 46(6), 479-506. https://doi.org/10.2747/0020-6814.46.6.479

Ewers, W. E., Graham, J., Hudson, D. R., & Rolls, J. M. (1976). Crystallization of chromite from nickel-iron sulphide melts. Contributions to Mineralogy and Petrology, 54, 61-64.

Fleet, M. E., & Pan, Y. (1994). Fractional crystallization of anhydrous sulfide liquid in the system FE-NI-CU-S, with application to magmatic sulfide deposits. Geochimica et Cosmochimica, 58(16), 3369-3377. https://doi.org/10.1016/0016-7037(94)90092-2

Fonseca, R. O. C., Campbell, I. H., O'Neill, H. St. C., & FitzGerald, J. D. (2008). Oxygen solubility and speciation in sulphide-rich mattes. Geochimica et Cosmochimica, 72(11), 2619-2635. https://doi.org/10.1016/j.gca.2008.03.009

Fulignati, P. (2020). Clay minerals in hydrothermal systems. Minerals, 10(10), 919. https://doi.org/10.3390/min10100919

Good, D. J., Epstein, R., McLean, K., Linnen, R. L., & Samson, I. M. (2015). Evolution of the Main Zone at the Marathon Cu-PGE sulfide deposit, Midcontinent Rift, Canada: spatial relationships in a magma conduit setting. Economic Geology, 110(4), 983-1008.

Good, D., & Lightfoot, P. C. (2019). Significance of the metasomatized lithospheric mantle in the formation of early basalts and Cu- platinum group element sulfide mineralization in the Coldwell Complex, Midcontinent Rift, Canada. Canadian Journal of Earth Sciences, 56(7), 693-714. https://doi.org/10.1139/cjes-2018-0042

Good, D., Hollings, P., Dunning, G. R., Epstein, R., McBride, J. H., Jedemann, A., Magnus, S., Bohay, T., & Shore, G. T. (2021). A new model for the Coldwell Complex and associated dykes of the Midcontinent Rift, Canada. Journal of Petrology, 62(7). https://doi.org/10.1093/petrology/egab036

Griffin, W. L., & O'Reilly, S. Y. (2007). The earliest subcontinental lithospheric mantle. Developments in Precambrian Geology, 15, 1013-1035. https://doi.org/10.1016/s0166-2635(07)15082-9

Heggie, G. (2005). Whole rock geochemistry, mineral chemistry, petrology and Pt, Pd mineralization of the Seagull Intrusion, Northwestern Ontario. Lakehead University (MSc), Thunder Bay, Ontario (pp. 365). https://knowledgecommons.lakeheadu.ca/handle/2453/689

Henry, P., Stevenson, R., & Gariépy, C. (1998). Late Archean mantle composition and crustal growth in the Western Superior Province of Canada: neodymium and lead isotopic evidence from the Wawa, Quetico, and Wabigoon subprovinces. Geochimica et Cosmochimica, 62(1), 143-157. https://doi.org/10.1016/s0016-7037(97)00324-4

Hergt, J., Chappell, B. W., McCulloch, M. T., McDougall, I., & Chivas, A. R. (1989). Geochemical and isotopic constraints on the origin of the Jurassic Dolerites of Tasmania. Journal of Petrology, 30(4), 841-883. https://doi.org/10.1093/petrology/30.4.841

Hinze, W. J., & Chandler, V. W. (2020). Reviewing the configuration and extent of the Midcontinent rift system. Precambrian Research, 342, 105688. doi:10.1016/j.precamres.2020.10568810.1016/j.precamres.2020.105688

Hocq, M. (1994). Géologie du Québec. Ministère des ressources naturelles, Québec, 94(1), 166.

Hofmann, A. W. (1997). Mantle Geochemistry: The message from Oceanic volcanism. Nature, 385(6613), 219-229. https://doi.org/10.1038/385219a0

Hollings, P., & Cundari, R. (2020). Ni-Cu-PGE mineralization of the 1.1 Ga Midcontinent Rift of N. America: rethinking models for the rift and the implications for mineralization. Mineral Deposits Studies Group, 43rd Annual Meeting, 6–8 January 2020 Natural History Museum, London, Program and Abstracts (pp. 24).

Hollings, P., Hart, T. R., Richardson, A., & MacDonald, C. A. (2007a). Geochemistry of the Mesoproterozoic intrusive rocks of the Nipigon Embayment, Northwestern Ontario: Evaluating the earliest phases of rift development. Canadian Journal of Earth Sciences, 44(8), 1087-1110. https://doi.org/10.1139/e06-127

Hollings, P., Richardson, A., Creaser, R. A., & Franklin, J. M. (2007b). Radiogenic isotope characteristics of the Mesoproterozoic intrusive rocks of the Nipigon Embayment, northwestern Ontario. Canadian Journal of Earth Sciences, 44(8), 1111-1129. https://doi.org/10.1139/e06-128

Holwell, D. A., & McDonald, I. (2010). A review of the behaviour of platinum group elements within natural magmatic sulfide ore systems. Platinum Metals Review, 54(1), 26-36. https://doi.org/10.1595/147106709x480913

Holwell, D. A., Adeyemi, Z., Ward, L. A., Smith, D. J., Graham, S., McDonald, I., & Smith, J. (2017). Low temperature alteration of magmatic Ni-Cu-PGE sulfides as a source for hydrothermal Ni and PGE ores: a quantitative approach using automated mineralogy. Ore Geology Reviews, 91, 718-740. https://doi.org/10.1016/j.oregeorev.2017.08.025

Keith, T. E., Muffler, L. P., & Cremer, M. (1968). Hydrothermal epidote formed in the Salton Sea geothermal system, California. American Mineralogist: Journal of Earth and Planetary Materials, 53(9-10), 1635-1644.

Kelemen, P. B., & Matter, J. M. (2008). In situ carbonation of peridotite for CO2 storage. Proceedings of the National Academy of Sciences, 105(45), 17295-17300. https://doi.org/10.1073/pnas.0805794105

Krogh, T. E., & Turek, A. (1982). Precise U-Pb zircon ages from the Gamitagama greenstone belt, southern Superior Province. Canadian Journal of Earth Sciences, 19(4), 859-867.

Kuntz, G., Wissent, B., Boyko, K., Harkonen, H., Jones, L., Muir, W., Buss, B., & Peacock, B. (2022) NI 43-101 Technical report and preliminary economic assessment for the Thunder Bay North Project, Thunder Bay, Ontario. Clean Air Metals Inc., Thunder Bay, ON, Canada

Kushiro, I. (1979). Chapter 6. Fractional Crystallization of Basaltic Magma. The evolution of the igneous rocks. Princeton University Press eBooks, 171-204. https://doi.org/10.1515/9781400868506-007

Kyser, T. K., O'Neil, J. R., & Carmichael, I. S. E. (1982). Genetic relations among basic lavas and ultramafic nodules: evidence from oxygen isotope compositions. Contributions to Mineralogy and Petrology, 81(2), 88-102. https://doi.org/10.1007/bf00372046

Kyser, T. K. (1986). Stable isotope variations in the mantle. Reviews in Mineralogy and Geochemistry, 16(1), 141-164.

Lagat, J. (2009). Hydrothermal alteration mineralogy in geothermal fields with case examples from Olkaria domes geothermal field, Kenya. SDG Short Course I on Exploration and Development of Geothermal Resources. 10-31 November 2016 Lake Bogoria and Lake Naivasha, Kenya.

Le Maitre, R. W. (1989). A Classification of Igneous Rocks and Glossary of Terms: Recommendations of the International Union of Geological Sciences Subcommission on the Systematics of Igneous Rocks. http://ci.nii.ac.jp/ncid/BA0727526X?l=en

LéCuyer, C., Gruau, G., Früh-Green, G. L., Picard, C. (1996). Hydrogen isotope composition of Early Proterozoic seawater. GeoScienceWorld. 24 (4), 291-294. https://doi.org/10.1130/0091-7613(1996)024<0291:HICOEP>2.3.CO;2

Li, C., & Naldrett, A. J. (1993). Sulfide capacity of magma; a quantitative model and its application to the formation of sulfide ores at Sudbury, Ontario. Economic geology and the bulletin of the Society of Economic Geologists, 88(5), 1253-1260. https://doi.org/10.2113/gsecongeo.88.5.1253

Li, C., & Ripley, E. M. (2011). Magmatic Ni-Cu and PGE deposits: geology, geochemistry, and genesis. Economic Geology. https://doi.org/10.5382/Rev.17

Li, C., Ripley, E. M., Maier, W. D., & Gomwe, T. E. S. (2002). Olivine and sulfur isotopic compositions of the Uitkomst Ni-Cu Sulfide ore-bearing Complex, South Africa: evidence for sulfur contamination and multiple magma emplacements. Chemical Geology, 188(3-4), 149-159. https://doi.org/10.1016/s0009-2541(02)00098-0

Li, D., Hollings, P., Chen, H., Sun, X., Tan, C., & Zurevinski, S. (2020). Zircon U–Pb and Lu–Hf systematics of the major terranes of the Western Superior Craton, Canada: Mantle-crust interaction and mechanism (s) of craton formation. Gondwana Research, 78, 261-277.

Li, H. (1991). Oxygen and Hydrogen Isotope Studies of Metamorphic Rocks in the Wawa-Kapuskasing Crustal Transect. Mcmaster University, Hamilton, Ontario (pp. 138).

Li, Y., Huang, F., Gao, W., Tang, X., Ren, Y., Meng, L., & Zhang, Z. (2019). Experimental Study of Dissolution-Alteration of Amphibole in a Hydrothermal Environment. Geologica Sinica, 93(6), 1933-1946

Loewen, M. W., Graham, D. W., Bindeman, I. N., Lupton, J. E., & Garcia, M. O. (2019). Hydrogen isotopes in high 3He/4He submarine basalts: primordial vs. recycled water and the veil of mantle enrichment. Earth and Planetary Science Letters, 508, 62-73. https://doi.org/10.1016/j.epsl.2018.12.012

Mackasey, W. O., Blackburn, C. E., & Trowell, N. F. (1974). A regional approach to the Wabigoon-Quetico belts and its bearing on exploration in northwestern Ontario. Ontario Division of Mines, 58 (pp. 29).

Mattey, D. P., Lowry, D., & Macpherson, C. G. (1994). Oxygen isotope composition of mantle peridotite. Earth and Planetary Science Letters, 128(3-4), 231-241. https://doi.org/10.1016/0012-821x(94)90147-3

Moine, B. N., Bolfan-Casanova, N., Radu, I. B., Ionov, D. A., Costin, G., Korsakov, A. V., Golovin, A.V., Oleinikov, O.B., Deloule, E., Cottin, J.Y., & Cottin, J. Y. (2020). Molecular hydrogen in minerals as a clue to interpret∂ D variations in the mantle. Nature Communications, 11(1), 3604. https://doi.org/10.1038/s41467-020-17442-8

Naldrett, A. J. (1969). A portion of the system Fe-S-O between 900 and 1080 C and its application to sulfide ore magmas. Journal of Petrology, 10(2), 171-201. https://doi.org/10.1093/petrology/10.2.171

Naldrett, A. J. (1981). Nickel sulfide deposits: classification, composition, and genesis. Economic geology. Seventy-Fifth Anniversary Volume, 628-685. https://doi.org/10.5382/AV75.16

Naldrett, A. J. (1999). World-class Ni-Cu-PGE deposits: key factors in their genesis. Mineralium Deposita, 34, 227-240. https://doi.org/10.1007/s001260050200

Naldrett, A. J. (2004). Magmatic sulfide deposits: Geology, Geochemistry and Exploration. In Springer (pp. 186). https://doi.org/10.1007/978-3-662-08444-1

Naldrett, A. J., Bruegmann, G. E., & Wilson, A. H. (1990). Models for the concentration of PGE in layered intrusions. The Canadian Mineralogist, 28(3), 389-408.

Naldrett, A. J., Singh, J., Krstic, S., & Li, C. (2000). The mineralogy of the Voisey's Bay Ni-Cu-Co deposit, northern Labrador, Canada: Influence of oxidation state on textures and mineral compositions. Economic Geology, 95(4), 889-900.

Nicholson, S. W., & Shirey, S. B. (1990). Midcontinent rift volcanism in the Lake Superior region: Sr, Nd, and Pb isotopic evidence for a mantle plume origin. Journal of Geophysical Research, 95(B7), 10851-10868. https://doi.org/10.1029/jb095ib07p10851

Nicholson, S. W., Schulz, K. J., Shirey, S. B., & Green, J. C. (1997). Rift-wide correlation of 1.1 Ga Midcontinent rift system basalts: implications for multiple mantle sources during rift

development. Canadian Journal of Earth Sciences, 34(4), 504-520. 34(4): 504-520. https://doi.org/10.1139/e17-041

O'Hanley, D. S. (1996). Serpentinites: records of tectonic and petrological history. Geological Magazine, 135, 143-158. https://doi.org/10.1017/S0016756897408257

Pan, Y., Fleet, M. E., & Longstaffe, F. J. (1999). Melt-related metasomatism in mafic granulites of the Quetico subprovince, Ontario: constraints from O-Sr-Nd isotopic and fluid inclusion data. Canadian Journal of Earth Sciences, 36(9), 1449-1462. https://doi.org/10.1139/e99-041

Park, Y., & Ripley, E. M. (1999). Hydrothermal flow systems in the Midcontinent Rift: oxygen and hydrogen isotopic studies of the North Shore Volcanic Group and related hypabyssal sills, Minnesota. Geochimica Et Cosmochimica, 63(11-12), 1787-1804. https://doi.org/10.1016/s0016-7037(99)00101-5

Pearce, J. A. (1983). Role of the sub-continental lithosphere in magma genesis at active continental margins. Continental basalts and mantle xenoliths, 230-249.

Percival, J. A. (1989). A regional perspective of the Quetico metasedimentary belt, Superior Province, Canada. Canadian Journal of Earth Sciences, 26(4), 677-693. doi:10.1139/e89-058

Percival, J. A., & Card, K. D. (1983). Archean crust as revealed in the Kapuskasing uplift, Superior Province, Canada. Geology, 11(6), 323-326.

Percival, J. A., & Krogh, T. E. (1983). U-Pb zircon geochronology of the Kapuskasing structural zone and vicinity in the Chapleau-Foleyet area, Ontario. Canadian Journal of Earth Sciences, 20(5), 830-843.

Percival, J. A., & Williams, H. R. (1989). Late Archean Quetico accretionary complex, Superior Province, Canada. Geology, 17(1), 23-25. https://doi.org/10.1130/0091-7613(1989)017%3C0023:LAQACS%3E2.3.CO;2

Percival, J. A., Sanborn-Barrie, M., Skulski, T., Stott, G. M., Helmstaedt, H., & White, D. J. (2006). Tectonic evolution of the Western Superior Province from NATMAP and Lithoprobe studies. Canadian Journal of Earth Sciences, 43(7), 1085-1117. https://doi.org/10.1139/e06-062

Ripley, E. M. (1981). Sulfur isotopic studies of the Dunka Road Cu-Ni deposit, Duluth Complex, Minnesota. Economic Geology, 76(3), 610-620.

Ripley, E. M. and LI, C. (2007). Applications of Stable and Radiogenic Isotopes to Magmatic Cu-Ni-PGE Deposits: Examples and Cautions. Earth Science Frontiers, Volume 14, 124-131. https://doi.org/10.1016/S1872-5791(07)60041-4

Ripley, E. M., & Alawi, J. A. (1988). Petrogenesis of pelitic xenoliths at the Babbitt Cu- Ni deposit, Duluth Complex, Minnesota, USA. Lithos, 21(2), 143-159.

Ripley, E. M., & Al-Jassar, T. J. (1987). Sulfur and Oxygen isotope Studies of melt-country rock Interaction, Babbitt Cu-Ni Deposit, Duluth Complex, Minnesota. Economic Geology and

the bulletin of the Society of Economic Geologists, 82(1), 87-107. https://doi.org/10.2113/gsecongeo.82.1.87

Ripley, E. M., Butler, B. K., Taib, N. I., & Lee, I. (1993). Hydrothermal alteration in the Babbitt CU-NI deposit, Duluth Complex; Mineralogy and Hydrogen isotope systematics. Economic Geology and the bulletin of the Society of Economic Geologists, 88(3), 679-696. https://doi.org/10.2113/gsecongeo.88.3.679

Ripley, E. M., Lightfoot, P. C., Li, C., & Elswick, E. (2003). Sulfur isotopic studies of continental flood basalts in the Noril'sk region: implications for the association between Lavas and ore-bearing intrusions. Geochimica et Cosmochimica, 67(15), 2805-2817. https://doi.org/10.1016/s0016-7037(03)00102-9

Robertson, J., Ripley, E. M., Barnes, S. J., & Li, C. (2015). Sulfur liberation from country rocks and incorporation in mafic magmas. Economic geology and the bulletin of the Society of Economic Geologists, 110(4), 1111-1123. https://doi.org/10.2113/econgeo.110.4.1111

Robinson, D., & Zamora, A. (1999). The smectite to chlorite transition in the Chipilapa Geothermal System, El Salvador. American Mineralogist, 84(4), 607-619. https://doi.org/10.2138/am-1999-0414

Rollinson, H. R., & Pease, V. (2021). Using geochemical data: to understand geological processes. Cambridge University Press.

Rooney, T. O., Konter, J. G., Finlayson, V., LaVigne, A., Brown, E. L., Stein, C. A., Stein, S., & Moucha, R. (2022). Constraining the isotopic endmembers contributing to 1.1 GA Keweenawan Large igneous province magmatism. Contributions to Mineralogy and Petrology, 177(4). https://doi.org/10.1007/s00410-022-01907-8

Sassani, D. C., & Pasteris, J. D. (1988). Preliminary investigation of alteration in a basal section of the southern Duluth Complex, Minnesota, and the effects on sulfide and oxide mineralization. In North American Conference on Tectonic Control of Ore Deposits and the Vertical and Horizontal Extent of Ore Systems, Proceedings Volume, 280-291. Missouri University of Science and Technology.

Schiffman, P., & Staudigel, H. (1995). The smectite to chlorite transition in a fossil Seamount hydrothermal system: the basement complex of La Palma, Canary Islands. Journal of Metamorphic Geology, 13(4), 487-498. https://doi.org/10.1111/j.1525-1314.1995.tb00236.x

Schoklitsch, K. (1935). Beitrag zur Physiographie steirischer Karbonspäte: (Gitterkonstanten, physikalische Angaben und chemische Zusammensetzung.). Zeitschrift für Kristallographie-Crystalline Materials, 90(1-6), 433-445.

Shirey, S. B. (1997). Re-Os Isotopic Compositions of Midcontinent Rift System picrites: Implications for plume- lithosphere interaction and Enriched mantle sources. Canadian Journal of Earth Sciences, 34(4), 489-503. https://doi.org/10.1139/e17-040

Shirey, S. B., Klewin, K. W., Berg, J., & Carlson, R. W. (1994). Temporal changes in the sources of flood basalts: isotopic and trace element evidence from the 1100 Ma old Keweenawan

Mamainse Point Formation, Ontario, Canada. Geochimica et Cosmochimica, 58(20), 4475-4490. https://doi.org/10.1016/0016-7037(94)90349-2

Simmons, S. W., & Christenson, B. (1994). Origins of calcite in a boiling geothermal system. American Journal of Science, 294(3), 361-400. https://doi.org/10.2475/ajs.294.3.361

Snelling, N. J. (1957). Notes on the Petrology and Mineralogy of the Barrovian Metamorphic Zones. Geological Magazine, 94(4), 297-304. https://doi.org/10.1017/s0016756800068734

Stott, G.M. (1997). The Superior Province, Canada. Greenstone belts, Clarendon Press, Oxford, 480-507.

Stott, G. M., Corkery, M. T., Percival, J. A., Simard, M., & Goutier, J. (2010). A revised terrane subdivision of the Superior Province. Summary of field work and other activities, 20-1.

Streckeisen, A. (1974). Classification and Nomenclature of plutonic rocks Recommendations of the IUGS Subcommission on the Systematics of Igneous Rocks. Geologische Rundschau (1910. Print), 63(2), 773-786. https://doi.org/10.1007/bf01820841

Sun, S., & McDonough, W. F. (1989). Chemical and Isotopic Systematics of Oceanic basalts: Implications for mantle composition and processes. Geological Society, London, Special Publications, 42(1), 313-345. https://doi.org/10.1144/gsl.sp.1989.042.01.19

Sutcliffe, R. H. (1991). Proterozoic geology of the Lake Superior area. Ontario Geological Survey, Special Volume, 4(Part 1), 627-658.

Swanson-Hysell, N. L., Ramezani, J., Fairchild, L. M., & Rose, I. (2019). Failed rifting and fast drifting: Midcontinent rift development, Laurentia's rapid motion and the driver of Grenvillian orogenesis. Geological Society of America Bulletin, 131(5-6), 913-940. https://doi.org/10.1130/b31944.1

Taylor, H. P. (1968). The oxygen isotope geochemistry of igneous rocks. Contributions to Mineralogy and Petrology, 19(1), 1-71. https://doi.org/10.1007/bf00371729

Thomas, D. G., Melnyk, J., Gormely, L., Searston, S., & Kulla, G. (2011). Magma metals limited Thunder Bay north polymetallic project Ontario, Canada. NI 43-101 Technical Report on Preliminary Assessment. Internal Report AMEC, Vancouver, BC (pp. 209).

Trevisan, B. E. (2014). The Petrology, Mineralization, and Regional Context of the Thunder Mafic to Ultramafic Intrusion, Midcontinent Rift, Thunder Bay, Ontario. Lakehead University (MSc), Thunder Bay, Ontario (pp. 300). https://www.lakeheadu.ca/programs/departments/geology/about/msctheses/summaries/node/24243

Valli, F., Guillot, S., & Hattori, K. H. (2004). Source and tectono-metamorphic evolution of mafic and pelitic metasedimentary rocks from the central Quetico metasedimentary belt, Archean Superior Province of Canada. Precambrian Research, 132(1-2), 155-177. doi:10.1016/j.precamres.2004.03.002 10.1016/j.precamres.2004.03.002

Welch, M. D., & Marshall, W. G. (2015). High-pressure behavior of clinochlore. American Mineralogist, 86(11-12), 1380-1386. https://doi.org/10.2138/am-2001-11-1206

Williams, H. R. (1991). Quetico Subprovince. In: Thurston, P.C., Williams, H.R., Sutcliffe, R.H., Stott, G.M. (Eds.), Geologyof Ontario. Ontario Geological Survey Special Vol. 4. Ontario Geological Survey, Ontario, Canada, 383–403

Woodruff, L. G., Schulz, K. J., Nicholson, S. W., & Dicken, C. L. (2020). Mineral deposits of the Mesoproterozoic Midcontinent Rift system in the Lake Superior region-a space and time classification. Ore Geology Reviews, 126, 103716. doi:10.1016/j.oregeorev.2020.103716

Yahia, K. (2023). Geochemistry, petrography, geochronology, and radiogenic isotopes of the weakly mineralized intrusions in Thunder Bay North Igneous Complex (MSc). Lakehead University, Thunder Bay, Ontario (pp. 148). https://knowledgecommons.lakeheadu.ca/handle/2453/5283

Zaleski, E., van Breemen, O., & Peterson, V. L. (1999). Geological evolution of the Manitouwadge greenstone belt and Wawa-Quetico subprovince boundary, Superior Province, Ontario, constrained by U-Pb zircon dates of supracrustal and plutonic rocks. Canadian Journal of Earth Sciences, 36(6), 945-966.

Zientek, M. L. (2012). Magmatic ore deposits in layered intrusions-Descriptive model for reef-type PGE and contact-type Cu-Ni-PGE deposits. U.S. Geological Survey Open-File Report 2012-1010 (pp. 48). https://pubs.usgs.gov/of/2012/1010/

APPENDIX A- Petrographic Descriptions

CAM-AC-2022-02		
Rock classification: wehrlite		
Silicates	**Sulfides**	**Oxides**
90% silicates **Clinopyroxene** Grain size: 2mm Texture: Poikilitic. Pyroxene as oikocryst enclosing smaller olivine. Abundance: 20% Alteration: 10% to lizardite-chrysotile along the fractures. **Orthopyroxene** Grain size: 1.5mm Texture: Poikilitic Abundance: 3% Alteration: 10% to lizardite-chrysotile with hourglass texture along the fractures. **Olivine** Grain size: 0.5mm Texture: Poikilitic- mesh-bastite Abundance: 60% Alteration: 70% to lizardite-chrysotile-magnetite with concentric growth in fractures and boundaries. **Plagioclase** **Anorthite** Grain size: 1.3mm Texture: polysynthetic twinning Abundance: 7%. Occurring interstitially in pyroxene and olivine Alteration: 5% to sericite.	**8% sulfides** **Pyrrhotite** Grain size:1.1mm Texture: pentlandite flames "exsolution texture." Filling interstices of silicates. Abundance: 5% Alteration: 5% to magnetite along fractures. **Chalcopyrite** Grain size: 0.6mm Texture: subhedral, filling interstices of silicates Abundance: 3% Alteration: 5% to magnetite along fractures. **Pentlandite** Grain size: 0.01mm Texture: subhedral filling interstices of silicates Abundance: 1% Alteration: 5% to magnetite.	**2% oxides** **Magnetite** Grain size: 0.4mm Texture: exsolution texture with ilmenite Abundance: 1.5% Alteration: unaltered mineral **Ilmenite** Grain size: 0.1mm Texture: exsolution texture with magnetite with trellis and sandwich-type lamellae Abundance:0.1% Alteration: unaltered mineral. **Chromite** Grain size: 0.01mm Observed within phenocrysts of pyroxenes and olivine Abundance:0.4% Alteration: unaltered mineral.

CAM-AC-2022-03		
Rock classification: wehrlite		
Silicates	**Sulfides**	**Oxides**
93% silicates **Clinopyroxene** Texture: Poikilitic. Pyroxene as oikocryst enclosing smaller olivine. Abundance: 25% Alteration: 5% to lizardite-chrysotile along the fractures. **Orthopyroxene** Grain size: 1.8mm Texture: Poikilitic Abundance: 1% Alteration: 5% to lizardite-chrysotile along the fractures. **Olivine** Grain size: 2mm Texture: Poikilitic- mesh-bastite Abundance: 55% Alteration: 70% to lizardite-chrysotile-magnetite with concentric growth in fractures. **Plagioclase** **Anorthite** Grain size: 2mm Texture: polysynthetic twinning Abundance: 12%. Occurring interstitially in pyroxene and olivine Alteration: 10% to epidote.	**5% sulfides** **Pyrrhotite** Grain size:0.9mm Texture: pentlandite flames "exsolution texture." Filling interstices of silicates. Abundance: 3% Alteration: 5% to magnetite along fractures. **Chalcopyrite** Grain size: 0.5mm Texture: subhedral, filling interstices of silicates Abundance: 2% Alteration: 5% to magnetite along fractures. **Pentlandite** Grain size: 0.01mm Texture: subhedral filling interstices of silicates Abundance: 1% Alteration: 5% to magnetite.	**2% oxides** **Magnetite** Grain size: 0.5mm Texture: exsolution texture with ilmenite Abundance: 1.4% Alteration: unaltered mineral **Ilmenite** Grain size: 0.1mm Texture: exsolution texture with magnetite Abundance:0.1% Alteration: unaltered mineral. **Chromite** Grain size: 0.01mm Observed within phenocrysts of pyroxenes and olivine Abundance:0.5% Alteration: unaltered mineral.
Comment: The 0.8 mm biotite presents a 60% alteration to chlorite on the boundaries; therefore, it could not be classified as primary or secondary silicate.		

CAM-AC-2022-05		
Rock classification: wehrlite		
Silicates	**Sulfides**	**Oxides**
92% silicates **Clinopyroxene** Grain size: 1.5mm Texture: Poikilitic. Pyroxene as oikocryst enclosing smaller olivine. Abundance: 27% Alteration: 15% to lizardite-chrysotile along the fractures. **Orthopyroxene** Grain size: 1.5mm Texture: Poikilitic Abundance: 3% Alteration: 15% to lizardite-chrysotile along the fractures. **Olivine** Grain size: 0.9mm Texture: Poikilitic- mesh-bastite Abundance: 54% Alteration: 90% to lizardite-chrysotile-magnetite with concentric growth in fractures and boundaries. **Plagioclase** **Anorthite** Grain size: 2.5mm Texture: polysynthetic twinning Abundance: 10%. Occurring interstitially in pyroxene and olivine Alteration: 25% to epidote and sericite.	**7% sulfides** **Pyrrhotite** Grain size:0.8mm Texture: pentlandite flames "exsolution texture." Filling interstices of silicates. Abundance: 3% Alteration: 7% to magnetite along fractures. **Chalcopyrite** Grain size: 0.8mm Texture: subhedral, filling interstices of silicates Abundance: 3% Alteration: 5% to magnetite along fractures. **Pentlandite** Grain size: 0.01mm Texture: subhedral filling interstices of silicates Abundance: 1% Alteration: 5% to magnetite.	**1% oxides** **Magnetite** Grain size: 0.4mm Abundance: 0.5% Alteration: unaltered mineral **Chromite** Grain size: 0.01mm Observed within phenocrysts of pyroxenes and olivine Abundance:0.5% Alteration: unaltered mineral.

CAM-AC-2022-06		
Rock classification: wehrlite		
Silicates	**Sulfides**	**Oxides**
90% silicates **Clinopyroxene** Grain size: 1.4mm Texture: Poikilitic. Pyroxene as oikocryst enclosing smaller olivine. Abundance: 22% Alteration: 15% to lizardite-chrysotile along the fractures. **Orthopyroxene** Grain size: 1.5mm Texture: Poikilitic Abundance: 2% Alteration: 15% to lizardite-chrysotile along the fractures. **Olivine** Grain size: 1.3mm Texture: Poikilitic- mesh-bastite Abundance: 60% Alteration: 80% to lizardite-chrysotile-magnetite with concentric growth in fractures and boundaries. **Plagioclase** **Anorthite** Grain size: 2.2mm Texture: polysynthetic twinning Abundance: 6%. Occurring interstitially in pyroxene and olivine Alteration: 20% to epidote and sericite.	**9% sulfides** **Pyrrhotite** Grain size:1.1mm Texture: pentlandite flames "exsolution texture." Filling interstices of silicates. Abundance: 5% Alteration: 10% to magnetite along fractures. **Chalcopyrite** Grain size: 0.6mm Texture: subhedral, filling interstices of silicates Abundance: 4% Alteration: 15% to magnetite along fractures. **Pentlandite** Grain size: 0.01mm Texture: subhedral filling interstices of silicates Abundance: 1% Alteration: 10% to magnetite.	**1% oxides** **Magnetite** Grain size: 0.4mm Texture: exsolution texture with ilmenite Abundance: 0.4% Alteration: unaltered mineral **Ilmenite** Grain size: 0.1mm Texture: exsolution texture with magnetite with trellis and sandwich-type lamellae Abundance:0.2% Alteration: unaltered mineral. **Chromite** Grain size: 0.01mm Observed within phenocrysts of pyroxenes and olivine Abundance:0.4% Alteration: unaltered mineral.
Comment: The 0.5 mm biotite presents a 40% alteration to chlorite on the boundaries; therefore, it could not be classified as primary or secondary silicate.		

CAM-AC-2022-07		
Rock classification: wehrlite		
Silicates	**Sulfides**	**Oxides**
92% silicates **Clinopyroxene** Grain size: 1.8mm Texture: Poikilitic. Pyroxene as oikocryst enclosing smaller olivine. Abundance: 25% Alteration: 5% to lizardite-chrysotile along the fractures. **Orthopyroxene** Grain size: 1.5mm Texture: Poikilitic Abundance: 2% Alteration: 5% to lizardite-chrysotile along the fractures. **Olivine** Grain size: 0.5mm Texture: Poikilitic- mesh-bastite Abundance: 58% Alteration: 70% to lizardite-chrysotile-magnetite with concentric growth in fractures and boundaries. **Plagioclase** **Anorthite** Grain size: 2.1mm Texture: polysynthetic twinning Abundance: 7%. Occurring interstitially in pyroxene and olivine Alteration: 15% to epidote and chlorite.	**7% sulfides** **Pyrrhotite** Grain size:1.1mm Texture: pentlandite flames "exsolution texture." Filling interstices of silicates. Abundance: 5% Alteration: unaltered. **Chalcopyrite** Grain size: 0.6mm Texture: subhedral, filling interstices of silicates Abundance: 3% Alteration: unaltered. **Pentlandite** Grain size: 0.01mm Texture: subhedral filling interstices of silicates Abundance: 1% Alteration: unaltered.	**1% oxides** **Magnetite** Grain size: 0.4mm Texture: exsolution texture with ilmenite Abundance: 0.5% Alteration: unaltered mineral **Ilmenite** Grain size: 0.01mm Texture: exsolution texture with magnetite. Abundance:0.1% Alteration: unaltered mineral. **Chromite** Grain size: 0.01mm Observed within phenocrysts of pyroxenes and olivine Abundance:0.4% Alteration: unaltered mineral.
Comment: The 1 mm biotite presents a 70% alteration to chlorite on the boundaries; therefore, it could not be classified as primary or secondary silicate.		

CAM-AC-2022-09		
Rock classification: wehrlite		
Silicates	**Sulfides**	**Oxides**
93% silicates **Clinopyroxene** Grain size: 2mm Texture: Poikilitic. Pyroxene as oikocryst enclosing smaller olivine. Abundance: 19% Alteration: 8% to lizardite-chrysotile along the fractures. **Orthopyroxene** Grain size: 1.8mm Texture: Poikilitic Abundance: 1% Alteration: 8% to lizardite-chrysotile along the fractures. **Olivine** Grain size: 2mm Texture: Poikilitic- mesh-bastite Abundance: 68% Alteration: 70% to lizardite-chrysotile-talc-magnetite-carbonates with concentric growth in fractures and boundaries. **Plagioclase** **Anorthite** Grain size: 2mm Texture: polysynthetic twinning Abundance: 5%. Occurring interstitially in pyroxene and olivine Alteration: 5% to epidote and sericite.	**5% sulfides** **Pyrrhotite** Grain size:0.9mm Texture: pentlandite flames "exsolution texture." Filling interstices of silicates. Abundance: 1.5% Alteration: 10% to magnetite along fractures. **Chalcopyrite** Grain size: 0.5mm Texture: subhedral, filling interstices of silicates Abundance: 3% Alteration: 10% to magnetite along fractures. **Pentlandite** Grain size: 0.1mm Texture: subhedral filling interstices of silicates Abundance: 0.5% Alteration: 10% to magnetite.	**2% oxides** **Magnetite** Grain size: 0.4mm Abundance: 1.5% Alteration: unaltered mineral **Chromite** Grain size: 0.01mm Observed within phenocrysts of pyroxenes and olivine Abundance:0.5% Alteration: unaltered mineral.

CAM-AC-2022-12		
Rock classification: wehrlite		
Silicates	**Sulfides**	**Oxides**
89% silicates **Clinopyroxene** Grain size: 1mm Texture: Poikilitic. Pyroxene as oikocryst enclosing smaller olivine. Abundance: 8% Alteration: 20% to actinolite-tremolite along the fractures. **Orthopyroxene** Grain size: 0.9mm Texture: Poikilitic Abundance: 1% Alteration: 20% to actinolite-tremolite along the fractures. **Olivine** Grain size: 0.5mm Texture: Poikilitic- mesh-bastite Abundance: 75% Alteration: 70% to antigorite-talc-magnetite-carbonates with concentric growth in fractures and boundaries. **Plagioclase** **Anorthite** Grain size: 1.5mm Texture: polysynthetic twinning Abundance: 5%. Occurring interstitially in pyroxene and olivine Alteration: 5% to epidote	**9% sulfides** **Pyrrhotite** Grain size:0.9mm Texture: pentlandite flames "exsolution texture." Filling interstices of silicates. Abundance: 3% Alteration: unaltered. **Chalcopyrite** Grain size: 0.5mm Texture: subhedral, filling interstices of silicates Abundance: 5% Alteration: unaltered. **Pentlandite** Grain size: 0.1mm Texture: subhedral filling interstices of silicates Abundance: 1% Alteration: unaltered.	**2% oxides** **Magnetite** Grain size: 0.4mm Texture: exsolution texture with ilmenite Abundance: 1.4% Alteration: unaltered mineral **Ilmenite** Grain size: 0.1mm Texture: exsolution texture with magnetite with trellis type lamellae Abundance:0.1% Alteration: unaltered mineral. **Chromite** Grain size: 0.01mm Observed within phenocrysts of pyroxenes and olivine Abundance:0.5% Alteration: unaltered mineral.

CAM-AC-2022-15		
Rock classification: lherzolite		
Silicates	**Sulfides**	**Oxides**
95% silicates **Clinopyroxene** Grain size: 0.8mm Texture: Poikilitic. Pyroxene as oikocryst enclosing smaller olivine. Abundance: 25% Alteration: 7% to lizardite-chrysotile. along the fractures. **Orthopyroxene** Grain size: 0.9mm Texture: Poikilitic Abundance: 12% Alteration: 7% to lizardite-chrysotile along the fractures. **Olivine** Grain size: 0.5mm Texture: Poikilitic- mesh-bastite Abundance: 50% Alteration: 70% to antigorite-magnetite ± lizardite-chrysotile with concentric growth in fractures and boundaries. **Plagioclase** **Anorthite** Grain size: 1.5mm Texture: polysynthetic twinning Abundance: 8%. Occurring interstitially in pyroxene and olivine Alteration: 6% to epidote	**4% sulfides** **Pyrrhotite** Grain size:1mm Texture: pentlandite flames "exsolution texture." Filling interstices of silicates. Abundance: 0.9% Alteration: 5% by magnetite. **Chalcopyrite** Grain size: 1mm Texture: subhedral, filling interstices of silicates Abundance: 3% Alteration: 5% by magnetite. **Pentlandite** Grain size: 0.1mm Texture: subhedral filling interstices of silicates Abundance: 0.1% Alteration: 50% by millerite.	**1% oxides** **Magnetite** Grain size: 0.4mm Texture: exsolution texture with ilmenite Abundance: 0.5% Alteration: unaltered mineral **Ilmenite** Grain size: 0.01mm Texture: exsolution texture with magnetite. Abundance:0.1% Alteration: unaltered mineral. **Chromite** Grain size: 0.01mm Observed within phenocrysts of pyroxenes and olivine Abundance:0.4% Alteration: unaltered mineral.

CAM-AC-2022-16		
Rock classification: lherzolite		
Silicates	**Sulfides**	**Oxides**
96% silicates **Clinopyroxene** Grain size: 1mm Texture: Poikilitic. Pyroxene as oikocryst enclosing smaller olivine. Abundance: 25% Alteration: 7% to lizardite-chrysotile along the fractures. **Orthopyroxene** Grain size: 1.5mm Texture: Poikilitic Abundance: 13% Alteration: 7% to lizardite-chrysotile along the fractures. **Olivine** Grain size: 0.6mm Texture: Poikilitic- mesh-bastite Abundance: 50% Alteration: 95% to magnetite- lizardite-chrysotile with concentric growth in fractures and boundaries. **Plagioclase** **Anorthite** Grain size: 1.4mm Texture: polysynthetic twinning Abundance: 8%. Occurring interstitially in pyroxene and olivine Alteration: 80% to chlorite	**3% sulfides** **Pyrrhotite** Grain size:0.7mm Texture: pentlandite flames "exsolution texture." Filling interstices of silicates. Abundance: 1% Alteration: 30% by pyrite-magnetite. **Chalcopyrite** Grain size: 0.8mm Texture: subhedral, filling interstices of silicates Abundance: 1.5% Alteration: 5% by magnetite. **Pentlandite** Grain size: 0.1mm Texture: subhedral filling interstices of silicates Abundance: 0.1% Alteration: 50% by millerite. **Secondary pyrrhotite** Grain size: 0.8mm Aggregates of pyrrhotite replacing secondary pyrite Abundance: 0.4%	**1% oxides** **Magnetite** Grain size: 0.4mm Texture: exsolution texture with ilmenite Abundance: 0.9% Alteration: unaltered mineral **Ilmenite** Grain size: 0.01mm Texture: exsolution texture with magnetite with trellis and sandwich-type lamellae Abundance:0.1% Alteration: unaltered mineral.

CAM-AC-2022-20		
Rock classification: wehrlite		
Silicates	**Sulfides**	**Oxides**
93% silicates **Clinopyroxene** Grain size: 1.5mm Texture: Poikilitic. Pyroxene as oikocryst enclosing smaller olivine. Abundance: 25% Alteration: 20% to lizardite-chrysotile along the fractures. **Olivine** Grain size: 1mm Texture: Poikilitic- mesh-bastite Abundance: 55% Alteration: 95% to lizardite-chrysotile-magnetite with concentric growth in fractures. **Plagioclase** **Anorthite** Grain size: 2mm Texture: polysynthetic twinning Abundance: 11%. Occurring interstitially in pyroxene and olivine Alteration: 80% to chlorite.	**5% sulfides** **Pyrrhotite** Grain size:0.9mm Texture: pentlandite flames "exsolution texture." Filling interstices of silicates. Abundance: 1.4% Alteration: 5% to pyrite-magnetite. **Chalcopyrite** Grain size: 0.5mm Texture: subhedral, filling interstices of silicates Abundance: 3% Alteration: 15% to cubanite. **Pentlandite** Grain size: 0.01mm Texture: subhedral filling interstices of silicates Abundance: 1% Alteration: 50% to millerite. **Secondary pyrrhotite** Grain size: 0.8mm Aggregates of pyrrhotite replacing secondary pyrite Abundance: 0.5%	**2% oxides** **Magnetite** Grain size: 0.4mm Texture: exsolution texture with ilmenite Abundance: 1.9% Alteration: unaltered mineral **Ilmenite** Grain size: 0.01mm Texture: exsolution texture with magnetite. Abundance:0.1% Alteration: unaltered mineral.
Comment: The 0.8 mm biotite presents a 60% alteration to chlorite on the boundaries; therefore, it could not be classified as primary or secondary silicate.		

CAM-AC-2022-24		
Rock classification: wehrlite		
Silicates	**Sulfides**	**Oxides**
95% silicates **Clinopyroxene** Grain size: 1mm Texture: Poikilitic. Pyroxene as oikocryst enclosing smaller olivine. Abundance: 23% Alteration: 15% to lizardite-chrysotile along the fractures. **Orthopyroxene** Grain size: 1mm Texture: Poikilitic Abundance: 1% Alteration: 15% to lizardite-chrysotile along the fractures. **Olivine** Grain size: 0.5mm Texture: Poikilitic- mesh-bastite Abundance: 65% Alteration: 80% to lizardite-chrysotile-magnetite with concentric growth in fractures. **Plagioclase** **Anorthite** Grain size: 1.5mm Texture: polysynthetic twinning Abundance: 7%. Occurring interstitially in pyroxene and olivine Alteration: 30% to epidote-sericite.	**4% sulfides** **Pyrrhotite** Grain size:0.9mm Texture: pentlandite flames "exsolution texture." Filling interstices of silicates. Abundance: 2.5% Alteration: 5% to pyrite-magnetite. **Chalcopyrite** Grain size: 0.5mm Texture: subhedral, filling interstices of silicates. Abundance: 1% Alteration: 15% to magnetite. **Pentlandite** Grain size: 0.01mm Texture: subhedral filling interstices of silicates Abundance: 0.5% Alteration: 10% to magnetite.	**1% oxides** **Magnetite** Grain size: 0.4mm Texture: exsolution texture with ilmenite Abundance: 0.5% Alteration: unaltered mineral **Ilmenite** Grain size: 0.1mm Texture: exsolution texture with magnetite. Abundance:0.1% Alteration: unaltered mineral. **Chromite** Grain size: 0.01mm Observed within phenocrysts of pyroxenes and olivine Abundance:0.4% Alteration: unaltered mineral.

CAM-AC-2022-28		
Rock classification: wehrlite		
Silicates	**Sulfides**	**Oxides**
96% silicates **Clinopyroxene** Grain size: 1.5mm Texture: Poikilitic. Pyroxene as oikocryst enclosing smaller olivine. Abundance: 10% Alteration: 8% to lizardite-chrysotile along the fractures. **Orthopyroxene** Grain size: 1.5mm Texture: Poikilitic Abundance: 3% Alteration: 8% to lizardite-chrysotile along the fractures. **Olivine** Grain size: 0.9mm Texture: Poikilitic- mesh-bastite Abundance: 77% Alteration: 98% to lizardite-chrysotile-magnetite-carbonates **Plagioclase** **Anorthite** Grain size: 2mm Texture: polysynthetic twinning Abundance: 10%. Occurring interstitially in pyroxene and olivine Alteration: 80% to sericite-epidote-	**3% sulfides** **Pyrrhotite** Grain size:0.8mm Texture: pentlandite flames "exsolution texture." Filling interstices of silicates. Abundance: 2% Alteration: 100% pyrite. **Chalcopyrite** Grain size: 0.8mm Texture: subhedral, filling interstices of silicates Abundance: 0.5% Alteration: 5% to magnetite along fractures. **Secondary pyrrhotite** Grain size: 0.8mm Aggregates of pyrrhotite replacing secondary pyrite Abundance: 0.5%	**1% oxides** **Magnetite** Grain size: 0.4mm Abundance: 0.9% Alteration: unaltered mineral **Chromite** Grain size: 0.01mm Observed within phenocrysts of pyroxenes and olivine Abundance:0.1% Alteration: unaltered mineral.

CAM-AC-2022-31		
Rock classification: wehrlite		
Silicates	**Sulfides**	**Oxides**
93% silicates **Clinopyroxene** Grain size: 1.4mm Texture: Poikilitic. Pyroxene as oikocryst enclosing smaller olivine. Abundance: 9% Alteration: 8% to lizardite-chrysotile along the fractures. **Orthopyroxene** Grain size: 1.4mm Texture: Poikilitic Abundance: 3% Alteration: 8% to lizardite-chrysotile along the fractures. **Olivine** Grain size: 0.7mm Texture: Poikilitic- mesh-bastite Abundance: 71% Alteration: 60% to lizardite-chrysotile-magnetite **Plagioclase** **Anorthite** Grain size: 1.8mm Texture: polysynthetic twinning Abundance: 10%. Occurring interstitially in pyroxene and olivine Alteration: 5% to sericite	**6% sulfides** **Pyrrhotite** Grain size:0.7mm Texture: pentlandite flames "exsolution texture." Filling interstices of silicates. Abundance: 2.8% Alteration: 10% magnetite. **Chalcopyrite** Grain size: 0.7mm Texture: subhedral, filling interstices of silicates Abundance: 4% Alteration: 5% to cubanite. **Pentlandite** Grain size: 0.01mm Texture: subhedral filling interstices of silicates Abundance: 0.2% Alteration: 10% to magnetite.	**1% oxides** **Magnetite** Grain size: 0.3mm Texture: exsolution texture with ilmenite Abundance: 0.5% Alteration: unaltered mineral **Ilmenite** Grain size: 0.1mm Texture: exsolution texture with magnetite with trellis and sandwich-type lamellae Abundance:0.1% Alteration: unaltered mineral. **Chromite** Grain size: 0.01mm Observed within phenocrysts of pyroxenes and olivine Abundance:0.4% Alteration: unaltered mineral.

CAM-AC-2022-33		
Rock classification: wehrlite		
Silicates	**Sulfides**	**Oxides**
93% silicates **Clinopyroxene** Grain size: 2mm Texture: Poikilitic. Pyroxene as oikocryst enclosing smaller olivine. Abundance: 7% Alteration: 8% to antigorite along the fractures. **Orthopyroxene** Grain size: 1.8mm Texture: Poikilitic Abundance: 1% Alteration: 8% to antigorite along the fractures. **Olivine** Grain size: 1.1mm Texture: Poikilitic- mesh-bastite Abundance: 80% Alteration: 70% antigorite-magnetite with concentric growth in fractures and boundaries. **Plagioclase** **Anorthite** Grain size: 1.8mm Texture: polysynthetic twinning Abundance: 5%. Occurring interstitially in pyroxene and olivine Alteration: 4% to sericite and chlorite	**5% sulfides** **Pyrrhotite** Grain size:0.9mm Texture: pentlandite flames "exsolution texture." Filling interstices of silicates. Abundance: 3% Alteration: 5% to magnetite along fractures. **Chalcopyrite** Grain size: 0.5mm Texture: subhedral, filling interstices of silicates Abundance: 1.5% Alteration: 5% to cubanite. **Pentlandite** Grain size: 0.1mm Texture: subhedral filling interstices of silicates Abundance: 0.5% Alteration: 5% to magnetite.	**2% oxides** **Magnetite** Grain size: 0.4mm Texture: exsolution texture with ilmenite Abundance: 1.9% Alteration: unaltered mineral **Ilmenite** Grain size: 0.1mm Texture: exsolution texture with magnetite. Abundance:0.1% Alteration: unaltered mineral.

CAM-AC-2022-34		
Rock classification: wehrlite		
Silicates	**Sulfides**	**Oxides**
90% silicates **Clinopyroxene** Grain size: 2mm Texture: Poikilitic. Pyroxene as oikocryst enclosing smaller olivine. Abundance: 9% Alteration: 25% to actinolite-tremolite. **Orthopyroxene** Grain size: 1.5mm Texture: Poikilitic Abundance: 3% Alteration: 25% to actinolite-tremolite. **Olivine** Grain size: 0.5mm Texture: Poikilitic- mesh-bastite Abundance: 60% Alteration: 90% to antigorite. Antigorite altered posteriorly to talc. **Plagioclase** **Anorthite** Grain size: 1.3mm Texture: polysynthetic twinning Abundance: 7%. Occurring interstitially in pyroxene and olivine Alteration: 30% to sericite- chlorite.	**8% sulfides** **Pyrrhotite** Grain size:1.1mm Filling interstices of silicates. Abundance: 5% Alteration: unaltered mineral. **Chalcopyrite** Grain size: 0.6mm Texture: subhedral, filling interstices of silicates Abundance: 3% Alteration: 10% to pyrite.	**2% oxides** **Magnetite** Grain size: 0.4mm Texture: exsolution texture with ilmenite Abundance: 1.8% Alteration: unaltered mineral **Ilmenite** Grain size: 0.1mm Texture: exsolution texture with magnetite with trellis and sandwich-type lamellae Abundance:0.1% Alteration: unaltered mineral. **Chromite** Grain size: 0.01mm Observed within phenocrysts of pyroxenes and olivine Abundance:0.1% Alteration: unaltered mineral.
Comment: late carbonate veins cutting the previous alterations (antigorite). Talc alters antigorite.		

CAM-AC-2022-35		
Rock classification: olivine gabbronorite		
Silicates	**Sulfides**	**Oxides**
94% silicates **Clinopyroxene** Grain size: 1mm Texture: Poikilitic. Pyroxene as oikocryst enclosing smaller olivine. Abundance: 6% Alteration: 100% to lizardite-chrysotile along the fractures. **Olivine** Grain size: 0.6mm Texture: Poikilitic- mesh-bastite Abundance: 44% Alteration: 100% to magnetite-lizardite-chrysotile with concentric growth in fractures and boundaries. **Plagioclase** **Labradorite** Grain size: 1.4mm Texture: carlsbad twinning Abundance: 44%. Occurring interstitially in pyroxene and olivine Alteration: 100% to epidote	**5% sulfides** **Secondary pyrite** Grain size:0.7mm Texture: replacement texture. Pyrrhotite has been completely replaced by pyrite. Abundance: 5%	**1% oxides** **Magnetite** Grain size: 0.4mm Abundance: 0.5% Texture: exsolution texture with magnetite. Alteration: 100% altered to chlorite **Ilmenite** Grain size: 0.4mm Texture: exsolution texture with magnetite with trellis and sandwich-type lamellae. Abundance:0.1% Alteration: unaltered mineral. **Chromite** Grain size: 0.01mm Observed within phenocrysts of pyroxenes and olivine Abundance:0.1% Alteration: unaltered mineral.

CAM-AC-2022-36		
Rock classification: olivine gabbronorite		
Silicates	**Sulfides**	**Oxides**
91% silicates **Clinopyroxene** Grain size: 0.9mm Texture: Poikilitic. Pyroxene as oikocryst enclosing smaller olivine. Abundance: 4% Alteration: 60% to antigorite along the fractures. Antigorite altered posteriorly to talc. **Olivine** Grain size: 0.5mm Texture: Poikilitic- mesh-bastite Abundance: 43% Alteration: 100% to antigorite-magnetite with concentric growth in fractures and boundaries. Antigorite altered posteriorly to talc. **Plagioclase** **Labradorite** Grain size: 1mm Texture: Carlsbad twinning Abundance: 44%. Occurring interstitially in pyroxene and olivine Alteration: 60% to chlorite	**8% sulfides** **Pyrrhotite** Grain size:0.5mm Filling interstices of silicates. Abundance: 6% Alteration:30% by pyrite. **Secondary pyrrhotite** Grain size: 0.4mm Aggregates of pyrrhotite replacing secondary pyrite Abundance: 2%	**1% oxides** **Magnetite** Grain size: 0.3mm Abundance: 0.5% Texture: exsolution texture with magnetite with trellis and sandwich-type lamellae. Alteration: 100% altered to chlorite **Ilmenite** Grain size: 0.4mm Texture: exsolution texture with magnetite. Abundance:0.4% Alteration: unaltered mineral. **Chromite** Grain size: 0.01mm Observed within phenocrysts of pyroxenes and olivine Abundance:0.1% Alteration: unaltered mineral.
Comment: late carbonate veins cutting the previous alterations (antigorite). Talc alters antigorite.		

CAM-AC-2022-37		
Rock classification: wehrlite		
Silicates	**Sulfides**	**Oxides**
92% silicates **Clinopyroxene** Grain size: 1.5mm Texture: Poikilitic. Pyroxene as oikocryst enclosing smaller olivine. Abundance: 11% Alteration: 5% to Antigorite-lizardite-chrysotile along the fractures. **Orthopyroxene** Grain size: 1.5mm Texture: Poikilitic Abundance: 2% Alteration: 5% to antigorite-lizardite-chrysotile along the fractures. **Olivine** Grain size: 0.5mm Texture: Poikilitic- mesh-bastite Abundance: 72% Alteration: 30% to antigorite-lizardite-chrysotile-magnetite with concentric growth in fractures and boundaries. **Plagioclase** **Anorthite** Grain size: 2mm Texture: polysynthetic twinning Abundance: 7%. Occurring interstitially in pyroxene and olivine Alteration: 20% to chlorite.	**7% sulfides** **Pyrrhotite** Grain size:1.1mm Texture: pentlandite flames "exsolution texture." Filling interstices of silicates. Abundance: 4.9% Alteration: 2% to magnetite. **Chalcopyrite** Grain size: 0.6mm Texture: subhedral, filling interstices of silicates Abundance: 2% Alteration: 3% to cubanite. **Pentlandite** Grain size: 0.01mm Texture: subhedral filling interstices of silicates Abundance: 0.1% Alteration: unaltered.	**1% oxides** **Magnetite** Grain size: 0.4mm Texture: exsolution texture with ilmenite Abundance: 0.9% Alteration: unaltered mineral **Ilmenite** Grain size: 0.01mm Texture: exsolution texture with magnetite. Abundance:0.1% Alteration: unaltered mineral. **Chromite** Grain size: 0.01mm Observed within phenocrysts of pyroxenes and olivine Abundance:0.1% Alteration: unaltered mineral.

CAM-AC-2022-38		
Rock classification: lherzolite		
Silicates	**Sulfides**	**Oxides**
93% silicates **Clinopyroxene** Grain size: 1.5mm Texture: Poikilitic. Pyroxene as oikocryst enclosing smaller olivine. Abundance: 10% Alteration: 5% to antigorite-lizardite-chrysotile **Orthopyroxene** Grain size: 1.8mm Texture: Poikilitic Abundance: 1% Alteration: 5% to antigorite-lizardite-chrysotile **Olivine** Grain size: 1.9mm Texture: Poikilitic- mesh-bastite Abundance: 80% Alteration: 30% to antigorite-lizardite-chrysotile-magnetite **Plagioclase** **Anorthite** Grain size: 2mm Texture: polysynthetic twinning Abundance: 2%. Occurring interstitially in pyroxene and olivine Alteration: 30% to chlorite-sericite.	**5% sulfides** **Pyrrhotite** Grain size:0.9mm Texture: pentlandite flames "exsolution texture." Filling interstices of silicates. Abundance: 3% Alteration: unaltered. **Chalcopyrite** Grain size: 0.5mm Texture: subhedral, filling interstices of silicates Abundance: 2% Alteration: unaltered. **Pentlandite** Grain size: 0.01mm Texture: subhedral filling interstices of silicates Abundance: 1% Alteration: unaltered.	**2% oxides** **Magnetite** Grain size: 0.2mm Abundance: 1.5% Alteration: unaltered mineral **Chromite** Grain size: 0.01mm Observed within phenocrysts of pyroxenes and olivine. Abundance: 0.5% Alteration: unaltered mineral.
Comment: late carbonate veins cutting the previous alterations (antigorite-lizardite-chrysotile). Talc alters antigorite.		

CAM-AC-2022-41		
Rock classification: wehrlite		
Silicates	**Sulfides**	**Oxides**
94% silicates **Clinopyroxene** Grain size: 1.5mm Texture: Poikilitic. Pyroxene as oikocryst enclosing smaller olivine. Abundance: 22% Alteration: 15% to Antigorite-lizardite-chrysotile **Olivine** Grain size: 1mm Texture: Poikilitic- mesh-bastite Abundance: 64% Alteration: 15% to Antigorite-lizardite-chrysotile. Talc replacing Antigorite-lizardite-chrysotile. **Plagioclase** **Anorthite** Grain size: 1.6mm Texture: polysynthetic twinning Abundance: 8%. Occurring interstitially in pyroxene and olivine Alteration: 100% to epidote, sericite and chlorite.	**5% sulfides** **Secondary pyrite** Grain size:0.5mm Texture: replacement texture. Pyrrhotite has been completely replaced by pyrite.	**1% oxides** **Magnetite** Grain size: 0.3mm Abundance: 0.8% Alteration: unaltered mineral **Chromite** Grain size: 0.01mm Observed within phenocrysts of pyroxenes and olivine. Abundance: 0.2% Alteration: unaltered mineral.
Comment: late carbonate- talc cutting the previous alterations (antigorite-lizardite-chrysotile). Talc alters antigorite.		

CAM-AC-2022-50		
Rock classification: wehrlite		
Silicates	**Sulfides**	**Oxides**
98% silicates **Clinopyroxene** Grain size: 1.2mm Texture: Poikilitic. Pyroxene as oikocryst enclosing smaller olivine. Abundance: 15% Alteration: 4% Antigorite-lizardite-chrysotile **Orthopyroxene** Grain size: 1.2mm Texture: Poikilitic Abundance: 2% Alteration: 4% Antigorite-lizardite-chrysotile **Olivine** Grain size: 1mm Texture: Poikilitic- mesh-bastite Abundance: 75% Alteration: 10% to Antigorite-lizardite-chrysotile **Plagioclase** **Anorthite** Grain size: 1.8mm Texture: polysynthetic twinning Abundance: 10%. Occurring interstitially in pyroxene and olivine Alteration: 20% to epidote and sericite.	**1% sulfides** **Pyrrhotite** Grain size:0.3mm Filling interstices of silicates. Abundance: 1% Alteration: unaltered.	**1% oxides** **Magnetite** Grain size: 0.4mm Abundance: 0.8% Alteration: unaltered mineral **Ilmenite** Grain size: 0.1mm Texture: exsolution texture with magnetite with trellis and sandwich-type lamellae Abundance:0.2% Alteration: unaltered mineral.

CAM-AC-2022-52		
Rock classification: lherzolite		
Silicates	**Sulfides**	**Oxides**
97% silicates **Clinopyroxene** Grain size: 1.8mm Texture: Poikilitic. Pyroxene as oikocryst enclosing smaller olivine. Abundance: 13% Alteration: 5% to lizardite-chrysotile along the fractures. **Orthopyroxene** Grain size: 1.5mm Texture: Poikilitic Abundance: 5% Alteration: 5% to lizardite-chrysotile along the fractures. **Olivine** Grain size: 0.5mm Texture: Poikilitic- mesh-bastite Abundance: 75% Alteration: 70% to lizardite-chrysotile-magnetite with concentric growth in fractures and boundaries. **Plagioclase** **Anorthite** Grain size: 2.1mm Texture: polysynthetic twinning Abundance: 5%. Occurring interstitially in pyroxene and olivine Alteration: 15% to chlorite.	**2% sulfides** **Pyrrhotite** Grain size:1mm Texture: pentlandite flames "exsolution texture." Filling interstices of silicates. Abundance: 0.5% Alteration: 30% to magnetite **Chalcopyrite** Grain size: 0.4mm Texture: subhedral, filling interstices of silicates Abundance: 1% Alteration: 30% to magnetite **Pentlandite** Grain size: 0.01mm Texture: subhedral filling interstices of silicates Abundance: 0.5% Alteration: 30% to magnetite.	**1% oxides** **Magnetite** Grain size: 0.3mm Texture: exsolution texture with ilmenite Abundance: 0.8% Alteration: unaltered mineral **Ilmenite** Grain size: 0.01mm Texture: exsolution texture with magnetite. Abundance:0.1% Alteration: unaltered mineral. **Chromite** Grain size: 0.01mm Observed within phenocrysts of pyroxenes and olivine. Abundance: 0.1% Alteration: unaltered mineral.

CAM-AC-2022-56		
Rock classification: lherzolite		
Silicates	**Sulfides**	**Oxides**
93% silicates **Clinopyroxene** Grain size: 1.2mm Texture: Poikilitic. Pyroxene as oikocryst enclosing smaller olivine. Abundance: 10% Alteration: 5% to antigorite-lizardite-chrysotile **Orthopyroxene** Grain size: 1.3mm Texture: Poikilitic Abundance: 1% Alteration: 5% to antigorite-lizardite-chrysotile **Olivine** Grain size: 1mm Texture: Poikilitic- mesh-bastite Abundance: 75% Alteration: 10% to antigorite-lizardite-chrysotile-magnetite **Plagioclase** **Anorthite** Grain size: 2mm Texture: polysynthetic twinning Abundance: 7%. Occurring interstitially in pyroxene and olivine Alteration: 80% to chlorite-sericite.	**6% sulfides** **Pyrrhotite** Grain size:0.8mm Texture: pentlandite flames "exsolution texture." Filling interstices of silicates. Abundance: 4% Alteration: 5% to pyrite. **Chalcopyrite** Grain size: 0.5mm Texture: subhedral, filling interstices of silicates Abundance: 2% Alteration: unaltered. **Pentlandite** Grain size: 0.01mm Texture: subhedral filling interstices of silicates Abundance: 1% Alteration: 10% to magnetite.	**1% oxides** **Magnetite** Grain size: 0.2mm Abundance: 0.7% Alteration: unaltered mineral **Chromite** Grain size: 0.01mm Observed within phenocrysts of pyroxenes and olivine. Abundance: 0.3% Alteration: unaltered mineral.

CAM-AC-2022-61		
Rock classification: wehrlite		
Silicates	**Sulfides**	**Oxides**
88% silicates **Clinopyroxene** Grain size: 1.4mm Texture: Poikilitic. Pyroxene as oikocryst enclosing smaller olivine. Abundance: 15% Alteration: 10% to lizardite-chrysotile-antigorite along the fractures. **Orthopyroxene** Grain size: 1.5mm Texture: Poikilitic Abundance: 3% Alteration: 10% to lizardite-chrysotile-antigorite along the fractures. **Olivine** Grain size: 1mm Texture: Poikilitic- mesh-bastite Abundance: 60% Alteration: 15% to lizardite-chrysotile-antigorite-magnetite **Plagioclase** **Anorthite** Grain size: 2mm Texture: polysynthetic twinning Abundance: 10%. Occurring interstitially in pyroxene and olivine Alteration: 100% to chlorite.	**10% sulfides** **Pyrrhotite** Grain size:0.5mm Texture: pentlandite flames "exsolution texture." Filling interstices of silicates. Abundance: 6% Alteration: 40% to pyrite-magnetite. **Chalcopyrite** Grain size: 0.5mm Texture: subhedral, filling interstices of silicates Abundance: 3% Alteration: 2% to cubanite. **Pentlandite** Grain size: 0.01mm Texture: subhedral filling interstices of silicates Abundance: 1% Alteration: unaltered **Secondary pyrrhotite** Grain size: 0.4mm Aggregates of pyrrhotite replacing secondary pyrite Abundance: 1%	**2% oxides** **Magnetite** Grain size: 0.3mm Texture: exsolution texture with ilmenite Abundance: 1.9% Alteration: unaltered mineral **Ilmenite** Grain size: 0.1mm Texture: exsolution texture with magnetite. Abundance:0.1% Alteration: unaltered mineral.

CAM-AC-2022-64		
Rock classification: wehrlite		
Silicates	**Sulfides**	**Oxides**
92% silicates **Clinopyroxene** Grain size: 1.5mm Texture: Poikilitic. Pyroxene as oikocryst enclosing smaller olivine. Abundance: 27% Alteration: 8% to lizardite-chrysotile-antigorite. **Olivine** Grain size: 0.9mm Texture: Poikilitic- mesh-bastite Abundance: 55% Alteration: 20% to lizardite-chrysotile-antigorite. **Plagioclase** **Anorthite** Grain size: 2.5mm Texture: polysynthetic twinning Abundance: 10%. Occurring interstitially in pyroxene and olivine Alteration: 10% to sericite and chlorite	**7% sulfides** **Pyrrhotite** Grain size:0.5mm Filling interstices of silicates. Abundance: 4% Alteration: 20% to pyrite-magnetite. **Chalcopyrite** Grain size: 0.8mm Texture: subhedral, filling interstices of silicates Abundance: 2% Alteration: unaltered **Secondary pyrrhotite** Grain size: 0.4mm Aggregates of pyrrhotite replacing secondary pyrite Abundance: 1%	**1% oxides** **Magnetite** Grain size: 0.4mm Texture: exsolution texture with ilmenite Abundance: 0.8% Alteration: unaltered mineral **Ilmenite** Grain size: 0.1mm Texture: exsolution texture with magnetite with trellis and sandwich-type lamellae Abundance:0.1% Alteration: unaltered mineral. **Chromite** Grain size: 0.01mm Observed within phenocrysts of pyroxenes and olivine. Abundance: 0.1% Alteration: unaltered mineral.

CAM-AC-2022-67		
Rock classification: wehrlite		
Silicates	**Sulfides**	**Oxides**
93% silicates **Clinopyroxene** Grain size: 2.1mm Texture: Poikilitic. Pyroxene as oikocryst enclosing smaller olivine. Abundance: 25% Alteration: 25% antigorite along the fractures. **Orthopyroxene** Grain size: 1.8mm Texture: Poikilitic Abundance: 1% Alteration: 25% antigorite along the fractures. **Olivine** Grain size: 2mm Texture: Poikilitic- mesh-bastite Abundance: 55% Alteration: 40% to antigorite-magnetite with concentric growth in fractures. **Plagioclase** **Anorthite** Grain size: 2mm Texture: polysynthetic twinning Abundance: 12%. Occurring interstitially in pyroxene and olivine Alteration: 10% to sericite and chlorite.	**5% sulfides** **Pyrrhotite** Grain size:0.9mm Filling interstices of silicates. Abundance: 3.5% Alteration: 5% to pyrite. **Chalcopyrite** Grain size: 0.5mm Texture: subhedral, filling interstices of silicates Abundance: 1% Alteration: 5% to cubanite. **Secondary pyrrhotite** Grain size: 0.4mm Aggregates of pyrrhotite replacing secondary pyrite Abundance: 0.5%	**2% oxides** **Magnetite** Grain size: 0.4mm Texture: exsolution texture with ilmenite Abundance: 1.8% Alteration: unaltered mineral **Ilmenite** Grain size: 0.1mm Texture: exsolution texture with magnetite with trellis type lamellae Abundance:0.1% Alteration: unaltered mineral. **Chromite** Grain size: 0.01mm Observed within phenocrysts of pyroxenes and olivine. Abundance: 0.1% Alteration: unaltered mineral.
Comment: late carbonate veins cutting the previous alterations (antigorite). Talc alters antigorite.		

CAM-AC-2022-69		
Rock classification: troctolite		
Silicates	**Sulfides**	**Oxides**
93% silicates **Clinopyroxene** Grain size: 2mm Texture: Poikilitic. Pyroxene as oikocryst enclosing smaller olivine. Abundance: 3% Alteration: 5% to actinolite-tremolite. **Olivine** Grain size: 2mm Texture: Poikilitic- mesh-bastite Abundance: 45% Alteration: 100% to antigorite-magnetite- with concentric growth in fractures and boundaries. The antigorite is altered to talc. **Plagioclase** **Labradorite** Grain size: 1.4mm Texture: carlsbad twinning Abundance: 45%. Occurring interstitially in pyroxene and olivine Alteration: 40% to epidote and chlorite.	**5% sulfides** **Secondary pyrite** Grain size:0.5mm Texture: replacement texture. Pyrrhotite has been completely replaced by pyrite.	**2% oxides** **Magnetite** Grain size: 0.4mm Texture: exsolution texture with ilmenite Abundance: 1.9% Alteration: unaltered mineral **Chromite** Grain size: 0.01mm Observed within phenocrysts of pyroxenes and olivine. Abundance: 0.1% Alteration: unaltered mineral.

CAM-AC-2022-71		
Rock classification: lherzolite		
Silicates	**Sulfides**	**Oxides**
91% silicates **Clinopyroxene** Grain size: 1.8mm Texture: Poikilitic. Pyroxene as oikocryst enclosing smaller olivine. Abundance: 12% Alteration: 5% to actinolite-lizardite-chrysotile along the fractures. **Orthopyroxene** Grain size: 1.5mm Texture: Poikilitic Abundance: 5% Alteration: 5% to actinolite- lizardite-chrysotile along the fractures. **Olivine** Grain size: 0.5mm Texture: Poikilitic- mesh-bastite Abundance: 70% Alteration: 85% to actinolite-lizardite-chrysotile-magnetite. **Plagioclase** **Anorthite** Grain size: 2.1mm Texture: polysynthetic twinning Abundance: 5%. Occurring interstitially in pyroxene and olivine Alteration: 20% to chlorite.	**8% sulfides** **Pyrrhotite** Grain size:1mm Texture: pentlandite flames "exsolution texture." Filling interstices of silicates. Abundance: 3.5% Alteration: 30% to pyrite. **Chalcopyrite** Grain size: 0.4mm Texture: subhedral, filling interstices of silicates Abundance: 4% Alteration: 30% to cubanite **Pentlandite** Grain size: 0.01mm Texture: subhedral filling interstices of silicates Abundance: 0.5% Alteration: 30% to magnetite.	**1% oxides** **Magnetite** Grain size: 0.3mm Texture: exsolution texture with ilmenite Abundance: 0.8% Alteration: unaltered mineral **Ilmenite** Grain size: 0.01mm Texture: exsolution texture with magnetite. Abundance:0.1% Alteration: unaltered mineral. **Chromite** Grain size: 0.1mm Observed within phenocrysts of pyroxenes and olivine. Abundance: 0.01% Alteration: unaltered mineral.

CAM-AC-2022-77		
Rock classification: lherzolite		
Silicates	**Sulfides**	**Oxides**
96% silicates **Clinopyroxene** Grain size: 1.3mm Texture: Poikilitic. Pyroxene as oikocryst enclosing smaller olivine. Abundance: 13% Alteration: 5% to lizardite-chrysotile along the fractures. **Orthopyroxene** Grain size: 1.2mm Texture: Poikilitic Abundance: 4% Alteration: 5% to lizardite-chrysotile along the fractures. **Olivine** Grain size: 0.5mm Texture: Poikilitic- mesh-bastite Abundance: 75% Alteration: 40% to lizardite-chrysotile-magnetite with concentric growth in fractures and boundaries. **Plagioclase** **Anorthite** Grain size: 1.6mm Texture: polysynthetic twinning Abundance: 5%. Occurring interstitially in pyroxene and olivine Alteration: 40% to epidote-chlorite.	**3% sulfides** **Pyrrhotite** Grain size:0.9mm Texture: pentlandite flames "exsolution texture." Filling interstices of silicates. Abundance: 1.5% Alteration: 2% to magnetite **Chalcopyrite** Grain size: 0.7mm Texture: subhedral, filling interstices of silicates Abundance: 1% Alteration: 2% to magnetite **Pentlandite** Grain size: 0.01mm Texture: subhedral filling interstices of silicates Abundance: 0.5% Alteration: 2% to magnetite.	**1% oxides** **Magnetite** Grain size: 0.6mm Texture: exsolution texture with ilmenite Abundance: 0.8% Alteration: unaltered mineral **Ilmenite** Grain size: 0.01mm Texture: exsolution texture with magnetite. Abundance:0.1% Alteration: unaltered mineral. **Chromite** Grain size: 0.1mm Observed within phenocrysts of pyroxenes and olivine. Abundance: 0.01% Alteration: unaltered mineral.

CAM-AC-2022-82		
Rock classification: wehrlite		
Silicates	**Sulfides**	**Oxides**
90% silicates **Clinopyroxene** Grain size: 1.4mm Texture: Poikilitic. Pyroxene as oikocryst enclosing smaller olivine. Abundance: 20% Alteration: 7% to actinolite-tremolite along the fractures. **Orthopyroxene** Grain size: 1.5mm Texture: Poikilitic Abundance: 3% Alteration: 7% to actinolite-tremolite along the fractures. **Olivine** Grain size: 0.5mm Texture: Poikilitic- mesh-bastite Abundance: 60% Alteration: 95% to antigorite- lizardite-chrysotile-magnetite with concentric growth in fractures and boundaries. **Plagioclase** **Anorthite** Grain size: 1.3mm Texture: polysynthetic twinning Abundance: 7%. Occurring interstitially in pyroxene and olivine Alteration: 10% to epidote- sericite.	**8% sulfides** **Pyrrhotite** Grain size:1mm Texture: pentlandite flames "exsolution texture." Filling interstices of silicates. Abundance: 3% Alteration: 50% pyrite. **Chalcopyrite** Grain size: 0.6mm Texture: subhedral, filling interstices of silicates Abundance: 5% Alteration: 5% to magnetite along fractures. **Pentlandite** Grain size: 0.01mm Texture: subhedral filling interstices of silicates Abundance: 1% Alteration: 5% to magnetite-millerite.	**2% oxides** **Magnetite** Grain size: 0.4mm Abundance: 1.8% Alteration: unaltered mineral **Chromite** Grain size: 0.01mm Observed within phenocrysts of pyroxenes and olivine. Abundance: 0.2% Alteration: unaltered mineral.
Comment: late carbonate veins cutting the previous alterations (antigorite- lizardite-chrysotile). Talc alters antigorite.		

CAM-AC-2022-83		
Rock classification: wehrlite		
Silicates	**Sulfides**	**Oxides**
89% silicates **Clinopyroxene** Grain size: 1.3mm Texture: Poikilitic. Pyroxene as oikocryst enclosing smaller olivine. Abundance: 21% Alteration: 25% to actinolite-tremolite **Orthopyroxene** Grain size: 1.5mm Texture: Poikilitic Abundance: 1% Alteration: 25% to actinolite-tremolite. **Olivine** Grain size: 0.8mm Texture: Poikilitic- mesh-bastite Abundance: 55% Alteration: 100% to antigorite-magnetite with concentric growth in fractures. **Plagioclase** **Anorthite** Grain size: 2mm Texture: polysynthetic twinning Abundance: 12%. Occurring interstitially in pyroxene and olivine Alteration: 10% to chlorite-sericite.	**9% sulfides** **Pyrrhotite** Grain size:0.9mm Texture: pentlandite flames "exsolution texture." Filling interstices of silicates. Abundance: 1% Alteration: 30% to pyrite along fractures. **Chalcopyrite** Grain size: 0.5mm Texture: subhedral, filling interstices of silicates Abundance: 8% Alteration: 30% to cubanite.	**2% oxides** **Magnetite** Grain size: 0.3mm Texture: exsolution texture with ilmenite Abundance: 1.9% Alteration: unaltered mineral **Ilmenite** Grain size: 0.1mm Texture: exsolution texture with magnetite with trellis type lamellae Abundance:0.1% Alteration: unaltered mineral.
Comment: late carbonate veins cutting the previous alterations (antigorite). Talc alters antigorite.		

CAM-MB-2021-177		
Rock classification: olivine gabbronorite		
Silicates	**Sulfides**	**Oxides**
95% silicates **Clinopyroxene** Grain size: 0.8mm Texture: Poikilitic. Pyroxene as oikocryst enclosing smaller olivine. Abundance: 4% Alteration: 5% to actinolite-tremolite along the fractures. **Olivine** Grain size: 0.6mm Texture: Poikilitic- mesh-bastite Abundance: 43% Alteration: 100% to antigorite-magnetite with concentric growth in fractures and boundaries. Antigorite altered posteriorly to talc. **Plagioclase** **Labradorite** Grain size: 1.1mm Texture: Carlsbad twinning Abundance: 48%. Occurring interstitially in pyroxene and olivine Alteration: 100% to chlorite-sericite-epidote.	**4% sulfides** **Secondary pyrite** Grain size:0.8mm Texture: replacement texture. Pyrrhotite has been completely replaced by pyrite.	**1% oxides** **Magnetite** Grain size: 0.3mm Abundance: 0.5% Texture: exsolution texture with magnetite with trellis and sandwich-type lamellae. Alteration: 100% altered to chlorite **Ilmenite** Grain size: 0.1mm Texture: exsolution texture with magnetite. Abundance:0.4% Alteration: unaltered mineral. **Chromite** Grain size: 0.1mm Observed within phenocrysts of pyroxenes and olivine Abundance:0.01% Alteration: unaltered mineral.
Comment: late carbonate veins cutting the previous alterations (antigorite). Talc alters antigorite.		

CAM-MB-2021-171		
Rock classification: lherzolite		
Silicates	**Sulfides**	**Oxides**
91% silicates **Clinopyroxene** Grain size: 1.1mm Texture: Poikilitic. Pyroxene as oikocryst enclosing smaller olivine. Abundance: 20% Alteration: 15% to actinolite-tremolite along the fractures. **Orthopyroxene** Grain size: 1.5mm Texture: Poikilitic Abundance: 13% Alteration: 15% to actinolite-tremolite along the fractures. **Olivine** Grain size: 0.9mm Texture: Poikilitic- mesh-bastite Abundance: 50% Alteration: 15% to antigorite-lizardite-chrysotile-magnetite with concentric growth in fractures and boundaries. **Plagioclase** **Anorthite** Grain size: 1.4mm Texture: polysynthetic twinning Abundance: 8%. Occurring interstitially in pyroxene and olivine Alteration: 100% to chlorite	**8% sulfides** **Pyrrhotite** Grain size:0.8mm Filling interstices of silicates. Abundance: 6% Alteration: 30% by pyrite-magnetite. **Chalcopyrite** Grain size: 0.7mm Texture: subhedral, filling interstices of silicates Abundance: 2% Alteration: 5% by cubanite.	**1% oxides** **Magnetite** Grain size: 0.3mm Texture: exsolution texture with ilmenite Abundance: 1.9% Alteration: unaltered mineral **Ilmenite** Grain size: 0.1mm Texture: exsolution texture with magnetite with trellis and sandwich-type lamellae Abundance:0.1% Alteration: unaltered mineral.

APPENDIX B- Whole-rock Geochemistry

* All values are reported anhydrous. Major element oxides reported in weight percent. Trace elements reported in parts per million.

Method		Sample ID CAM-AC-22-01	Sample ID CAM-AC-22-02	Sample ID CAM-AC-22-03	Sample ID CAM-AC-22-04
ICP-AES	SiO_2	38.9	36.6	37.3	36.3
ICP-AES	Al_2O_3	4.57	4.21	4.93	5.11
ICP-AES	Fe_2O_3	16.5	17.65	17.3	16.45
ICP-AES	CaO	3.99	3.67	4.3	4.78
ICP-AES	MgO	25.6	25.5	24	21
ICP-AES	Na_2O	0.75	0.69	0.93	0.83
ICP-AES	K_2O	0.33	0.26	0.34	0.31
ICP-AES	Cr_2O_3	0.467	0.56	0.478	0.431
ICP-AES	TiO_2	1.08	1	1.07	1.18
ICP-AES	MnO	0.18	0.17	0.17	0.18
ICP-AES	P_2O_5	0.13	0.12	0.12	0.12
ICP-AES	SrO	0.03	0.02	0.03	0.04
ICP-AES	BaO	0.02	0.01	0.01	0.01

Method		Sample ID CAM-AC-22-05	Sample ID CAM-AC-22-08	Sample ID CAM-AC-22-09	Sample ID CAM-AC-22-11
ICP-AES	SiO_2	37.4	37.6	36.4	37.5
ICP-AES	Al_2O_3	5.34	4.56	4.95	4.81
ICP-AES	Fe_2O_3	18.05	17.05	18.95	17.9
ICP-AES	CaO	4.48	3.81	4.19	3.58
ICP-AES	MgO	21	23.7	23.1	24.4
ICP-AES	Na_2O	0.97	0.64	0.66	0.62
ICP-AES	K_2O	0.33	0.31	0.22	0.35
ICP-AES	Cr_2O_3	0.441	0.43	0.479	0.64
ICP-AES	TiO_2	1.18	1.12	1.12	1.16
ICP-AES	MnO	0.16	0.17	0.17	0.17
ICP-AES	P_2O_5	0.13	0.13	0.1	0.13
ICP-AES	SrO	0.03	0.02	0.03	0.02
ICP-AES	BaO	0.01	0.01	0.01	0.01

Method		Sample ID CAM-AC-22-14	Sample ID CAM-AC-22-21	Sample ID CAM-AC-22-23	Sample ID CAM-AC-22-30
ICP-AES	**SiO_2**	41.6	37.5	37.7	37.8
ICP-AES	**Al_2O_3**	4.99	4.07	3.97	4.23
ICP-AES	**Fe_2O_3**	15.5	15.25	16.4	16.45
ICP-AES	**CaO**	5.47	3.41	2.9	3.38
ICP-AES	**MgO**	21.9	27	28	27.3
ICP-AES	**Na_2O**	0.58	0.44	0.37	0.58
ICP-AES	**K_2O**	0.41	0.24	0.24	0.25
ICP-AES	**Cr_2O_3**	0.153	0.654	0.497	0.555
ICP-AES	**TiO_2**	0.98	1.01	0.91	1.01
ICP-AES	**MnO**	0.18	0.18	0.17	0.18
ICP-AES	**P_2O_5**	0.17	0.11	0.1	0.1
ICP-AES	**SrO**	0.03	0.02	0.02	0.03
ICP-AES	**BaO**	0.14	0.01	0.01	0.01

Method		Sample ID CAM-AC-22-35	Sample ID CAM-AC-22-43	Sample ID CAM-AC-22-45	Sample ID CAM-AC-22-46
ICP-AES	**SiO_2**	46.7	37.6	38.2	38.2
ICP-AES	**Al_2O_3**	10.35	3.13	3.36	3.51
ICP-AES	**Fe_2O_3**	13.8	16.85	15.35	16.85
ICP-AES	**CaO**	5.6	2.93	2.89	3.05
ICP-AES	**MgO**	10.5	30	30.1	29.5
ICP-AES	**Na_2O**	1.88	0.53	0.64	0.64
ICP-AES	**K_2O**	0.42	0.2	0.19	0.22
ICP-AES	**Cr_2O_3**	0.053	0.67	0.594	0.765
ICP-AES	**TiO_2**	2.68	0.79	0.8	0.82
ICP-AES	**MnO**	0.11	0.19	0.18	0.18
ICP-AES	**P_2O_5**	0.22	0.11	0.1	0.1
ICP-AES	**SrO**	0.15	0.02	0.02	0.02
ICP-AES	**BaO**	0.02	0.01	0.01	0.01

Method		Sample ID CAM-AC-22-53	Sample ID CAM-AC-22-55	Sample ID CAM-AC-22-57	Sample ID CAM-AC-22-65
ICP-AES	**SiO_2**	38	38.3	38.3	38.3
ICP-AES	**Al_2O_3**	3.79	4.18	3.89	4.47
ICP-AES	**Fe_2O_3**	15.6	15.25	16.7	16.3
ICP-AES	**CaO**	3.11	3.59	3.19	3.61
ICP-AES	**MgO**	28.4	28.2	28.8	26.7
ICP-AES	**Na_2O**	0.29	0.47	0.57	0.62
ICP-AES	**K_2O**	0.24	0.28	0.29	0.25
ICP-AES	**Cr_2O_3**	0.614	0.461	0.521	0.441
ICP-AES	**TiO_2**	0.94	1.04	0.93	1.08

ICP-AES	**MnO**	0.18	0.18	0.17	0.18
ICP-AES	**P_2O_5**	0.1	0.11	0.1	0.13
ICP-AES	**SrO**	0.02	0.03	0.03	0.03
ICP-AES	**BaO**	0.01	0.01	0.01	0.01

Method		**Sample ID CAM-AC-22-67**	**Sample ID CAM-AC-22-68**	**Sample ID CAM-AC-22-69**	**Sample ID CAM-AC-22-72**
ICP-AES	**SiO_2**	40.1	38.3	43.1	37.5
ICP-AES	**Al_2O_3**	6.66	4.39	6.59	4.78
ICP-AES	**Fe_2O_3**	15.3	17.7	15.5	15.75
ICP-AES	**CaO**	4.98	3.66	6.75	3.58
ICP-AES	**MgO**	20.6	24	17.95	26.2
ICP-AES	**Na_2O**	0.97	0.16	1.18	0.42
ICP-AES	**K_2O**	0.64	0.26	0.13	0.26
ICP-AES	**Cr_2O_3**	0.46	0.645	0.199	0.622
ICP-AES	**TiO_2**	1.55	1.09	1.6	1.1
ICP-AES	**MnO**	0.19	0.19	0.18	0.21
ICP-AES	**P_2O_5**	0.19	0.13	0.16	0.14
ICP-AES	**SrO**	0.04	0.01	0.02	0.02
ICP-AES	**BaO**	0.02	0.0065	0.0065	0.01

Method		**Sample ID CAM-AC-22-75**	**Sample ID CAM-MB-21-201**	**Sample ID CAM-MB-21-215**	**Sample ID CAM-MB-21-72**
ICP-AES	**SiO_2**	39	74.8	76.3	74.4
ICP-AES	**Al_2O_3**	4.27	14.35	15.2	14.65
ICP-AES	**Fe_2O_3**	16.4	1.35	1.02	1.65
ICP-AES	**CaO**	3.5	0.54	0.53	0.75
ICP-AES	**MgO**	28.6	0.49	0.21	0.57
ICP-AES	**Na_2O**	0.3	3.08	4.65	3.68
ICP-AES	**K_2O**	0.23	6.22	2.78	5.06
ICP-AES	**Cr_2O_3**	0.559	0.005	0.003	0.002
ICP-AES	**TiO_2**	1.02	0.13	0.05	0.19
ICP-AES	**MnO**	0.19	0.01	0.02	0.01
ICP-AES	**P_2O_5**	0.11	0.09	0.13	0.07
ICP-AES	**SrO**	0.03	0.01	0.0065	0.02
ICP-AES	**BaO**	0.01	0.04	0.0065	0.09

Method		**Sample ID CAM-MB-21-45**	**Sample ID CAM-MB-21-09**	**Sample ID CAM-MB-21-62**	**Sample ID CAM-MB-21-85**
ICP-AES	**SiO_2**	74.8	41.78	39.25	40.96
ICP-AES	**Al_2O_3**	14.1	4.84	4.54	4.90
ICP-AES	**Fe_2O_3**	1.57	18.90	23.80	19.71
ICP-AES	**CaO**	0.26	3.98	3.66	2.09

ICP-AES	**MgO**	1.02	27.63	25.97	28.99
ICP-AES	**Na_2O**	2.91	0.63	0.64	0.59
ICP-AES	**K_2O**	5.75	0.29	0.18	0.51
ICP-AES	**Cr_2O_3**	0.002	0.51	0.56	0.69
ICP-AES	**TiO_2**	0.17	1.08	1.05	1.19
ICP-AES	**MnO**	0.02	0.19	0.18	0.21
ICP-AES	**P_2O_5**	0.04	0.12	0.11	0.14
ICP-AES	**SrO**	0.02	0.03	0.03	0.01
ICP-AES	**BaO**	0.06	0.01	0.01	0.01

Method		**Sample ID CAM-MB-21-127**	**Sample ID CAM-MB-21-136**	**Sample ID CAM-MB-21-144**	**Sample ID CAM-MB-21-163**
ICP-AES	**SiO_2**	40.44	40.10	40.27	43.62
ICP-AES	**Al_2O_3**	4.13	2.49	2.96	5.50
ICP-AES	**Fe_2O_3**	19.52	17.08	17.14	16.81
ICP-AES	**CaO**	3.60	2.63	2.55	5.04
ICP-AES	**MgO**	29.41	35.59	34.59	25.82
ICP-AES	**Na_2O**	0.66	0.22	0.50	0.70
ICP-AES	**K_2O**	0.27	0.14	0.17	0.31
ICP-AES	**Cr_2O_3**	0.61	0.78	0.80	0.50
ICP-AES	**TiO_2**	1.02	0.64	0.70	1.28
ICP-AES	**MnO**	0.21	0.22	0.20	0.20
ICP-AES	**P_2O_5**	0.10	0.07	0.07	0.17
ICP-AES	**SrO**	0.03	0.02	0.02	0.04
ICP-AES	**BaO**	0.01	0.02	0.01	0.01

Method		**Sample ID CAM-MB-21-177**	**Sample ID CAM-MB-21-184**	**Sample ID CAM-MB-21-91**	**Sample ID CAM-MB-21-108**
ICP-AES	**SiO_2**	45.84	43.61	45.19	41.30
ICP-AES	**Al_2O_3**	6.62	5.53	4.44	3.68
ICP-AES	**Fe_2O_3**	17.46	16.89	17.27	17.59
ICP-AES	**CaO**	7.38	4.99	5.60	3.67
ICP-AES	**MgO**	19.61	25.62	24.52	30.97
ICP-AES	**Na_2O**	0.52	0.79	0.78	0.63
ICP-AES	**K_2O**	0.35	0.40	0.37	0.35
ICP-AES	**Cr_2O_3**	0.25	0.50	0.46	0.58
ICP-AES	**TiO_2**	1.54	1.24	1.02	0.88
ICP-AES	**MnO**	0.24	0.20	0.19	0.21
ICP-AES	**P_2O_5**	0.16	0.16	0.14	0.11
ICP-AES	**SrO**	0.01	0.04	0.01	0.02
ICP-AES	**BaO**	0.01	0.02	0.01	0.01

Method		Sample ID CAM-MB-21-30	Sample ID CAM-MB-21-61	Sample ID CAM-MB-21-65	Sample ID CAM-MB-21-74
ICP-AES	SiO_2	45.48	41.83	42.93	39.53
ICP-AES	Al_2O_3	7.74	5.64	5.30	5.21
ICP-AES	Fe_2O_3	15.43	19.97	19.58	22.45
ICP-AES	CaO	6.05	4.45	5.01	4.46
ICP-AES	MgO	20.57	24.65	24.01	25.18
ICP-AES	Na_2O	1.35	0.93	0.70	0.73
ICP-AES	K_2O	0.84	0.37	0.41	0.18
ICP-AES	Cr_2O_3	0.34	0.50	0.40	0.59
ICP-AES	TiO_2	1.71	1.28	1.22	1.31
ICP-AES	MnO	0.19	0.19	0.19	0.20
ICP-AES	P_2O_5	0.23	0.15	0.22	0.12
ICP-AES	SrO	0.05	0.03	0.03	0.03
ICP-AES	BaO	0.02	0.01	0.01	0.01

Method		Sample ID CAM-MB-21-83	Sample ID CAM-MB-21-93	Sample ID CAM-MB-21-101	Sample ID CAM-MB-21-109
ICP-AES	SiO_2	43.89	41.02	45.48	41.67
ICP-AES	Al_2O_3	7.28	4.42	7.48	4.22
ICP-AES	Fe_2O_3	18.31	19.53	15.42	17.12
ICP-AES	CaO	5.51	3.15	6.53	3.57
ICP-AES	MgO	20.98	28.98	21.02	30.72
ICP-AES	Na_2O	1.04	0.69	0.83	0.44
ICP-AES	K_2O	0.36	0.34	0.58	0.28
ICP-AES	Cr_2O_3	0.44	0.53	0.41	0.68
ICP-AES	TiO_2	1.69	0.98	1.80	0.95
ICP-AES	MnO	0.19	0.20	0.20	0.19
ICP-AES	P_2O_5	0.24	0.14	0.20	0.13
ICP-AES	SrO	0.04	0.02	0.04	0.02
ICP-AES	BaO	0.02	0.01	0.02	0.01

Method		Sample ID CAM-MB-21-118	Sample ID CAM-MB-21-122	Sample ID CAM-MB-21-140	Sample ID CAM-MB-21-152
ICP-AES	SiO_2	41.54	41.63	40.53	45.65
ICP-AES	Al_2O_3	3.66	4.16	5.21	6.43
ICP-AES	Fe_2O_3	17.67	17.66	20.96	18.31
ICP-AES	CaO	3.94	3.17	4.55	7.13
ICP-AES	MgO	30.41	30.56	25.52	19.41
ICP-AES	Na_2O	0.67	0.55	0.70	0.65
ICP-AES	K_2O	0.28	0.28	0.41	0.39
ICP-AES	Cr_2O_3	0.58	0.71	0.53	0.30
ICP-AES	TiO_2	0.91	0.97	1.22	1.37

ICP-AES	**MnO**	0.21	0.19	0.19	0.18
ICP-AES	**P_2O_5**	0.10	0.09	0.14	0.16
ICP-AES	**SrO**	0.02	0.02	0.03	0.01
ICP-AES	**BaO**	0.01	0.01	0.01	0.01

Method		**Sample ID**	**Sample ID**
		CAM-MB-21-156	**CAM-MB-21-171**
ICP-AES	**SiO_2**	40.39	41.14
ICP-AES	**Al_2O_3**	3.91	4.06
ICP-AES	**Fe_2O_3**	19.35	18.07
ICP-AES	**CaO**	3.22	3.69
ICP-AES	**MgO**	30.55	30.25
ICP-AES	**Na_2O**	0.42	0.47
ICP-AES	**K_2O**	0.22	0.33
ICP-AES	**Cr_2O_3**	0.72	0.57
ICP-AES	**TiO_2**	0.89	1.04
ICP-AES	**MnO**	0.19	0.21
ICP-AES	**P_2O_5**	0.10	0.14
ICP-AES	**SrO**	0.02	0.02
ICP-AES	**BaO**	0.01	0.01

Method		Sample ID CAM-AC-22-08	Sample ID CAM-AC-22-09	Sample ID CAM-AC-22-11	Sample ID CAM-AC-22-14
ICP-MS	**Ba**	113	88	103	1255
ICP-MS	**Ce**	33.06	26.65	31.99	43.80
ICP-MS	**Cr**	3566	3828	4961	1229
ICP-MS	**Cs**	0.44	0.33	0.58	3.82
ICP-MS	**Dy**	2.04	1.89	1.92	2.49
ICP-MS	**Er**	0.87	0.76	0.83	1.04
ICP-MS	**Eu**	1.06	1.04	1.12	1.37
ICP-MS	**Ga**	8.35	8.37	8.86	8.87
ICP-MS	**Gd**	3.10	2.65	2.75	4.01
ICP-MS	**Ge**	1.19	1.20	1.19	1.60
ICP-MS	**Hf**	2.63	2.18	2.53	2.81
ICP-MS	**Ho**	0.35	0.32	0.35	0.47
ICP-MS	**La**	13.77	10.77	13.40	18.70
ICP-MS	**Lu**	0.09	0.09	0.08	0.13
ICP-MS	**Nb**	8.84	7.59	9.38	10.79
ICP-MS	**Nd**	19.94	16.97	19.24	26.17
ICP-MS	**Pr**	4.63	3.80	4.69	6.15
ICP-MS	**Rb**	7.70	5.33	10.05	16.56
ICP-MS	**Sm**	4.43	3.50	4.21	5.26
ICP-MS	**Sn**	1.52	2.07	1.51	0.96
ICP-MS	**Sr**	238	295	258	309
ICP-MS	**Ta**	0.43	0.44	0.86	0.53
ICP-MS	**Tb**	0.41	0.35	0.38	0.48
ICP-MS	**Th**	0.91	0.71	0.97	1.27
ICP-MS	**Tm**	0.11	0.11	0.10	0.16
ICP-MS	**U**	0.29	0.27	0.29	0.36
ICP-MS	**V**	172	174	174	142
ICP-MS	**Y**	9.75	8.27	9.08	12.61
ICP-MS	**Yb**	0.67	0.54	0.64	0.84
ICP-MS	**Zr**	106	87	102	125
ICP-MS	**As**	1.08	3.05	0.97	5.34
ICP-MS	**Bi**	1.30	4.10	1.78	0.21
ICP-MS	**Se**	9.10	19.79	9.94	0.64
ICP-MS	**Te**	0.23	0.79	0.28	0.09
ICP-MS	**Tl**	0.07	0.05	0.06	0.30
ICP-AES	**Cd**	1.30	2.07	1.40	0.96
ICP-AES	**Co**	189	231	196	142
ICP-AES	**Cu**	5506	10528	6290	1007
ICP-AES	**Mo**	1.08	1.09	1.08	1.07
ICP-AES	**Ni**	3089	4644	3448	1095
ICP-AES	**Sc**	14.09	14.14	12.97	19.23
ICP-AES	**Zn**	113	110	116	114

Method		Sample ID CAM-AC-22-21	Sample ID CAM-AC-22-23	Sample ID CAM-AC-22-30	Sample ID CAM-AC-22-35
ICP-MS	**Ba**	89	74	94	215
ICP-MS	**Ce**	29.57	27.45	28.24	73.14
ICP-MS	**Cr**	5023	4007	4285	427
ICP-MS	**Cs**	1.02	0.67	0.41	0.90
ICP-MS	**Dy**	1.98	1.83	1.78	4.54
ICP-MS	**Er**	0.81	0.57	0.69	1.87
ICP-MS	**Eu**	1.01	0.92	1.00	2.51
ICP-MS	**Ga**	8.02	7.58	8.19	16.75
ICP-MS	**Gd**	2.83	2.56	2.51	6.55
ICP-MS	**Ge**	1.21	1.21	1.33	1.83
ICP-MS	**Hf**	2.20	2.09	2.23	5.48
ICP-MS	**Ho**	0.35	0.31	0.31	0.83
ICP-MS	**La**	12.20	11.42	12.07	31.36
ICP-MS	**Lu**	0.08	0.07	0.08	0.24
ICP-MS	**Nb**	7.90	8.14	8.35	20.08
ICP-MS	**Nd**	17.70	16.58	16.61	42.31
ICP-MS	**Pr**	4.14	3.91	3.81	9.87
ICP-MS	**Rb**	6.05	6.37	6.75	8.48
ICP-MS	**Sm**	3.59	3.38	3.53	8.85
ICP-MS	**Sn**	0.88	0.66	0.78	1.93
ICP-MS	**Sr**	195	233	270	1487
ICP-MS	**Ta**	0.44	0.44	0.44	1.18
ICP-MS	**Tb**	0.37	0.34	0.31	0.87
ICP-MS	**Th**	0.84	0.76	0.87	2.41
ICP-MS	**Tm**	0.10	0.09	0.10	0.25
ICP-MS	**U**	0.25	0.22	0.24	0.71
ICP-MS	**V**	156	141	157	410
ICP-MS	**Y**	9.01	7.91	8.19	21.48
ICP-MS	**Yb**	0.62	0.48	0.52	1.55
ICP-MS	**Zr**	91	88	89	220
ICP-MS	**As**	0.77	3.95	0.44	23.52
ICP-MS	**Bi**	0.14	0.05	0.16	1.57
ICP-MS	**Se**	1.10	0.55	0.66	3.01
ICP-MS	**Te**	0.07	0.02	0.04	0.46
ICP-MS	**Tl**	0.04	0.02	0.03	0.02
ICP-AES	**Cd**	0.66	0.55	0.78	0.54
ICP-AES	**Co**	159	168	173	88
ICP-AES	**Cu**	510	194	550	95
ICP-AES	**Mo**	1.10	1.10	1.11	1.07
ICP-AES	**Ni**	1720	1597	1822	171
ICP-AES	**Sc**	13.19	10.98	12.18	35.44
ICP-AES	**Zn**	119	120	125	63

Method		Sample ID CAM-AC-22-43	Sample ID CAM-AC-22-45	Sample ID CAM-AC-22-46	Sample ID CAM-AC-22-53
ICP-MS	**Ba**	78.63	118.72	87.35	72.78
ICP-MS	**Ce**	23.88	26.12	25.89	25.89
ICP-MS	**Cr**	4987	4663	5683	4732
ICP-MS	**Cs**	0.28	0.24	0.16	1.09
ICP-MS	**Dy**	1.44	1.61	1.54	1.62
ICP-MS	**Er**	0.56	0.64	0.61	0.70
ICP-MS	**Eu**	0.77	0.84	0.80	0.94
ICP-MS	**Ga**	6.05	6.37	6.52	7.18
ICP-MS	**Gd**	2.12	2.47	2.34	2.31
ICP-MS	**Ge**	1.17	1.19	1.16	1.20
ICP-MS	**Hf**	1.59	1.91	1.96	2.02
ICP-MS	**Ho**	0.27	0.26	0.29	0.28
ICP-MS	**La**	9.87	11.22	10.95	10.88
ICP-MS	**Lu**	0.05	0.08	0.06	0.08
ICP-MS	**Nb**	5.77	6.86	6.83	7.29
ICP-MS	**Nd**	14.75	15.43	15.15	15.77
ICP-MS	**Pr**	3.29	3.70	3.67	3.71
ICP-MS	**Rb**	4.99	4.32	4.95	6.96
ICP-MS	**Sm**	2.97	3.62	2.95	3.30
ICP-MS	**Sn**	0.96	0.65	0.74	0.65
ICP-MS	**Sr**	211	213	214	185
ICP-MS	**Ta**	0.32	0.32	0.42	0.33
ICP-MS	**Tb**	0.30	0.30	0.31	0.34
ICP-MS	**Th**	0.64	0.79	0.76	0.72
ICP-MS	**Tm**	0.07	0.09	0.08	0.10
ICP-MS	**U**	0.18	0.22	0.22	0.21
ICP-MS	**V**	120	120	128	144
ICP-MS	**Y**	6.90	7.34	7.16	7.51
ICP-MS	**Yb**	0.51	0.53	0.48	0.53
ICP-MS	**Zr**	67	79	79	81
ICP-MS	**As**	17.93	3.45	32.94	2.28
ICP-MS	**Bi**	1.02	0.25	3.36	0.07
ICP-MS	**Se**	3.82	0.32	2.53	0.76
ICP-MS	**Te**	2.09	0.26	1.87	0.04
ICP-MS	**Tl**	0.04	0.04	0.05	0.02
ICP-AES	**Cd**	0.96	0.65	1.05	0.65
ICP-AES	**Co**	184	165	196	162
ICP-AES	**Cu**	2621	535	3168	268
ICP-AES	**Mo**	1.06	1.08	1.05	1.09
ICP-AES	**Ni**	2610	1646	2810	1610
ICP-AES	**Sc**	10.61	10.79	11.58	13.05
ICP-AES	**Zn**	112	108	114	104

Method		Sample ID CAM-AC-22-55	Sample ID CAM-AC-22-57	Sample ID CAM-AC-22-65	Sample ID CAM-AC-22-67
ICP-MS	**Ba**	76	85	112	158
ICP-MS	**Ce**	27.98	24.98	34.00	47.60
ICP-MS	**Cr**	3513	4092	3336	3605
ICP-MS	**Cs**	0.66	0.53	0.26	2.44
ICP-MS	**Dy**	1.69	1.59	2.12	2.94
ICP-MS	**Er**	0.69	0.68	0.86	1.25
ICP-MS	**Eu**	1.03	0.80	1.24	1.54
ICP-MS	**Ga**	7.37	7.00	8.55	11.55
ICP-MS	**Gd**	2.70	2.32	3.04	4.20
ICP-MS	**Ge**	1.17	1.29	1.28	1.28
ICP-MS	**Hf**	2.20	2.15	2.58	3.68
ICP-MS	**Ho**	0.32	0.29	0.35	0.50
ICP-MS	**La**	11.64	10.34	14.11	19.90
ICP-MS	**Lu**	0.06	0.06	0.09	0.12
ICP-MS	**Nb**	7.84	8.15	9.54	13.26
ICP-MS	**Nd**	16.87	15.83	19.89	28.99
ICP-MS	**Pr**	3.95	3.66	4.79	6.73
ICP-MS	**Rb**	7.15	7.00	6.20	19.47
ICP-MS	**Sm**	3.29	3.39	3.95	5.33
ICP-MS	**Sn**	0.85	1.18	0.86	1.18
ICP-MS	**Sr**	286	268	289	382
ICP-MS	**Ta**	0.43	0.43	0.53	0.64
ICP-MS	**Tb**	0.31	0.30	0.41	0.56
ICP-MS	**Th**	0.79	0.74	0.99	1.42
ICP-MS	**Tm**	0.10	0.08	0.11	0.16
ICP-MS	**U**	0.23	0.22	0.28	0.41
ICP-MS	**V**	141	138	150	216
ICP-MS	**Y**	8.22	7.43	9.20	13.26
ICP-MS	**Yb**	0.57	0.45	0.65	0.96
ICP-MS	**Zr**	91	87	107	150
ICP-MS	**As**	2.35	15.29	0.43	1.93
ICP-MS	**Bi**	0.33	0.86	0.30	0.44
ICP-MS	**Se**	1.82	6.57	1.71	2.35
ICP-MS	**Te**	0.04	0.22	0.53	0.05
ICP-MS	**Tl**	0.02	0.03	0.04	1.94
ICP-AES	**Cd**	0.75	1.51	0.75	0.75
ICP-AES	**Co**	159	177	165	128
ICP-AES	**Cu**	443	2358	877	287
ICP-AES	**Mo**	1.07	1.08	1.07	1.07
ICP-AES	**Ni**	1772	2304	1893	1129
ICP-AES	**Sc**	12.81	10.77	11.76	16.05
ICP-AES	**Zn**	108	150	114	116

Method		Sample ID CAM-AC-22-68	Sample ID CAM-AC-22-69	Sample ID CAM-AC-22-72	Sample ID CAM-AC-22-75
ICP-MS	**Ba**	34	36	79	72
ICP-MS	**Ce**	35.41	47.35	35.87	27.74
ICP-MS	**Cr**	4873	1482	4750	4182
ICP-MS	**Cs**	2.96	1.66	1.76	2.45
ICP-MS	**Dy**	2.18	3.29	2.10	1.78
ICP-MS	**Er**	0.87	1.37	0.85	0.70
ICP-MS	**Eu**	1.14	1.62	1.20	0.91
ICP-MS	**Ga**	8.12	11.39	8.53	7.74
ICP-MS	**Gd**	2.99	4.79	3.11	2.53
ICP-MS	**Ge**	1.30	1.48	1.33	1.18
ICP-MS	**Hf**	2.71	3.63	2.72	2.20
ICP-MS	**Ho**	0.38	0.58	0.38	0.32
ICP-MS	**La**	14.29	19.62	15.06	11.40
ICP-MS	**Lu**	0.10	0.16	0.11	0.06
ICP-MS	**Nb**	8.78	11.76	9.49	7.48
ICP-MS	**Nd**	21.55	29.53	21.37	16.45
ICP-MS	**Pr**	4.96	6.78	5.04	3.81
ICP-MS	**Rb**	12.13	6.75	9.30	11.83
ICP-MS	**Sm**	4.32	6.54	3.94	3.26
ICP-MS	**Sn**	1.62	1.58	0.78	1.18
ICP-MS	**Sr**	48	134	204	225
ICP-MS	**Ta**	0.43	0.63	0.44	0.32
ICP-MS	**Tb**	0.40	0.62	0.41	0.34
ICP-MS	**Th**	1.07	1.47	0.94	0.80
ICP-MS	**Tm**	0.13	0.20	0.11	0.10
ICP-MS	**U**	0.29	0.46	0.32	0.24
ICP-MS	**V**	167	236	163	148
ICP-MS	**Y**	10.18	15.19	9.41	7.74
ICP-MS	**Yb**	0.71	0.89	0.66	0.58
ICP-MS	**Zr**	112	139	106	84
ICP-MS	**As**	7.58	14.76	2.77	3.66
ICP-MS	**Bi**	1.25	0.56	0.21	0.04
ICP-MS	**Se**	3.14	1.27	0.55	0.32
ICP-MS	**Te**	0.56	0.20	0.06	0.03
ICP-MS	**Tl**	0.31	0.03	0.48	0.12
ICP-AES	**Cd**	1.30	0.95	0.78	0.65
ICP-AES	**Co**	211	124	155	168
ICP-AES	**Cu**	5415	2573	424	215
ICP-AES	**Mo**	1.08	1.05	1.11	1.08
ICP-AES	**Ni**	3216	1577	1727	1688
ICP-AES	**Sc**	16.24	27.42	12.18	11.83
ICP-AES	**Zn**	110	143	113	116

Method		Sample ID CAM-MB-21-201	Sample ID CAM-MB-21-72	Sample ID CAM-MB-21-45	Sample ID CAM-MB-21-09
ICP-MS	**Ba**	348	821	557	114
ICP-MS	**Ce**	60	130	145	34
ICP-MS	**Cr**	38	21	15	3792
ICP-MS	**Cs**	1.74	1.65	1.77	0.36
ICP-MS	**Dy**	3.93	2.20	2.00	2.11
ICP-MS	**Er**	2.55	0.85	0.60	0.81
ICP-MS	**Eu**	0.41	0.75	0.74	1.12
ICP-MS	**Ga**	17.24	20.61	16.17	8.53
ICP-MS	**Gd**	3.29	3.28	4.68	3.01
ICP-MS	**Ge**	1.11	1.01	1.01	1.08
ICP-MS	**Hf**	3.31	4.63	4.98	2.77
ICP-MS	**Ho**	0.86	0.39	0.28	0.36
ICP-MS	**La**	27.52	67.77	72.95	13.29
ICP-MS	**Lu**	0.31	0.11	0.06	0.08
ICP-MS	**Nb**	8.72	12.22	4.44	8.72
ICP-MS	**Nd**	24.70	43.14	52.24	19.45
ICP-MS	**Pr**	6.89	13.78	16.07	4.49
ICP-MS	**Rb**	259	229	154	8
ICP-MS	**Sm**	4.58	6.31	8.45	3.73
ICP-MS	**Sn**	3.33	3.12	1.11	1.19
ICP-MS	**Sr**	97	180	135	271
ICP-MS	**Ta**	0.40	0.80	0.30	0.54
ICP-MS	**Tb**	0.57	0.40	0.50	0.44
ICP-MS	**Th**	17.84	25.64	40.01	1.18
ICP-MS	**Tm**	0.38	0.12	0.07	0.14
ICP-MS	**U**	5.51	5.27	2.50	1.44
ICP-MS	**V**	10	12	12	154
ICP-MS	**Y**	26.71	11.87	7.38	9.29
ICP-MS	**Yb**	2.24	0.82	0.40	0.75
ICP-MS	**Zr**	108	167	172	105
ICP-MS	**As**	0.07	0.20	0.07	0.65
ICP-MS	**Bi**	0.03	0.11	0.02	1.27
ICP-MS	**Se**	0.40	0.30	0.20	8.86
ICP-MS	**Te**	0.01	0.01	0.01	0.73
ICP-MS	**Tl**	0.06	0.13	0.03	0.05
ICP-AES	**Cd**	0.03	0.03	0.03	0.65
ICP-AES	**Co**	2.02	2.01	1.01	206.35
ICP-AES	**Cu**	7.06	4.02	2.02	4591.52
ICP-AES	**Mo**	1.01	0.65	0.66	-
ICP-AES	**Ni**	13	5	4	3284
ICP-AES	**Sc**	2.02	2.01	2.02	14.04
ICP-AES	**Zn**	16.13	17.09	16.17	113.44

Method		Sample ID CAM-MB-21-62	Sample ID CAM-MB-21-85	Sample ID CAM-MB-21-127	Sample ID CAM-MB-21-136
ICP-MS	**Ba**	99	116	101	211
ICP-MS	**Ce**	30	33	30	18
ICP-MS	**Cr**	4026	4843	4332	5567
ICP-MS	**Cs**	0.79	3.02	0.19	0.42
ICP-MS	**Dy**	1.75	1.95	1.82	1.05
ICP-MS	**Er**	0.80	0.77	0.94	0.52
ICP-MS	**Eu**	0.98	1.09	1.00	0.55
ICP-MS	**Ga**	8.52	8.96	8.11	5.43
ICP-MS	**Gd**	2.84	2.77	2.74	1.75
ICP-MS	**Ge**	1.00	1.09	1.07	0.87
ICP-MS	**Hf**	2.54	2.53	2.27	1.35
ICP-MS	**Ho**	0.37	0.32	0.37	0.21
ICP-MS	**La**	11.73	12.46	12.38	7.38
ICP-MS	**Lu**	0.10	0.08	0.07	0.04
ICP-MS	**Nb**	8.45	9.23	7.91	4.21
ICP-MS	**Nd**	17.70	18.37	16.65	10.42
ICP-MS	**Pr**	3.99	4.38	4.14	2.52
ICP-MS	**Rb**	5.42	21.76	5.76	4.12
ICP-MS	**Sm**	3.75	3.53	3.59	2.02
ICP-MS	**Sn**	1.22	0.98	1.39	-
ICP-MS	**Sr**	241	140	245	183
ICP-MS	**Ta**	0.55	0.55	0.43	0.33
ICP-MS	**Tb**	0.39	0.37	0.35	0.23
ICP-MS	**Th**	0.87	1.01	0.95	0.50
ICP-MS	**Tm**	0.11	0.10	0.11	0.07
ICP-MS	**U**	0.28	0.44	0.26	0.16
ICP-MS	**V**	150	160	146	102
ICP-MS	**Y**	8.30	8.09	8.43	5.10
ICP-MS	**Yb**	0.74	0.69	0.61	0.41
ICP-MS	**Zr**	98	103	96	55
ICP-MS	**As**	1.11	3.50	0.96	88.98
ICP-MS	**Bi**	1.73	0.69	1.38	0.21
ICP-MS	**Se**	16.70	9.84	7.15	1.19
ICP-MS	**Te**	3.12	0.47	0.38	0.62
ICP-MS	**Tl**	0.15	0.55	0.02	0.09
ICP-AES	**Cd**	1.00	0.87	0.85	-
ICP-AES	**Co**	321	214	216	176
ICP-AES	**Cu**	6947	3367	4599	604
ICP-AES	**Ni**	6372	3028	3276	1921
ICP-AES	**Sc**	12.17	12.03	11.74	9.77
ICP-AES	**Zn**	127	136	112	114

Method		Sample ID CAM-MB-21-144	Sample ID CAM-MB-21-163	Sample ID CAM-MB-21-177	Sample ID CAM-MB-21-184
ICP-MS	**Ba**	72	132	57	157
ICP-MS	**Ce**	22	35	51	42
ICP-MS	**Cr**	6472	3841	1892	3886
ICP-MS	**Cs**	0.27	3.24	3.73	1.64
ICP-MS	**Dy**	1.30	2.20	2.98	2.50
ICP-MS	**Er**	0.61	0.92	1.40	1.24
ICP-MS	**Eu**	0.67	1.32	1.48	1.38
ICP-MS	**Ga**	6.10	9.44	11.28	10.40
ICP-MS	**Gd**	2.04	3.43	4.64	3.81
ICP-MS	**Ge**	1.16	1.27	1.05	1.27
ICP-MS	**Hf**	1.66	2.54	3.51	3.22
ICP-MS	**Ho**	0.24	0.41	0.56	0.48
ICP-MS	**La**	8.84	14.33	21.30	17.20
ICP-MS	**Lu**	0.06	0.12	0.15	0.10
ICP-MS	**Nb**	5.70	9.85	14.02	10.46
ICP-MS	**Nd**	12.21	19.74	26.88	23.46
ICP-MS	**Pr**	2.90	4.75	6.66	5.55
ICP-MS	**Rb**	4.21	12.10	14.34	13.17
ICP-MS	**Sm**	2.40	4.15	5.71	4.60
ICP-MS	**Sn**	0.53	0.85	1.48	1.17
ICP-MS	**Sr**	172	352	75	355
ICP-MS	**Ta**	0.32	0.64	0.84	0.64
ICP-MS	**Tb**	0.26	0.44	0.56	0.50
ICP-MS	**Th**	0.72	1.08	1.69	1.34
ICP-MS	**Tm**	0.06	0.12	0.18	0.14
ICP-MS	**U**	0.20	0.34	0.46	0.36
ICP-MS	**V**	110	162	218	173
ICP-MS	**Y**	5.89	10.08	13.49	11.68
ICP-MS	**Yb**	0.45	0.82	1.02	0.82
ICP-MS	**Zr**	66	106	139	133
ICP-MS	**As**	1.26	1.27	8.54	0.32
ICP-MS	**Bi**	0.14	0.45	0.62	0.44
ICP-MS	**Se**	1.16	1.80	4.43	2.44
ICP-MS	**Te**	0.22	0.20	0.24	0.20
ICP-MS	**Tl**	0.03	0.27	0.24	0.23
ICP-AES	**Cd**	-	-	14.23	0.64
ICP-AES	**Co**	182	145	144	150
ICP-AES	**Cu**	772	1093	4185	2665
ICP-AES	**Ni**	2105	1528	1486	1545
ICP-AES	**Sc**	10.52	15.92	24.25	15.93
ICP-AES	**Zn**	114	117	4069	155

Method		Sample ID CAM-MB-21-91	Sample ID CAM-MB-21-108	Sample ID CAM-MB-21-30	Sample ID CAM-MB-21-61
ICP-MS	**Ba**	127	108	178	121
ICP-MS	**Ce**	40	29	52	36
ICP-MS	**Cr**	3108	4046	2555	3523
ICP-MS	**Cs**	2.64	2.65	2.89	0.64
ICP-MS	**Dy**	2.34	1.70	3.00	2.19
ICP-MS	**Er**	1.03	0.73	1.51	1.04
ICP-MS	**Eu**	1.08	0.83	1.76	1.24
ICP-MS	**Ga**	8.80	6.73	12.62	10.58
ICP-MS	**Gd**	3.52	2.48	4.90	3.36
ICP-MS	**Ge**	1.49	0.95	1.47	1.31
ICP-MS	**Hf**	2.94	2.20	3.76	2.92
ICP-MS	**Ho**	0.41	0.28	0.57	0.43
ICP-MS	**La**	15.91	11.25	20.19	13.96
ICP-MS	**Lu**	0.13	0.07	0.15	0.09
ICP-MS	**Nb**	9.01	7.42	12.51	9.88
ICP-MS	**Nd**	22.59	17.24	31.55	21.82
ICP-MS	**Pr**	4.97	3.73	7.02	4.84
ICP-MS	**Rb**	13.15	11.46	29.13	9.60
ICP-MS	**Sm**	4.04	3.12	6.06	4.47
ICP-MS	**Sn**	0.85	0.74	1.26	1.96
ICP-MS	**Sr**	155	228	401	284
ICP-MS	**Ta**	0.53	0.42	0.74	0.55
ICP-MS	**Tb**	0.48	0.30	0.64	0.47
ICP-MS	**Th**	1.78	0.87	1.78	1.13
ICP-MS	**Tm**	0.14	0.09	0.19	0.13
ICP-MS	**U**	0.60	0.25	0.45	0.32
ICP-MS	**V**	169	129	219	169
ICP-MS	**Y**	10.18	7.57	14.20	9.93
ICP-MS	**Yb**	0.78	0.57	1.08	0.81
ICP-MS	**Zr**	114	84	145	113
ICP-MS	**As**	3.08	2.31	5.26	22.58
ICP-MS	**Bi**	0.52	0.73	0.34	2.63
ICP-MS	**Se**	1.17	1.05	1.26	14.62
ICP-MS	**Te**	0.43	0.18	0.58	1.96
ICP-MS	**Tl**	1.37	0.23	0.49	0.12
ICP-AES	**Cd**	-	-	-	1.42
ICP-AES	**Co**	159	177	120	217
ICP-AES	**Cu**	1830	2228	836	9206
ICP-AES	**Ni**	1888	2291	1052	3883
ICP-AES	**Sc**	18.03	12.61	17.88	15.27
ICP-AES	**Zn**	134	115	118	116

Method		Sample ID CAM-MB-21-65	Sample ID CAM-MB-21-74	Sample ID CAM-MB-21-83	Sample ID CAM-MB-21-93
ICP-MS	**Ba**	85	80	191	116
ICP-MS	**Ce**	46	29	57	41
ICP-MS	**Cr**	2978	4251	3070	3704
ICP-MS	**Cs**	2.61	1.25	2.83	0.44
ICP-MS	**Dy**	2.76	2.02	3.33	2.20
ICP-MS	**Er**	1.11	0.86	1.34	1.08
ICP-MS	**Eu**	1.42	1.11	1.87	1.17
ICP-MS	**Ga**	9.50	9.15	12.07	7.86
ICP-MS	**Gd**	3.83	2.89	4.75	3.19
ICP-MS	**Ge**	1.17	1.18	1.27	1.08
ICP-MS	**Hf**	3.12	2.35	3.97	2.95
ICP-MS	**Ho**	0.47	0.37	0.60	0.42
ICP-MS	**La**	18.57	11.19	22.55	16.26
ICP-MS	**Lu**	0.11	0.09	0.14	0.13
ICP-MS	**Nb**	10.78	8.14	16.62	11.04
ICP-MS	**Nd**	26.90	18.72	33.67	23.15
ICP-MS	**Pr**	6.02	4.07	7.43	5.25
ICP-MS	**Rb**	18.57	5.70	13.76	7.97
ICP-MS	**Sm**	5.24	3.78	6.75	4.22
ICP-MS	**Sn**	1.28	1.83	1.27	1.40
ICP-MS	**Sr**	286	271	380	229
ICP-MS	**Ta**	0.64	0.54	0.74	0.65
ICP-MS	**Tb**	0.52	0.42	0.69	0.43
ICP-MS	**Th**	1.37	0.76	1.68	1.31
ICP-MS	**Tm**	0.17	0.12	0.20	0.14
ICP-MS	**U**	0.52	0.26	0.46	0.37
ICP-MS	**V**	173	185	210	126
ICP-MS	**W**	-	-	-	1.29
ICP-MS	**Y**	11.95	8.72	14.61	10.23
ICP-MS	**Yb**	0.82	0.72	1.02	0.81
ICP-MS	**Zr**	127	95	163	121
ICP-MS	**As**	3.20	1.51	1.69	5.06
ICP-MS	**Bi**	1.88	0.93	1.05	0.65
ICP-MS	**Se**	8.32	15.17	6.35	4.31
ICP-MS	**Te**	0.85	1.68	0.49	0.34
ICP-MS	**Tl**	0.09	0.46	0.72	0.04
ICP-AES	**Cd**	0.85	1.18	-	0.54
ICP-AES	**Co**	218	284	184	221
ICP-AES	**Cu**	4675	10352	3208	4587
ICP-AES	**Mo**	-	1.08	1.06	-
ICP-AES	**Ni**	2711	5520	2668	2756
ICP-AES	**Sc**	16.0	15.1	18.0	11.8
ICP-AES	**Zn**	131	125	113	120

Method		Sample ID CAM-MB-21-101	Sample ID CAM-MB-21-109	Sample ID CAM-MB-21-118	Sample ID CAM-MB-21-122
ICP-MS	**Ba**	199	110	111	90
ICP-MS	**Ce**	54	32	28	30
ICP-MS	**Cr**	2937	4763	4177	4946
ICP-MS	**Cs**	3.18	1.03	1.02	0.59
ICP-MS	**Dy**	3.56	1.83	1.71	1.78
ICP-MS	**Er**	1.41	0.83	0.78	0.78
ICP-MS	**Eu**	1.75	1.02	0.89	0.96
ICP-MS	**Ga**	12.63	7.69	7.38	7.88
ICP-MS	**Gd**	4.90	2.58	2.55	2.63
ICP-MS	**Ge**	1.37	1.19	1.05	0.88
ICP-MS	**Hf**	4.01	2.31	1.96	2.43
ICP-MS	**Ho**	0.56	0.32	0.33	0.35
ICP-MS	**La**	21.16	12.45	11.39	12.15
ICP-MS	**Lu**	0.14	0.09	0.08	0.10
ICP-MS	**Nb**	13.21	7.46	7.15	7.51
ICP-MS	**Nd**	31.79	18.08	15.82	16.19
ICP-MS	**Pr**	6.92	4.15	3.75	4.05
ICP-MS	**Rb**	22.42	8.44	9.07	8.64
ICP-MS	**Sm**	6.42	3.62	3.29	3.34
ICP-MS	**Sn**	1.16	0.76	0.84	0.98
ICP-MS	**Sr**	375	213	230	195
ICP-MS	**Ta**	0.74	0.43	0.42	0.44
ICP-MS	**Tb**	0.65	0.35	0.34	0.34
ICP-MS	**Th**	1.60	1.00	0.86	0.93
ICP-MS	**Tm**	0.19	0.11	0.12	0.10
ICP-MS	**U**	0.41	0.25	0.32	0.28
ICP-MS	**V**	233	136	140	140
ICP-MS	**Y**	14.53	8.23	7.70	7.88
ICP-MS	**Yb**	1.06	0.62	0.56	0.60
ICP-MS	**Zr**	158	100	84	97
ICP-MS	**As**	1.37	0.32	2.11	0.66
ICP-MS	**Bi**	0.12	0.76	0.61	1.60
ICP-MS	**Se**	0.95	3.90	1.79	5.47
ICP-MS	**Te**	0.04	0.75	0.33	0.81
ICP-MS	**Tl**	0.32	0.06	0.04	0.03
ICP-AES	**Co**	112	183	172	179
ICP-AES	**Cu**	487	2219	2247	3491
ICP-AES	**Ni**	1030	2512	2289	2429
ICP-AES	**Sc**	20.00	12.99	13.71	13.13
ICP-AES	**Zn**	107	108	111	107

Method		Sample ID CAM-MB-21-140	Sample ID CAM-MB-21-152	Sample ID CAM-MB-21-156	Sample ID CAM-MB-21-171
ICP-MS	**Ba**	126	76	87	98
ICP-MS	**Ce**	32	25	47	32
ICP-MS	**Cr**	3881	5165	2220	4410
ICP-MS	**Cs**	1.06	0.37	3.52	1.70
ICP-MS	**Dy**	2.10	1.53	2.91	2.01
ICP-MS	**Er**	0.92	0.73	1.27	0.84
ICP-MS	**Eu**	1.17	0.84	1.26	0.97
ICP-MS	**Ga**	9.43	7.46	11.15	8.22
ICP-MS	**Gd**	3.23	2.45	4.21	2.97
ICP-MS	**Ge**	0.75	0.86	1.05	1.07
ICP-MS	**Hf**	2.56	1.96	3.57	2.41
ICP-MS	**Ho**	0.40	0.26	0.52	0.37
ICP-MS	**La**	12.76	10.27	19.78	13.03
ICP-MS	**Lu**	0.11	0.09	0.14	0.10
ICP-MS	**Nb**	8.35	6.75	12.10	7.90
ICP-MS	**Nd**	18.98	14.05	25.04	17.72
ICP-MS	**Pr**	4.48	3.46	6.27	4.27
ICP-MS	**Rb**	10.18	4.86	15.78	9.82
ICP-MS	**Sm**	3.76	2.83	4.97	3.70
ICP-MS	**Sn**	1.39	0.86	1.58	0.85
ICP-MS	**Sr**	331	220	130	226
ICP-MS	**Ta**	0.54	0.43	0.74	0.53
ICP-MS	**Tb**	0.39	0.35	0.54	0.40
ICP-MS	**Th**	1.01	0.75	1.68	1.00
ICP-MS	**Tm**	0.13	0.10	0.17	0.11
ICP-MS	**U**	0.28	0.21	0.52	0.32
ICP-MS	**V**	165	137	209	151
ICP-MS	**W**	0.54	-	0.84	0.53
ICP-MS	**Y**	9.54	7.02	12.84	9.18
ICP-MS	**Yb**	0.69	0.57	0.97	0.64
ICP-MS	**Zr**	104	79	136	104
ICP-MS	**As**	18.65	0.43	9.47	11.74
ICP-MS	**Bi**	2.15	0.96	0.95	0.44
ICP-MS	**Se**	11.47	6.38	4.95	2.03
ICP-MS	**Te**	0.38	0.99	0.38	0.14
ICP-MS	**Tl**	0.05	0.04	0.96	0.06
ICP-AES	**Cd**	1.93	-	-	-
ICP-AES	**Co**	238	215	180	175
ICP-AES	**Cu**	8898	4074	4251	1527
ICP-AES	**Ni**	4267	3317	2283	2167
ICP-AES	**Sc**	13.94	10.81	23.15	12.81
ICP-AES	**Zn**	140	116	101	120

APPENDIX C- Mineral Chemistry

*Calculation of the serpentine and chlorite structural formula based on 14 and 28 oxygens, respectively. Calculated assuming full site occupancy. Method Reference: Deer, Howie & Zussman (1992).

Sample-ID	**AC-CAM-22-02**	**AC-CAM-22-03**	**AC-CAM-22-05**	**AC-CAM-22-16**
sem-Site	**SEM-03**	**SEM-01**	**SEM-04**	**SEM-01**
Analysis-ID	**Chlorite**	**Chlorite**	**Chlorite**	**Chlorite**
SiO2 wt%	37.09	42.06	38.80	33.43
Al2O3 wt%	4.65	1.72	4.27	10.24
FeO wt%	8.71	5.79	12.72	17.26
Fe2O3 wt%	-	-	-	-
MgO wt%	36.99	37.26	31.29	26.69
CaO wt%	-	-	-	-
Na2O wt%	-	-	-	-
K2O wt%	-	-	-	-
H2O wt%	12.92	12.64	12.71	11.92
TOTAL	100.36	99.47	99.79	99.54

Sample ID	**AC-CAM-22-67**	**AC-CAM-22-69**	**AC-CAM-22-69**	**AC-CAM-22-69**
SEM Site	**SEM-02**	**SEM-01**	**SEM-02**	**SEM-04-1**
Analysis ID	**Chlorite**	**Chlorite**	**Chlorite**	**Chlorite**
SiO2 wt%	39.82	43.82	33.10	34.60
Al2O3 wt%	6.16	7.39	13.37	11.09
FeO wt%	7.82	9.13	17.10	13.93
Fe2O3 wt%	-	-	-	-
MgO wt%	33.31	27.15	23.80	26.55
CaO wt%	-	-	-	-
Na2O wt%	-	-	-	-
K2O wt%	-	-	-	-
H2O wt%	12.27	12.75	11.70	12.00
TOTAL	99.38	100.24	99.07	98.17

Sample ID	AC-CAM-22-69	AC-CAM-22-16	AC-CAM-22-77	AC-CAM-22-77
SEM Site	SEM-05	SEM-02	SEM-01	SEM-02-01
Analysis ID	Chlorite	Chlorite	Chlorite	Chlorite
SiO2 wt%	46.71	31.78	33.31	39.31
Al2O3 wt%	5.59	13.57	10.11	3.56
FeO wt%	8.91	21.47	16.02	11.02
Fe2O3 wt%	-	-	-	-
MgO wt%	25.45	21.20	27.85	33.97
CaO wt%	-	-	-	-
Na2O wt%	-	-	-	-
K2O wt%	-	-	-	-
H2O wt%	13.08	11.75	12.11	12.40
TOTAL	99.74	99.77	99.40	100.26

Sample ID	AC-CAM-22-77	AC-CAM-22-67	AC-CAM-22-69	AC-CAM-22-69
SEM Site	SEM-02-02	SEM-02	SEM-01	SEM-03
Analysis ID	Chlorite	Chlorite	Chlorite	Chlorite
SiO2 wt%	33.17	35.51	39.63	35.57
Al2O3 wt%	11.96	10.59	9.50	10.25
FeO wt%	14.16	8.56	10.10	14.51
Fe2O3 wt%	-	-	-	-
MgO wt%	26.96	32.54	27.45	26.09
CaO wt%	-	-	-	-
Na2O wt%	-	-	-	-
K2O wt%	-	-	-	-
H2O wt%	11.95	12.31	12.46	11.95
TOTAL	98.20	99.51	99.14	98.37

Sample ID	AC-CAM-22-69	AC-CAM-22-171	AC-CAM-22-07	AC-CAM-22-07
SEM Site	SEM-04-2	SEM-01	SEM-02-01	SEM-02-02
Analysis ID	Chlorite	Chlorite	Chlorite	Chlorite
SiO2 wt%	30.99	40.19	41.40	35.61
Al2O3 wt%	14.68	6.42	3.79	6.55
FeO wt%	20.01	7.61	12.56	15.41
Fe2O3 wt%	-	-	-	-
MgO wt%	21.08	31.95	28.75	29.67
CaO wt%	-	-	-	-
Na2O wt%	-	-	-	-
K2O wt%	-	-	-	-
H2O wt%	11.66	12.48	12.75	11.99
TOTAL	98.42	98.65	99.25	99.23

Sample ID	AC-CAM-22-07	AC-CAM-22-28	AC-CAM-22-28	AC-CAM-22-28
SEM Site	SEM-03-01	SEM-02-01	SEM-03	SEM-05
Analysis ID	Chlorite	Chlorite	Chlorite	Chlorite
SiO2 wt%	36.40	38.63	40.19	29.45
Al2O3 wt%	7.93	3.65	2.18	17.66
FeO wt%	12.47	12.14	7.71	14.30
Fe2O3 wt%	-	-	-	-
MgO wt%	31.00	32.78	37.15	26.65
CaO wt%	-	-	-	-
Na2O wt%	-	-	-	-
K2O wt%	-	-	-	-
H2O wt%	11.83	12.01	12.23	11.93
TOTAL	99.63	99.21	99.46	99.99

Sample ID	AC-CAM-22-28	AC-CAM-22-38	AC-CAM-22-38	AC-CAM-22-38
SEM Site	SEM-06	SEM-01-01	SEM-02-03	SEM-03-01
Analysis ID	Chlorite	Chlorite	Chlorite	Chlorite
SiO2 wt%	40.22	35.36	39.01	35.49
Al2O3 wt%	3.04	8.39	4.75	7.81
FeO wt%	7.30	16.34	11.85	18.42
Fe2O3 wt%	-	-	-	-
MgO wt%	37.19	28.13	31.93	25.91
CaO wt%	-	-	-	-
Na2O wt%	-	-	-	-
K2O wt%	-	-	-	-
H2O wt%	12.32	11.64	11.87	11.74
TOTAL	100.07	99.86	99.41	99.37

Sample ID	AC-CAM-22-71	AC-CAM-22-71	AC-CAM-22-71	AC-CAM-22-71
SEM Site	SEM-01	SEM-02-01	SEM-02-02	SEM-02-04
Analysis ID	Chlorite	Chlorite	Chlorite	Chlorite
SiO2 wt%	34.19	39.99	30.27	36.85
Al2O3 wt%	5.96	5.16	14.41	7.55
FeO wt%	19.75	5.95	17.28	10.53
Fe2O3 wt%	-	-	-	-
MgO wt%	28.62	36.79	26.09	32.34
CaO wt%	-	-	-	-
Na2O wt%	-	-	-	-
K2O wt%	-	-	-	-
H2O wt%	11.45	12.15	11.55	11.89

TOTAL	99.97	100.04	99.60	99.16

Sample ID	**AC-CAM-22-71**	**CAM-AC-22-35**	**CAM-AC-22-35**	**CAM-AC-22-35**
SEM Site	**SEM-03**	**SEM-01**	**SEM-02**	**SEM-03**
Analysis ID	**Chlorite**	**Chlorite**	**Chlorite**	**Chlorite**
SiO2 wt%	34.76	24.45	25.37	27.14
Al2O3 wt%	6.45	20.10	20.90	18.01
FeO wt%	15.85	28.50	25.78	25.37
Fe2O3 wt%	-	2.17	3.36	5.28
MgO wt%	30.21	12.65	10.35	11.58
CaO wt%	-	0.45	0.90	0.64
Na2O wt%	-	0.10	0.51	0.68
K2O wt%	-	0.27	0.41	0.57
H2O wt%	11.93	11.81	11.51	10.65
TOTAL	99.20	100.50	99.10	99.92

Sample ID	**CAM-AC-22-35**
SEM Site	**SEM-03-1**
Analysis ID	**Chlorite**
SiO2 wt%	27.42
Al2O3 wt%	19.40
FeO wt%	28.50
Fe2O3 wt%	1.02
MgO wt%	11.04
CaO wt%	0.32
Na2O wt%	0.21
K2O wt%	0.91
H2O wt%	11.18
TOTAL	100.00

Sample ID	**AC-CAM-22-02**	**AC-CAM-22-02**	**AC-CAM-22-02**	**AC-CAM-22-03**
SEM Site	**SEM 01**	**SEM 02-01**	**SEM 02-02**	**SEM 03-02**
Analysis ID	**Lizardite-chrysotile**	**Lizardite-chrysotile**	**Lizardite-chrysotile**	**Lizardite-chrysotile**
SiO2 Wt. %	40.69	40.17	41.32	41.02
Al2O3 Wt. %	0.6	0.68	0.49	0.57
Fe2O wt%	0.22	0.25	1.15	1.13
FeO Wt. %	0.14	0.15	0.1	0.11
MgO Wt.%	41.23	42.51	41.78	41.89
H2O Wt. %	13.98	14.2	14.12	13.65
Total	96.86	97.96	98.96	98.37

Sample ID	AC-CAM-22-77	AC-CAM-22-03	AC-CAM-22-03	AC-CAM-22-03
SEM Site	SEM 01	SEM 02-01	SEM 02-02	SEM 03-01
Analysis ID	Lizardite-chrysotile	Lizardite-chrysotile	Lizardite-chrysotile	Lizardite-chrysotile
SiO2 Wt. %	41.12	42.74	39.77	42.13
Al2O3 Wt. %	0.55	0.13	0.65	0.11
Fe2O wt%	1.17	0.19	0.35	0.1
FeO Wt. %	0.12	0.089	0.18	0.09
MgO Wt.%	41.81	41.78	42.43	41.1
H2O Wt. %	13.56	13.78	14.32	13.23
Total	98.33	98.709	97.7	96.76

Sample ID	AC-CAM-22-28	AC-CAM-22-28	AC-CAM-22-07	AC-CAM-22-83
SEM Site	SEM 01-02	SEM 01-01	SEM 03-03	SEM-01
Analysis ID	Lizardite-chrysotile	Lizardite-chrysotile	Antigorite	Antigorite
SiO2 Wt. %	39.85	40.75	45.85	44.34
Al2O3 Wt. %	0.55	0.35	1.15	1.24
Fe2O wt%	0.4	0.27	0.79	0.81
FeO Wt. %	0.15	0.1	0.6	0.79
MgO Wt.%	42.4	41.65	38.21	39.12
H2O Wt. %	14.23	13.98	11.59	12.23
Total	97.58	97.1	98.19	98.53

Sample ID	AC-CAM-22-171	AC-CAM-22-71	AC-CAM-22-71
SEM Site	SEM 01	SEM 04-01	SEM-05-01
Analysis ID	Antigorite	Antigorite	Antigorite
SiO2 Wt. %	43.04	43.28	44.92
Al2O3 Wt. %	1.39	1.3	1.15
Fe2O wt%	0.93	0.9	0.84
FeO Wt. %	0.89	0.8	0.76
MgO Wt.%	39.44	39.6	39.1
H2O Wt. %	12.68	12.49	12.13
Total	98.37	98.37	98.9

Sample ID sem Site Analysis ID	CAM-AC-22-07 SEM 03-02 Augite	CAM-AC-22-07 SEM 03-03 Estatite	CAM-AC-22-38 SEM 01-04 Augite	CAM-AC-22-74 SEM 04-02 Estatite
Na2O Wt.%	1.01	-	0.90	-
CaO Wt. %	16.85	1.29	17.67	1.23
Al2O Wt. %	4.34	0.84	2.71	0.57
MgO Wt. %	19.34	40.42	20.12	39.12
TiO2 Wt. %	2.09	-	1.48	-
FeO Wt. %	5.89	8.27	6.40	6.32
SiO2 Wt. %	50.96	48.91	50.57	52.43
Total	100.48	99.73	99.85	99.67

Sample ID sem Site Analysis ID	CAM-AC-22-41 SEM 02 Augite	CAM-AC-22-69 SEM 02 Augite
Na2O Wt.%	0.3	0.38
CaO Wt. %	18.14	17.48
Al2O Wt. %	2.45	2.52
MgO Wt. %	19.32	18.72
TiO2 Wt. %	0.95	1.35
FeO Wt. %	6.78	7.68
SiO2 Wt. %	51.12	51.23
Total	99.06	99.36

APPENDIX D- Radiogenic Isotopes

Sample ID	Zone	ε_{Nd}	$^{147}Sm/^{144}Nd$	$^{143}Nd/^{144}Nd$ (init)	$^{143}Nd/^{144}Nd$ (current)
CAM-MB-21-09	Current	-2.0393	0.12385	0.51110	0.51200
CAM-MB-21-62	Current	-1.1986	0.12889	0.51115	0.51208
CAM-MB-21-85	Beaver-Cloud	-1.1828	0.12312	0.51115	0.51204
CAM-MB-21-127	Beaver-Cloud	-1.7524	0.12314	0.51112	0.51201
CAM-MB-21-136	Beaver-Cloud	-2.2291	0.12380	0.51109	0.51199
CAM-MB-21-144	Beaver-Cloud	-2.2177	0.12348	0.51109	0.51199
CAM-MB-21-163	437-SEA	-2.6912	0.12476	0.51107	0.51198
CAM-MB-21-177	437-SEA	-2.5732	0.12003	0.51108	0.51195
CAM-MB-21-184	437-SEA	-2.1997	0.12322	0.51110	0.51199
CAM-MB-21-91	Beaver-Cloud	-4.0157	0.12308	0.51100	0.51190

Sample ID	Zone	Sr_i	$^{87}Rb/^{86}Sr$	$^{87}Sr/^{86}Sr$ (current)
CAM-MB-21-09	Current	0.70256	0.08964	0.7039786
CAM-MB-21-62	Current	0.70256	0.06505	0.70358877
CAM-MB-21-85	Beaver-Cloud	0.70216	0.45062	0.70930116
CAM-MB-21-127	Beaver-Cloud	0.70269	0.06800	0.70377016
CAM-MB-21-136	Beaver-Cloud	0.70407	0.06513	0.70509853
CAM-MB-21-144	Beaver-Cloud	0.70267	0.07079	0.70379361
CAM-MB-21-163	437-SEA	0.70293	0.09943	0.70450801
CAM-MB-21-177	437-SEA	0.70439	0.54904	0.71308415
CAM-MB-21-184	437-SEA	0.70303	0.10756	0.70473216
CAM-MB-21-91	Beaver-Cloud	0.70381	0.24641	0.70771573

APPENDIX E- Stable isotopes

Sample ID	Zone	$\delta^{2}H$	$\delta^{18}O$
CAM-AC-22-14	Beaver-Cloud	-89	6.1
CAM-AC-22-21	Beaver-Cloud	-100	4.5
CAM-AC-22-23	Beaver-Cloud	-108	3.9
CAM-AC-22-30	Beaver-Cloud	-116	5.1
CAM-AC-22-35	437-SEA	-93	6.7
CAM-AC-22-43	437-SEA	-105	5.4
CAM-AC-22-53	437-SEA	-91	4.9
CAM-AC-22-55	437-SEA	-95	5.4
CAM-AC-22-67	437-SEA	-106	6
CAM-AC-22-69	Beaver-Cloud	-91	5.5
CAM-MB-21-09	Current	-92	5.6
CAM-MB-21-62	Current	-95	5.3
CAM-MB-21-85	Beaver-Cloud	-89	5.5
CAM-MB-21-127	Beaver-Cloud	-81	3.1
CAM-MB-21-136	Beaver-Cloud	-76	6.3
CAM-MB-21-144	Beaver-Cloud	-71	4.6
CAM-MB-21-163	437-SEA	-87	5.7
CAM-MB-21-177	437-SEA	-63	7.7
CAM-MB-21-184	437-SEA	-81	5.4
CAM-MB-21-91	Beaver-Cloud	-87	6.4
CAM-MB-21-108	Beaver-Cloud	-90	6.2
CAM-MB-21-30	Current	-84	6.3
CAM-MB-21-61	Current	-91	4.5
CAM-MB-21-65	Beaver-Cloud	-88	6.3
CAM-MB-21-74	Beaver-Cloud	-95	5.6
CAM-MB-21-83	Beaver-Cloud	-83	6.1
CAM-MB-21-93	Beaver-Cloud	-95	5.6
CAM-MB-21-101	Beaver-Cloud	-69	7.2
CAM-MB-21-109	Beaver-Cloud	-94	4.7
CAM-MB-21-118	Beaver-Cloud	-93	6.1
CAM-MB-21-122	Beaver-Cloud	-90	4.7
CAM-MB-21-140	Beaver-Cloud	-79	6.1
CAM-MB-21-152	Beaver-Cloud	-76	5.9
CAM-MB-21-156	437-SEA	-63	6.4
CAM-MB-21-171	437-SEA	-75	5.5
CAM-MB-21-201	Country Rock	-113	10
CAM-MB-21-215	Country Rock	-81	10.2
CAM-MB-21-72	Country Rock	-90	10.1

Sample ID	Zone	$\delta^{2}H$	$\delta^{18}O$
CAM-MB-21-45	Country Rock	-89	9.5